Unconventional Superconductivity and Majorana Modes

Henrik Schou Røising
Balliol College
University of Oxford

A thesis submitted for the degree of
Doctor of Philosophy in Theoretical Physics

Trinity Term 2020

Abstract

In this thesis superconductivity with unconventional pairing symmetries arising from repulsive interactions is investigated. Anyonic quasiparticles within the subclass of chiral p-wave superconductors are also examined.

In Chapter 2 we study weak-coupling superconductivity in a repulsive Hubbard model on the tetragonal lattice. With the weak-coupling approximation we establish the superconducting phase diagram as the out-of-plane hopping strength and electron filling is varied. For four Fermi surface topologies we identify a total of five types of p- and d-wave ground state orders, several of which have accidental line nodes and break time-reversal symmetry.

The weak-coupling scheme is adapted to strontium ruthenate (Sr_2RuO_4) in Chapter 3. We compute and compare odd- and even-parity superconducting order parameters using a realistic three-dimensional band structure. Two superconducting phases are identified: a helical p-wave spin triplet and a d-wave spin singlet phase. Both orders are roughly found to be compatible with specific heat data and recent nuclear magnetic resonance measurements [A. Pustogow et al., Nature **574**, 72 (2019)]. We suggest that a d-wave order is likely involved in the superconducting phase, although certain experiments appear to remain incompatible with this conclusion.

In Chapter 4 we describe anyonic (Majorana) quasiparticles in chiral p-wave superconductors at temperatures non-negligible compared to the superconducting gap. We consider the impact of thermally occupying in-gap vortex states on the hybridisation of two Majorana modes. The hybridisation, reflecting the state of the qubit defined by the two Majorana modes, is found to decay algebraically with temperature just above the first-excited state energy scale. In novel iron-based superconductors our results suggest that there is an appreciable temperature range in which qubit read-out can be achieved via the inter-vortex force derived from the hybridisation.

Acknowledgements

First and foremost, I am profoundly indebted to my supervisor, Steven Simon, who has willingly shared of his tremendous insight and fruitful ideas with an unmatched passion for physics. I further thank him for his admirable patience with me. Secondly, I have been very fortunate to work with Thomas Scaffidi and Felix Flicker. Both have provided indispensable guidance.

I thank Dmitry Kovrizhin, Jon Magne Leinaas, Tobias Meng, Yoshiteru Maeno, Fabian Essler, Alexander Balatsky, Catherine Kallin, Mats Horsdal, Fabian Jerzembeck, Glenn Wagner, and Joe Huxford for discussions, feedback, and helpful comments at various points in time.

I am grateful for having shared *the real office* with Yuri van Nieuwkerk, Edward O'Brien, and Tunrayo Adeleke-Larodo. The numerous discussions, formals, and chats we have had have been essential. I thank Nikola Gushterov, Stefan Groha, and Richard Fern, for making me feel welcome at the Rudolf Peierls Centre, and for your friendliness and advice.

I am deeply grateful to the Aker Scholarship (The Anne Grete Eidsvig and Kjell Inge Røkke charitable foundation for education) and in particular to Bjørn Blindheim. This is due to the personal guidance and financial support which have allowed me to pursue my physics dream. Equally valuable, however, is the access to a community of talented individuals summoned by Bjørn, many of whom have become my friends for life and made the time Oxford an unforgettable experience. I am especially thankful for having met Jonas Heen Haeg, Vidar Skretting, Fredrik Vaeng Røtnes, Ellen Tveteraas, Eirik Kvindesland, Allan D'Silva, Mikael Hiberg Naghizadeh, and Andreas Svela.

I thank Mari Røysheim and Eli Bæverfjord Rye for our lasting and sincere friendship. A special and warm greeting to Silje Saurdal, for your strength and acumen (and for teaching me the ways of Yatzy). Finally, I warmly thank my family, Hanne Schou Røising, Leif Hugo Stubrud, and Victoria Fredrikke Schou Røising, for your continued care and wisdom, and for putting up with me during stressful periods.

Contents

Appendices

List of Abbreviations

1D, 2D, 3D	One-, two- or three-dimensional, referring to spatial dimensions
SRO	Strontium ruthenate, Sr_2RuO_4
BCS	Bardeen–Cooper–Schrieffer
ABM	Anderson–Brinkman–Morel
BW	Balian–Werthamer
KL	Kohn–Luttinger
BdG	Bogoliubov–de Gennes
CdGM	Caroli–de Gennes–Matricon
NMR	Nuclear magnetic resonance
ARPES	Angle-resolved photoemission spectroscopy
BZ	Brillouin zone
Irrep	Irreducible representation
SOC	Spin-orbit coupling
TRSI	Time-reversal symmetry invariant
TRSB	Time-reversal symmetry breaking
PHS	Particle-hole symmetry
TSC	Topological superconductivity/superconductor
MZM	Majorana zero mode

Chapter 1

Introduction

1.1 Prelude

Superconductivity is most commonly associated with dissipationless flow of currents and expulsion of external magnetic fields. The phenomenon has, over its more than 100-year long history, proven to be common in solid state systems. Still, there is a growing number of instances in which superconductivity is yet to be fully understood. As a prime example of a collective phase in many-body physics – with applications of both theoretical and practical significance – superconductivity is worthy of profound interest.

Superconductivity was initially discovered by Heike Kamerlingh Onnes in 1911 [1], who observed the resistivity of mercury dropping to zero below temperatures of 4.2 K. But almost half a century would pass before a satisfactory theory of the phenomenon was presented: the celebrated Bardeen–Cooper–Schrieffer (BCS) theory of superconductivity developed in 1957 [2]. In this theory, the motion of electrons distorts the underlying ion lattice, giving rise to an effective attraction between the electrons. The electron-phonon-mediated attraction was, by BCS, found to favour electrons pairing up to form bosonic Cooper pairs, which then condense to form a superfluid in a manner reminiscent of Bose–Einstein condensation. The Cooper pairs considered by BCS consist of electrons in a spin singlet and zero relative angular momentum state – a spherically symmetric bound state – denoted by s-wave pairing. The paradigm developed by BCS is today commonly known as *conventional superconductivity.*

In the years following the development of BCS theory, superconductivity in numerous elements and compounds was found to be in full agreement with predictions derived from the theory. Well-studied examples include aluminium, niobium, and lead [3]. The first example of non-s-wave pairing came with the discovery of superfluidity in liquid helium-3 (^{3}He), identified in nuclear magnetic resonance (NMR) experiments by Osheroff and collaborators in 1971 [4]. However, ^{3}He is not a superconductor, but a superfluid in which the Cooper pairs are bound states of neutral fermions. The Cooper pairs of ^{3}He have spins in a triplet state and relative angular momentum 1 (in units of $\hbar$) [5–7], called p-wave pairing. According to the Pauli principle, the relative angular momentum of the Cooper pairs must be odd if the spins are in a symmetric state. The pairing mechanism of ^{3}He is clearly non-phononic (there is no lattice). Indeed, a spin-fluctuation mediated interaction causes non-rotationally symmetric Cooper pairs in this case [8].

With the discovery of heavy fermion superconductors [9] and the cuprates [10] in the 1980s, it became evident that ever-growing families of strongly correlated solid state systems lack explanation within the BCS phonon paradigm. The cuprates have spin singlet Cooper pairs of relative angular momentum[1] 2, and the heavy fermion superconductors, like UPt_3 [12, 13], typically have complicated phase diagrams and may support multiple phases. These systems have in common that their pairing mechanism is believed to, at least partly, be mediated by electron-electron interactions [11]. Throughout this thesis the phenomenon of superconductivity with non-s-wave pairing will be referred to as *unconventional superconductivity.*

---

[1] To be precise, the Cooper pairs deriving from a lattice system (no rotational invariance) are characterised by their symmetries with respect to the crystal point group, not the angular momentum. For instance, s-wave means that the symmetries of the Cooper pairs coincide with the trivial representation of the crystal point group [11].

1.2 Motivation

The temperature below which a material superconducts is called the critical temperature, T_c. The cuprates, for instance, have T_c ranging from about 30 to 150 K. One of the long-standing goals in the field of superconductivity is to ultimately achieve room-temperature superconductivity, which could have a large impact on technology. A general framework for predicting superconductivity and the associated critical temperature in new compounds is elusive and remains a holy grail in the field of high-T_c superconductivity.

In the 1960s, Kohn and Luttinger [14] proposed a novel mechanism for unconventional superconductivity arising from weakly repulsive electron interactions. Their mechanism generically yields low critical temperatures compared to the Fermi energy, and it is thus not expected to be applicable to high-T_c superconductivity. However, the framework is tractable, and it has proven helpful in gaining fundamental insight into the favoured superconducting pairing states in lattice models [15]. The repulsive Hubbard model [16], characterised by a repulsive on-site density-density interaction, is well-suited for exploring the Kohn–Luttinger mechanism. Serving as a technical background for the remainder of this thesis, an extensive study of the Kohn–Luttinger mechanism in an anisotropic three-dimensional Hubbard model is presented in Chapter 2.

A prime example of an unconventional superconductor of historical importance is strontium ruthenate (Sr_2RuO_4, SRO), in which superconductivity was discovered by Yoshiteru Maeno and collaborators in 1994 [17]. For almost two decades SRO has been widely hypothesised to be a chiral p-wave superconductor[2] – a solid state analogue of ^{3}He [18]. Recently, however, the understanding of superconductivity in this material reached a turning point due to NMR experiments, casting serious doubt on the chiral p-wave hypothesis [19, 20]. As a result, the debate regarding the superconducting state in SRO has substantially heated up over the last

---

[2] Here, “chiral” means that the pairing has spontaneously chosen one of the particular complex phases $p_x + ip_y$ or $p_x - ip_y$, as discussed in Subsection 2.3.2.

year. Determining the pairing symmetry is currently considered an open problem. Unconventional superconductivity in SRO is the topic of Chapter 3.

A major strand of superconductivity research lies within the subclass of *topological superconductors* (defined in Chapter 4), which was first discovered theoretically around the beginning of this century. In seminal works by Read and Green, Kitaev, and Ivanov [21–23] it was demonstrated that chiral p-wave superconductors can support quasiparticle excitations called non-Abelian anyons[3], the appearance of which is closely related to the concept of topological superconductivity. In general, anyons have exchange statistics different from that of fermions and bosons [25, 26], and they come in two flavours: Abelian or non-Abelian [27]. The definite experimental confirmation of anyons would be a major triumph for theoretical physics. In addition, non-Abelian anyons can in principle be used to encode quantum information and hence constitute the basic building blocks of a (topological) quantum computer [28]. Quantum computers exploit the quantum superposition principle by coherent action on quantum states. In a topological quantum computer, the non-local properties of non-Abelian anyons are exploited to achieve quantum computation in a fashion that by nature is resistant to errors. A quantum computer could revolutionise the way certain problems, like prime number factorisation [29] and quantum simulations [30, 31], are solved.

The search for chiral p-wave superconductors has intensified in the hope of realising and employing non-Abelian anyons for quantum computation [28, 32, 33]. The non-Abelian anyons appearing in a chiral p-wave superconductor are called *Majorana zero modes*. They are neutral quasiparticles of zero energy which localise in vortex cores and on domain walls. Two Majorana zero modes are needed to form one quantum information unit, a quantum bit or *qubit* – defining the basic two-level system which is to be manipulated in quantum computing protocols. Concrete protocols for quantum computation with Majorana zero modes exist [34, 35], but they are faced with major obstacles in practice. For instance, to exploit Majorana zero modes in vortex cores, it is commonly believed that the temperature needs to

---

[3] Such quasiparticles were first predicted to appear in the fractional quantum Hall system [24].

be very low to avoid thermal excitations of fermionic in-gap states [36]. Another issue faced by protocols for Majorana based quantum computing is having a scheme for reading out the state of the qubit. Finite temperature effects and read-out of Majorana qubits in vortex cores is the topic of Chapter 4.

1.3 Outline

The bulk of this degree has been concerned with the publications of References [37–40]. The content presented in Chapters 2, 3, and 4 of this thesis are primarily based on References [38], [40], [39], respectively.

The outline of this thesis is as follows. In Sections 2.1 and 2.2 we derive and review the Kohn–Luttinger method for calculating the favoured unconventional pairing states in tetragonal lattice models with weak repulsive interactions. In Section 2.3 an anisotropic Hubbard model is presented for which we, in Section 2.4, calculate asymptotically exact results in the weak-coupling low-filling limit. Relaxing the low-filling condition, the full weak-coupling ground state phase diagram is established numerically in Section 2.5, and Section 2.6 comments on the range of validity of these results.

In Section 3.1 we provide a historical and experimental overview of strontium ruthenate, and the continued interest in studying unconventional superconductivity in this perovskite is motivated. A realistic three-dimensional tight-binding model for the normal state of SRO is developed in Section 3.2. The weak-coupling framework for multiband superconductors with spin-orbit coupling is reviewed in Section 3.3 and applied numerically to SRO in Section 3.4. In Section 3.5 a detailed comparison of the results with two key experimental probes is provided. The chapter is concluded with a discussion of outstanding aspects in Section 3.6.

In Section 4.1 the concept of topological superconductivity is introduced. We focus on superconductors with chiral p-wave pairing and their low-energy quasiparticles localised in vortex cores in Section 4.2. In Section 4.3 we study a chiral p-wave superconductor containing two vortices, each hosting a Majorana zero mode. We characterise the energy hybridisation between the Majorana zero modes when both the inter-vortex separation and the temperature is finite. In Section 4.4 we discuss how the hybridisation offers a novel route to achieving read-out of the Majorana qubit. The proposed scheme is based on measuring the inter-vortex force contribution derived from the hybridisation – a contribution that is sensitive to the state of the qubit. We also discuss the main practical limitations that possibly hinder the realisation the proposed scheme. Chapter 4 is concluded with a summary and a material-oriented outlook in Section 4.5. Finally, the thesis is summarised and concluded in Chapter 5.

Chapter 2

Superconductivity in an Anisotropic Hubbard Model

Contents

2.1 Introduction

2.1.1 Kohn–Luttinger Superconductivity

Soon after phonon-mediated superconductivity was microscopically understood with BCS theory, Kohn and Luttinger (KL) [14, 41] proposed that superconductivity (and superfluidity) could arise also from purely repulsive electron interactions[1]. Today, electron-electron interactions are believed to be an important ingredient in most instances of unconventional superconductivity [11]. The KL-mechanism for Cooper pairing relies on the sharpness of the Fermi surface and screening of the bare interactions. Technically, the key idea is that pairing in the particle-particle

---

[1] Gor'kov and Melik-Barkhudarov [42] presented similar ideas in 1961, a few years before KL.

channel is determined by the *irreducible vertex* (which is defined in Subsection 2.2.2). The irreducible vertex includes contributions from the particle-hole continuum and can conspire to create an attraction in some pairing channel, even though the initial electron-electron interaction is repulsive.

Intuitively, the physics here is reminiscent to that of a charge impurity in a metal. Screening of the charge leads to density (Friedel) modulations away from the charge impurity. The modulations result in a long-range Coulomb potential proportional to $\cos(2k_F r + \varphi)/r^3$, where k_F is the Fermi momentum, r the distance from the impurity, and φ some phase [43]. In some angular momentum channel l, the two-particle wavefunction may have its dominant weight at distances coinciding with the attractive tail of the potential, leading to stable Cooper pairs in that channel. Here, $l = 0, 1, 2, \dots$ corresponds to s-, p-, d-wave pairing etc. For screened electrons in metals with weak short-range interactions and rotational invariance, as considered by Kohn and Luttinger, the transition temperature scales (asymptotically) with angular momentum like

$$k_B T_c / E_F \sim \exp\big[-(2l)^4 \big], \tag{2.1}$$

where E_F is the Fermi energy, and k_B is the Boltzmann constant [14]. The dependence on l results in very low critical temperatures, in stark contrast to e.g. the critical temperatures applicable to the cuprates [10].

The KL-mechanism is derived in the limit of weak interactions compared to the electronic bandwidth, a limit we will refer to as the *weak-coupling limit* in this thesis. Even though this limit formally does not apply to (nearly any) real materials, the KL-mechanism, in various forms and generalisations, has still harboured great success and valuable insight when applied to real systems [44]. The weak-coupling approximation has an advantage in being controlled[2] and numerically tractable in otherwise very complicated problems. Furthermore, we will in Subsection 3.4.3 argue in the context of the models considered in this and the next chapter that the

---

[2] Controlled in the sense that the critical temperature and pairing symmetry obtained are asymptotically exact as $U/W \ll 1$, where U is the interaction strength and W is the bandwidth [15].

range of validity can be reasonably expected to extend beyond what is formally the weak-coupling regime.

2.1.2 The Hubbard Model

In condensed matter theory, the Hubbard model – named after John Hubbard who did seminal work in the 1960s [16] – represents perhaps the simplest paradigm of interacting models to study (super)conducting and insulating phases of matter on the lattice. The single-band Hubbard model is a many-body second-quantised model valid when the Fermi energy lies inside a single conduction band, with weak inter-band interactions. In its simplest form the Hubbard model is given by

$$H = -t \sum_{s,\langle ij \rangle} c^{\dagger}_{is} c_{js} - \mu \sum_{s,i} n_{is} + U \sum_{i} n_{i\uparrow} n_{i\downarrow}, \tag{2.2}$$

where c_{is} ($c^{\dagger}_{is}$) annihilates (creates) an electron of spin s on lattice site i, $n_{is} = c^{\dagger}_{is} c_{is}$ is the density operator, t is the hopping strength between neighbouring sites $\langle ij \rangle$, μ is the chemical potential, and U is the Hubbard interaction parameter. Despite the apparent simplicity of the model, it has been widely shown to support rich phases ranging from Mott insulators to (anti)ferromagnetism [45]. Determining the full phase diagram of the two- and three-dimensional Hubbard model persists as an extremely difficult and largely open problem [46, 47].

To this end, a great deal has been established in the weak-coupling limit $U/t \ll 1$ (with repulsive interactions $U > 0$) [48–53]. In this limit, the square lattice (2D) Hubbard model supports two types of d-wave superconductivity as a function of the electron filling ($\langle n \rangle$) below half-filling ($\langle n \rangle = 1$), with a tiny pocket of p-wave superconductivity at intermediate filling [53]. The cubic lattice (3D) Hubbard model supports d- and p-wave superconductivity at high and low electron filling at weak coupling, respectively [48]. Superconductivity in the 2D Hubbard model has also been studied with e.g. the random phase approximation (RPA) [54, 55]. In RPA, an infinite series of bubble diagrams, representing the interaction vertex, is summed up at the expense of neglecting another infinite set of diagrams, leaving little control of the error at finite U/t [56].

The weak-coupling (Kohn–Luttinger) scheme on the lattice was recast as a renormalisation group (RG) approach by Raghu, Scalapino, and Kivelson [15], which is formally equivalent to the method we present and apply in this and the succeeding chapter. In the RG framework, the high-energy degrees of freedom are integrated out, and divergence of the RG flow of the effective two-particle vertex (defined in Subsection 2.2.2) in the Cooper channel is used as the defining criterion for the onset of superconductivity. It is shown in Ref. [15] that the critical temperature permits an asymptotic expansion when using perturbation theory in U/t for the effective two-particle vertex. Any diagram beyond second order in U contributes with subleading corrections in U/t and can hence be neglected in the weak-coupling limit.

2.1.3 Outline

In this chapter we review the weak-coupling scheme introduced by Kohn and Luttinger. We give a detailed derivation of the generalised gap equation, the solution of which defines the *superconducting order parameter*. We provide an overview of the symmetries of the solutions to the generalised gap equation for tetragonal lattice models. The generalised gap equation is then solved for an anisotropic Hubbard model, defined to generally have different in-plane ($t_\parallel$) and out-of-plane ($t_\perp$) nearest-neighbour hopping strengths. The model continuously interpolates between the 2D ($t_\parallel = 0$) and the 3D ($t_\parallel = t_\perp$) repulsive Hubbard model. In the 3D, low-filling limit case we recover known results in terms of the critical temperature and the order parameter symmetry.

We expand on known results by calculating how the three-fold degeneracy of the ground state is lifted when the hopping parameter $t_\perp$ is tuned away from the case of $t_\parallel = t_\perp$ at low filling, which makes the Fermi surface a prolate ($t_\parallel > t_\perp$) or oblate ($t_\parallel < t_\perp$) spheroid. We then relax the low-filling condition and establish the full weak-coupling ground state phase diagram numerically, as a function of the chemical potential per in-plane hopping strength $\mu/t_\parallel$ and the hopping ratio $t_\perp/t_\parallel$. We investigate the nodal structure of the superconducting order parameter at various points in the phase diagram. Interestingly, we find chiral p-wave order with horizontal line nodes for a weakly corrugated cylindrical Fermi surface. This is surprising since "textbook" chiral p-wave order on a cylindrical Fermi surface is expected to be uniform and fully gapped.

2.2 Theoretical Background

2.2.1 Cooper Susceptibility

To set the stage for superconductivity in repulsive lattice models, our starting point is an interacting second-quantised Hamiltonian in reciprocal space:

$$\begin{aligned} H &= H_K + H_I \\ &= \sum_{\boldsymbol{k},s} \xi_{\boldsymbol{k}} c^\dagger_{\boldsymbol{k}s} c_{\boldsymbol{k}s} + \sum_{\substack{\{\boldsymbol{k}_i\}: \\ \boldsymbol{k}_1+\boldsymbol{k}_2=\boldsymbol{k}_3+\boldsymbol{k}_4}} \sum_{\{s_i\}} V_{\boldsymbol{k}_1 s_1;\boldsymbol{k}_2 s_2;\boldsymbol{k}_3 s_3;\boldsymbol{k}_4 s_4} c^\dagger_{\boldsymbol{k}_1 s_1} c^\dagger_{\boldsymbol{k}_2 s_2} c_{\boldsymbol{k}_3 s_3} c_{\boldsymbol{k}_4 s_4}. \end{aligned} \tag{2.3}$$

Here, $\xi_{\boldsymbol{k}} = \epsilon_{\boldsymbol{k}} - \mu$, where $\epsilon_{\boldsymbol{k}}$ is the single-particle energy, and μ is the chemical potential. Further, V is the bare two-body interaction potential, and $c^\dagger_{\boldsymbol{k}s}$ is the creation operator of an electron of crystal momentum $\boldsymbol{k}$ and spin s. The momentum sums in the interacting part of the Hamiltonian run over $\{\boldsymbol{k}_i\} = \{\boldsymbol{k}_1, \boldsymbol{k}_2, \boldsymbol{k}_3\}$, with $\boldsymbol{k}_4 = \boldsymbol{k}_1 + \boldsymbol{k}_2 - \boldsymbol{k}_3$ due to momentum conservation. The spin sums run over $\{s_i\} = \{s_1, s_2, s_3, s_4\}$. As a matter of convention, crystal momenta appearing in this thesis are assumed dimensionless, i.e. scaled by the associated lattice spacing.

The hallmark of superconductivity is a non-vanishing thermal expectation value of the Cooper pair creation operator

$$\Phi^\dagger_{\boldsymbol{k}ss'} \equiv c^\dagger_{\boldsymbol{k}s} c^\dagger_{-\boldsymbol{k}s'}. \tag{2.4}$$

Within a linear response field theory approach [41, 56–60], one can relate the thermal expectation value of Eq. (2.4) to the Hamiltonian of Eq. (2.3). The crucial step in this process is to allow coupling to an auxiliary field J of the form $H_J = \sum_{\boldsymbol{k}} J_{\boldsymbol{k}ss'} \Phi_{\boldsymbol{k}ss'} + \text{h.c.}$, where J is assumed small compared to the energy scales of H. The thermal expectation of Eq. (2.4) is evaluated within a fermionic coherent state representation, i.e. an imaginary-time field theory where time is defined in terms of the inverse temperature, $it = \beta \equiv 1/(k_B T)$. The coherent state representation is defined in terms Grassmann variables $\alpha_{\boldsymbol{k}s}(\omega)$ of fermionic

Matsubara frequency $\omega = (2n+1)\pi/\beta$, which by definition are eigenvalues of the annihilation operator $c_{\boldsymbol{k}s}$. The result of these briefly outlined steps is the entrance of the Cooper susceptibility[3]:

$$\begin{aligned}\chi^{\text{Cooper},c}_{\boldsymbol{k}_1 s_1 s_1';\boldsymbol{k}_2 s_2 s_2'}(\omega_1,\omega_2) = &\left\langle \bar{\alpha}_{\boldsymbol{k}_2 s_2}(\omega_2)\bar{\alpha}_{-\boldsymbol{k}_2 s_2'}(-\omega_2)\alpha_{-\boldsymbol{k}_1 s_1'}(-\omega_1)\alpha_{\boldsymbol{k}_1 s_1}(\omega_1)\right\rangle_I \\ &- \left\langle \bar{\alpha}_{-\boldsymbol{k}_2 s_2'}(-\omega_2)\alpha_{-\boldsymbol{k}_1 s_1'}(-\omega_1)\right\rangle_I \left\langle \bar{\alpha}_{\boldsymbol{k}_2 s_2}(\omega_2)\alpha_{\boldsymbol{k}_1 s_1}(\omega_1)\right\rangle_I \\ &+ \left\langle \bar{\alpha}_{-\boldsymbol{k}_2 s_2'}(-\omega_2)\alpha_{\boldsymbol{k}_1 s_1}(\omega_1)\right\rangle_I \left\langle \bar{\alpha}_{\boldsymbol{k}_2 s_2}(\omega_2)\alpha_{-\boldsymbol{k}_1 s_1'}(-\omega_1)\right\rangle_I .\end{aligned} \tag{2.5}$$

Here the expectation values are evaluated in the interacting theory,

$$\langle A \rangle_I = \frac{\text{Tr}\left[A e^{S_K + S_I}\right]}{\text{Tr}\left[e^{S_K + S_I}\right]}, \tag{2.6}$$

where S_K (S_I) is the coherent state action deriving from H_K (H_I). We define the Cooper instability criterion to be a divergence in the connected Cooper susceptibility at temperature T_c and zero frequency[4] [41]. At temperature T_c the system becomes unstable towards the formation of Cooper pairs.

The critical temperature can now be determined by perturbation theory in S_I, assuming that the interactions are weak. The perturbative approach makes use of a diagrammatic representation of the Cooper susceptibility, defined by the two basic Feynman rules shown in Fig. (2.1), which follow from the Hamiltonian of Eq. (2.3).

2.2.2 The Two-Particle Vertex

Building on the Cooper susceptibility introduced above, we introduce the two-particle vertex as

$$\begin{aligned}\mathcal{V}_{\boldsymbol{k}_1 s_1 s_1';\boldsymbol{k}_2 s_2 s_2'}(\omega_1,\omega_2) \equiv -\frac{1}{2\beta}&(i\omega_1 - \xi_{\boldsymbol{k}_1})(-i\omega_1 - \xi_{-\boldsymbol{k}_1})(i\omega_2 - \xi_{\boldsymbol{k}_2})(-i\omega_2 - \xi_{-\boldsymbol{k}_2}) \\ &\times \chi^{\text{Cooper},c}_{\boldsymbol{k}_1 s_1 s_1';\boldsymbol{k}_2 s_2 s_2'}(\omega_1,\omega_2).\end{aligned} \tag{2.7}$$

Convenient factors of the inverse Green's function are introduced to cancel contributions from the four external legs of the Cooper susceptibility. The vertex can be represented as an infinite series of all connected two-particle diagrams with ingoing

---

[3] Precisely: $\langle \Phi_{\boldsymbol{k}_1 s_1 s_1'} \rangle = -\frac{1}{\beta^3}\sum_{\boldsymbol{k}_2,\omega_1,\omega_2,s_2,s_2'} \chi^{\text{Cooper}}_{\boldsymbol{k}_1 s_1 s_1';\boldsymbol{k}_2 s_2 s_2'}(\omega_1,\omega_2)(J_{\boldsymbol{k}_2 s_2 s_2'})^*$, where χ^{Cooper} is the unconnected version of Eq. (2.5).

[4] We note, however, that there is a growing interest in the possibility of finite-frequency pairing [61].

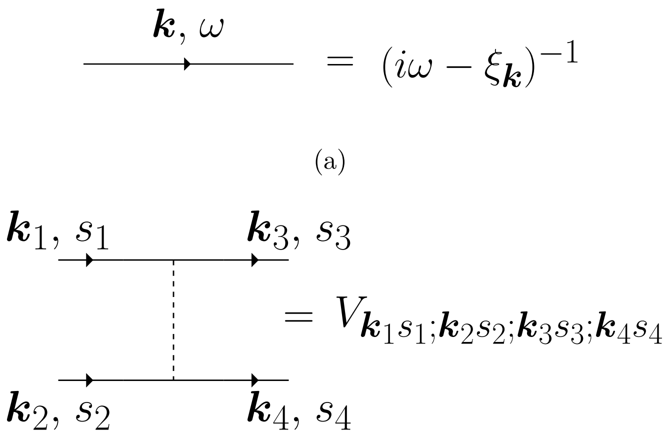

(a)

(b)

Figure 2.1: The basic Feynman rules defined by the theory in Eq. (2.3). (a) Solid lines are representations of bare particle Green's functions, and (b) dotted lines represent the (momentum-conserving) two-particle bare interaction potential.

external legs of indices $(\boldsymbol{k}_1, s_1, \omega_1)$ and $(-\boldsymbol{k}_1, s_1', -\omega_1)$, and outgoing external legs of indices $(\boldsymbol{k}_2, s_2, \omega_2)$ and $(-\boldsymbol{k}_2, s_2', -\omega_2)$.

In the same fashion, the irreducible two-particle vertex Γ is defined as the sum of all connected *two-particle irreducible diagrams.* The two-particle irreducible diagrams are those diagrams which cannot be reduced to two disconnected diagrams when cutting any two internal lines (propagators). By definition, this allows us to express the two-particle vertex as a composition of two-particle irreducible vertices, as shown diagrammatically in Fig. 2.2. In matrix notation this is expressed and formally solved via the Bethe–Salpeter equation [62]:

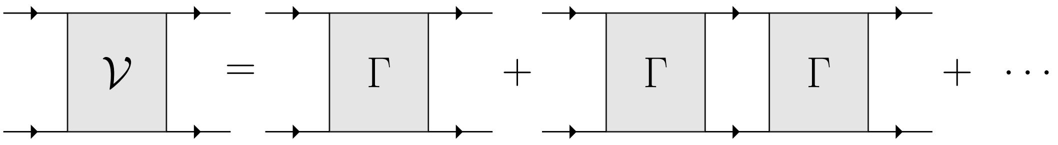

Figure 2.2: Diagrammatic representation of the two-particle vertex $\mathcal{V}$ decomposed into compositions of the irreducible two-particle vertex Γ. Full lines represent bare Green's function, and internal lines are summed over.

$$
\begin{aligned}
-\mathcal{V} &= -\Gamma + \Gamma \star \mathcal{G}_0 \star \Gamma + \dots \\
&= -\Gamma + \Gamma \star \mathcal{G}_0 \star \mathcal{V} \qquad (2.8) \\
&\Rightarrow \mathcal{V} = (\mathbb{1} + \Gamma \star \mathcal{G}_0)^{-1} \star \Gamma.
\end{aligned}
$$

Above, the $\star$ product contains a factor of β^{-1} and a contraction over repeated indices[5], and the inverse operation in Eq. (2.8) is meant with respect to this product. The two-particle Green's function was also introduced as

$$(\mathcal{G}_0)_{\boldsymbol{k}_1 s_1 s_1'; \boldsymbol{k}_2 s_2 s_2'}(\omega_1, \omega_2) = \beta(i\omega_1 - \xi_{\boldsymbol{k}_1})^{-1}(-i\omega_1 - \xi_{-\boldsymbol{k}_1})^{-1}\delta_{\boldsymbol{k}_1 s_1 s_1' \omega_1, \boldsymbol{k}_2 s_2 s_2' \omega_2}. \tag{2.9}$$

Note that Eq. (2.8) is an exact recasting of the vertex, showing that a pole in the vertex originates from the irreducible vertex [41]. Specifically, from Eq. (2.8) it is clear that an eigenfunction of $\Gamma \star \mathcal{G}_0$ with eigenvalue -1 signals a singularity in the two-particle vertex and thus by definition the onset of superconductivity.

In Subsection 2.2.4 we determine the critical temperature by treating Γ with perturbation theory. In the RG formulation of Ref. [15] it is shown that the decomposition of Fig. 2.2 then yields a consistent theory at all orders in U/t, with the expression for the critical temperature being independent of an artificially introduced energy cutoff above which states are integrated out.

2.2.3 The Generalised Gap Equation

We are thus interested in the eigenfunctions Δ of $\Gamma \star \mathcal{G}_0$ corresponding to the eigenvalue -1:

$$\Gamma \star \mathcal{G}_0 \star \Delta = -\Delta. \tag{2.10}$$

This is a general form of the celebrated gap equation [56, 58]. An eigenfunction of the equation Δ defines a superconducting order parameter (or gap). The order parameter is a direct measure of the superconducting excitation gap in the ground state, and it reflects the energy needed to break up a Cooper pair. Below, the gap equation is simplified to a useful form that can be readily implemented numerically.

Assume that in some temperature regime below a frequency cutoff[6] $k_B T \ll \omega_c$ there is a solution to the gap equation with no frequency-dependence, and that the frequency-dependence of the vertex in this regime can be ignored. For an

---

[5] To be precise: $(\mathcal{G}_0 \star \Gamma)_{\boldsymbol{k}_1 s_1 s_1'; \boldsymbol{k}_2 s_2 s_2'}(\omega_1, \omega_2) = \frac{1}{\beta}\sum_{\boldsymbol{k}, \omega, s, s'}(\mathcal{G}_0)_{\boldsymbol{k}_1 s_1 s_1'; \boldsymbol{k} s s'}(\omega_1, \omega)\Gamma_{\boldsymbol{k} s s'; \boldsymbol{k}_2 s_2 s_2'}(\omega, \omega_2)$.

[6] Indeed, the critical temperature will emerge at an energy scale exponentially smaller than ω_c, cf. Eq. (2.1).

electronically driven mechanism of superconductivity, we will take ω_c to be on the order of the bare bandwidth. In contrast, ω_c would have been associated with the Debye frequency ω_D in a BCS superconductor where phonons of the underlying ion lattice set the cutoff. The above assumptions allow us to factorise Eq. (2.10) as

$$\frac{1}{\beta}\sum_{\substack{\boldsymbol{k},s,s'\\|\xi_{\boldsymbol{k}}|<\omega_c}}\Gamma_{\boldsymbol{k}_1 s_1 s_1';\boldsymbol{k}ss'}\Delta_{ss'}(\boldsymbol{k})\sum_{|\omega|<\omega_c}(i\omega-\xi_{\boldsymbol{k}})^{-1}(-i\omega-\xi_{-\boldsymbol{k}})^{-1}=-\Delta_{s_1 s_1'}(\boldsymbol{k}_1). \quad (2.11)$$

The innermost frequency sum is evaluated using the residue theorem. As such, we define the complex function and the fermionic Matsubara weight function as

$$h(z)=(z-\xi_{\boldsymbol{k}})^{-1}(-z-\xi_{-\boldsymbol{k}})^{-1}, \quad (2.12)$$

$$f(z)=(1+\exp(\beta z))^{-1}, \quad (2.13)$$

respectively. The weight function $f(z)$, i.e. the Fermi function, is used since it has its simple poles situated at $z=i\omega_n=i(2n+1)\pi/\beta$ with residues $\operatorname{Res}\left[f(z),\ z=i\omega_n\right]=-1/\beta$. Thus, by standard complex integration techniques (inflating the contour) we are left with two contributions [60]:

$$\begin{aligned}\frac{1}{\beta}\sum_{|\omega_n|<\omega_c}h(z=i\omega_n)&=-\sum_{|\omega_n|<\omega_c}\operatorname{Res}\left[h(z)f(z),\ z=i\omega_n\right]\\&=\sum_{w=\xi_{\boldsymbol{k}},-\xi_{-\boldsymbol{k}}}\operatorname{Res}\left[h(z)f(z),\ z=w\right]-\frac{1}{2\pi i}\oint_{|z|=\omega_c}\mathrm{d}z\ h(z)f(z)\\&=\frac{\tanh(\beta\xi_{\boldsymbol{k}}/2)}{2\xi_{\boldsymbol{k}}}-0,\end{aligned} \quad (2.14)$$

where we made use of the limit $k_B T \ll \omega_c$ and assumed that $\xi_{-\boldsymbol{k}}=\xi_{\boldsymbol{k}}$.

The momentum sum in Eq. (2.11) is evaluated as an integral in the coordinates $(\xi,\ \hat{\boldsymbol{k}})$, where $\hat{\boldsymbol{k}}$ lies on the Fermi surface defined by $S_F(\xi)\equiv\{\hat{\boldsymbol{k}}:\ \xi_{\hat{\boldsymbol{k}}}=\xi\}$:

$$\sum_{\substack{\boldsymbol{k}:\\|\xi_{\boldsymbol{k}}|<\omega_c}}(\ldots)=\int_{-\omega_c}^{\omega_c}\mathrm{d}\xi\int_{S_F(\xi)}\mathrm{d}\hat{\boldsymbol{k}}\,\frac{1}{|\nabla\xi_{\hat{\boldsymbol{k}}}|}(\ldots)=\int_{-\omega_c}^{\omega_c}\mathrm{d}\xi\,\rho_\xi\int_{S_F(\xi)}\frac{\mathrm{d}\hat{\boldsymbol{k}}}{|S_F|}\frac{\bar{v}_F}{v_F(\hat{\boldsymbol{k}})}(\ldots). \quad (2.15)$$

In the last expression we introduced a number of definitions, namely the Fermi velocity, the average Fermi velocity, and the density of states as

$$
\begin{aligned}
v_F(\hat{\boldsymbol{k}}) &= |\nabla \xi_{\hat{\boldsymbol{k}}}|, && (2.16)\\
\bar{v}_F &= \Big(\int_{S_F(\xi)} \frac{\mathrm{d}\hat{\boldsymbol{k}}}{|S_F|} \frac{1}{v_F(\hat{\boldsymbol{k}})} \Big)^{-1}, && (2.17)\\
\rho_\xi &= \int_{S_F(\xi)} \frac{\mathrm{d}\hat{\boldsymbol{k}}}{(2\pi)^3} \frac{1}{v_F(\hat{\boldsymbol{k}})}, && (2.18)
\end{aligned}
$$

respectively. Finally, the Fermi surface area is denoted by $|S_F|$. When combining Eqs. (2.14) and (2.15) in Eq. (2.11) we arrive at the following simplified version of the gap equation:

$$
\int_{-\omega_c}^{\omega_c} \mathrm{d}\xi \, \frac{\tanh(\beta\xi/2)}{2\xi} \int_{S_F(\xi)} \frac{\mathrm{d}\hat{\boldsymbol{k}}}{|S_F|} \frac{\rho_\xi \bar{v}_F}{v_F(\hat{\boldsymbol{k}})} \sum_{s,s'} \Gamma_{\hat{\boldsymbol{k}}_1 s_1 s_1'; \hat{\boldsymbol{k}} s s'} \Delta_{ss'}(\hat{\boldsymbol{k}}) = -\Delta_{s_1 s_1'}(\hat{\boldsymbol{k}}_1). \quad (2.19)
$$

The integrand above is a function of ξ, but it can be replaced by a power series in ξ, motivated by the factor of $\tanh(\beta\xi/2)/(2\xi)$ that decays with ξ. In the limit $\beta\omega_c \to \infty$, only the leading term this expansion (i.e. when evaluating the innermost integral at $\xi = 0$) yields a (log-)divergence. This divergence stems from

$$
\int_{-\omega_c}^{\omega_c} \mathrm{d}\xi \, \frac{\tanh(\beta\xi/2)}{2\xi} \approx \ln\left(\frac{2\beta\omega_c e^\gamma}{\pi} \right), \quad (2.20)
$$

as obtained when neglecting subleading terms that are regular in the aforementioned limit[7]. Above, $\gamma \approx 0.5772$ is the Euler–Mascheroni constant.

Finally, if $\Delta_{ss'}(\boldsymbol{k})$ is an eigenfunction of the remaining ($\xi = 0$) integral equation associated with the negative eigenvalue $-|\lambda|$, the critical temperature follows from

$$
\begin{aligned}
-\ln\left(\frac{2\omega_c e^\gamma}{\pi k_B T_c} \right) |\lambda| = -1 \Rightarrow \\
T_c = \frac{2e^\gamma}{\pi} \frac{\omega_c}{k_B} e^{-\frac{1}{|\lambda|}}.
\end{aligned} \quad (2.21)
$$

Here the numerical prefactor $2e^\gamma/\pi \approx 1.13$ is recognised from BCS theory [58].

---

[7] After a partial integration we have $\int_{-\omega_c}^{\omega_c} \mathrm{d}\xi \, \tanh(\beta\xi/2)/(2\xi) = \ln(\beta\omega_c/2) \tanh(\beta\omega_c/2) + \ln(4e^\gamma/\pi) + \int_{\beta\omega_c/2}^{\infty} \mathrm{d}x \, \ln(x)/\cosh^2(x)$.

2.2.4 Weak-Coupling Theory

To make use of the generalised gap equation derived above, we turn to the main assumption of the Kohn–Luttinger approach, namely that the on-site density-density interaction, labelled U like in Eq. (2.2), is weak compared to the electronic bandwidth $U \ll \omega_c$, called the weak-coupling limit[8]. This limit is perfectly valid mathematically; how it applies to real materials is discussed in Section 2.6 and Subsection 3.4.3. The superconducting order parameter with the highest T_c is given by the eigenfunction of Eq. (2.19) associated with the most negative eigenvalue. To determine it, our strategy is to treat the irreducible vertex Γ perturbatively in the interaction strength U, specifically to one-loop (leading) order $\mathcal{O}(U^2)$. Redefining the vertex to be dimensionless for convenience, the gap equation reads [15]:

$$\int_{S_F} \frac{\mathrm{d}\boldsymbol{k}'}{|S_F|} \bar{\Gamma}_{\boldsymbol{k},\boldsymbol{k}'} \psi(\boldsymbol{k}') = \lambda \psi(\boldsymbol{k}), \tag{2.22}$$

$$\bar{\Gamma}_{\boldsymbol{k},\boldsymbol{k}'} = \rho_0 U^2 \sqrt{\frac{\bar{v}_F}{v_F(\boldsymbol{k})}} \Gamma^{(2)}_{\boldsymbol{k},\boldsymbol{k}'} \sqrt{\frac{\bar{v}_F}{v_F(\boldsymbol{k}')}}. \tag{2.23}$$

The above integral runs over the Fermi surface (of area $|S_F|$), and $\bar{\Gamma}_{\boldsymbol{k},\boldsymbol{k}'}$ is the dimensionless irreducible vertex with spin indices left implicit. We also re-introduced the Fermi velocity, the average Fermi velocity, and the density of states at the Fermi level $\xi = 0$ as (cf. Eqs. (2.16), (2.17), and (2.18))

$$v_F(\boldsymbol{k}) = |\nabla \xi_{\boldsymbol{k}}|, \quad \bar{v}_F = \left(\int_{S_F} \frac{\mathrm{d}\boldsymbol{k}}{|S_F|} \frac{1}{v_F(\boldsymbol{k})} \right)^{-1}, \quad \rho_0 = \frac{|S_F|}{\bar{v}_F (2\pi)^3}, \tag{2.24}$$

respectively. Finally, $\Gamma^{(2)}_{\boldsymbol{k},\boldsymbol{k}'}$ is the irreducible vertex at second order, for which the diagrams in both the singlet and triplet spin channels are shown in Fig. 2.3. The second-order diagrams of Fig. 2.3 are readily evaluated:

$$\Gamma^{(2)}_{\boldsymbol{k},\boldsymbol{k}'} = \begin{cases} +\chi(\boldsymbol{k}+\boldsymbol{k}') & \text{spin singlet} \\ -\chi(\boldsymbol{k}-\boldsymbol{k}') & \text{spin triplet} \end{cases}, \tag{2.25}$$

---

[8] For a model defined on the lattice, the weak-coupling limit is $U \ll t$ where t is on the scale of the (maximal) electron hopping terms, cf. t in Eq. (2.2).

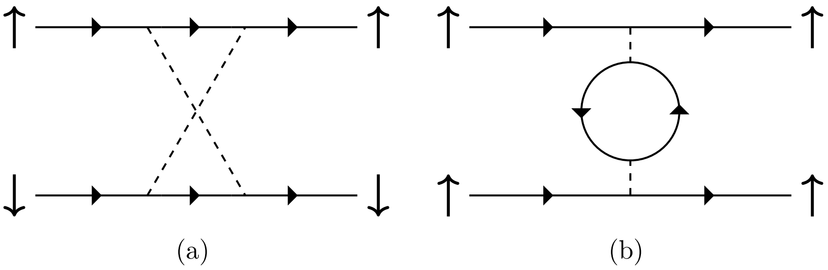

Figure 2.3: The second-order diagrams in the (a) singlet and (b) triplet channel. Solid lines are bare electron propagators, dashed lines denote the Hubbard interaction, and vertical arrows denote spins.

as expressed in terms of the the density-density response function, or the *Lindhard function*, $\chi(\boldsymbol{q})$ given by [15, 60]

$$\begin{aligned}\chi(\boldsymbol{q}) &= -\frac{1}{\beta}\sum_{\boldsymbol{p},n}\frac{1}{i\omega_n - \xi_{\boldsymbol{p}}}\frac{1}{i\omega_n - \xi_{\boldsymbol{p}+\boldsymbol{q}}} \\ &= -\int_{\mathrm{BZ}}\frac{\mathrm{d}\boldsymbol{p}}{(2\pi)^3}\frac{f(\xi_{\boldsymbol{p}}) - f(\xi_{\boldsymbol{p}+\boldsymbol{q}})}{\xi_{\boldsymbol{p}} - \xi_{\boldsymbol{p}+\boldsymbol{q}}},\end{aligned} \tag{2.26}$$

when taking the continuum limit in the transition from the first to the second line. The Matsubara sum was carried out in analogy to Eq. (2.14).

In the singlet channel one must also account for the (trivial) first-order contribution, as readily shown in Fig. 2.1 (b). Since the first-order vertex $\Gamma^{(1)}$ is positive semidefinite and has no $\boldsymbol{k}$-structure, an overall finite-T_c solution to the gap equation must belong to the kernel $\mathrm{Ker}(\Gamma^{(1)})$ to evade the repulsion at first order. In turn, this implies that for any non-degenerate order parameter:

$$\psi(\boldsymbol{k}) \in \mathrm{Ker}(\Gamma^{(1)}) \;\; \Rightarrow \;\; \int_{S_F}\mathrm{d}\boldsymbol{k}\;\psi(\boldsymbol{k}) = 0. \tag{2.27}$$

One may take $\psi(\boldsymbol{k}) \in \mathrm{Ker}(\Gamma^{(1)})$ as a defining criterion of the "unconventional sector". Note that this set excludes the BCS s-wave solution, which does not change sign over the Fermi surface.

To summarise, an eigenfunction $\psi(\boldsymbol{k})$ of the integral equation in Eq. (2.22) associated with a negative eigenvalue λ signals the onset of superconductivity with an order parameter $\Delta(\boldsymbol{k})$ below a critical temperature T_c,

$$\Delta(\boldsymbol{k}) = T_c\sqrt{\frac{v_F(\boldsymbol{k})}{\bar{v}_F}}\psi(\boldsymbol{k}), \qquad T_c \sim We^{-1/|\lambda|}, \tag{2.28}$$

where $W \equiv \frac{2e^{\gamma}}{\pi}\frac{\omega_c}{k_B}$ is on the order of the electronic bandwidth, as per Eq. (2.21). We define the ground state as the order parameter with the highest T_c, i.e. the solution with the most negative eigenvalue.

2.3 An Anisotropic Hubbard Model

2.3.1 The Model and its Fermi Surface

To employ the formalism introduced in the previous section, we shall focus on an anisotropic three-dimensional Hubbard model, previously studied in Refs. [63, 64]. We allow electrons at chemical potential μ to hop on a primitive tetragonal lattice (see Subsection 2.3.2 and Fig. 2.5) defined by an in-plane (out-of-plane) hopping strength $t_{\parallel}$ ($t_{\perp}$). The electrons are subject to an on-site repulsive density-density interaction $U > 0$. The Hamiltonian is given by (cf. Eq. (2.2))

$$H = -t_{\parallel} \sum_{s,\langle ij\rangle_{\parallel}} c^{\dagger}_{is}c_{js} - t_{\perp} \sum_{s,\langle ij\rangle_{\perp}} c^{\dagger}_{is}c_{js} - \mu \sum_{s,i} n_{is} + U \sum_{i} n_{i\uparrow}n_{i\downarrow}. \tag{2.29}$$

Here c_{is} ($c^{\dagger}_{is}$) annihilates (creates) an electron of spin s on lattice site i, $n_{is} = c^{\dagger}_{is}c_{is}$ is the density operator, and $\langle\cdot\rangle_{\parallel}$ ($\langle\cdot\rangle_{\perp}$) denotes in-plane (out-of-plane) nearest neighbouring sites. The non-interacting part of the Hamiltonian yields the single-particle dispersion in momentum space:

$$\xi_{\boldsymbol{k}} = -2t_{\parallel}\left(\cos k_x + \cos k_y\right) - 2t_{\perp}\cos k_z - \mu. \tag{2.30}$$

The electron filling is defined as the expectation value

$$n = \langle n_{\boldsymbol{k}s}\rangle = 2\int_{\mathrm{BZ}} \frac{\mathrm{d}\boldsymbol{k}}{(2\pi)^3} f(\xi_{\boldsymbol{k}}), \tag{2.31}$$

where the factor of 2 comes from the sum over spins, $f(E) = (1+\exp(\beta E))^{-1}$ is the Fermi function, and the 3D Brillouin zone is $\mathrm{BZ} = [-\pi,\pi]^3$. Due to the presence of particle-hole symmetry[9], it suffices to study the region below half-filling $n \in [0,1]$ since the order at filling $2-n$ would be identical by this symmetry. The relationship between n, μ, and $t_{\perp}$ for fixed $t_{\parallel} = 1$ is shown in Fig. 2.4.

---

[9] The particle-hole symmetry exchanges the roles of electrons and holes and is defined as an antiunitary operator that anti-commutes with the single-particle Bogoliubov–de Gennes Hamiltonian [65]. We elaborate on the role of this symmetry in superconductors in Sections 4.1 and 4.2.

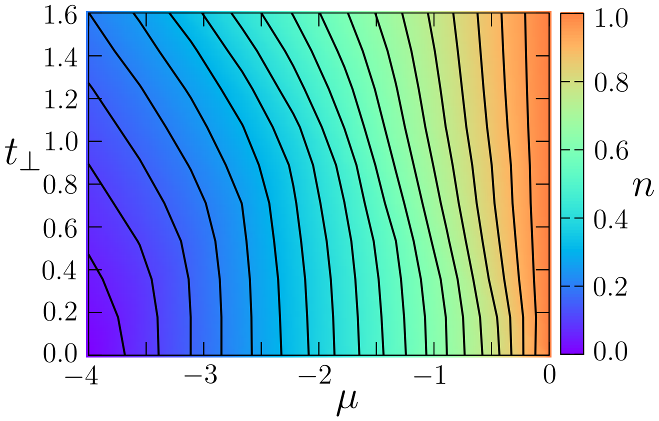

Figure 2.4: Heat map of the electron filling $n(\mu, t_\perp, t_\parallel = 1)$, defined in Eq. (2.31), as a function of the chemical potential μ and the out-of-plane hopping $t_\perp$. Black lines are isolines for n.

The Fermi surface derived from the model in Eq. (2.29), defined by $\xi_{\boldsymbol{k}} = 0$, takes on four topologically distinct shapes below half-filling. To see this, we introduce the two *van Hove* parameter lines

$$\mu_z = -4t_\parallel + 2t_\perp, \qquad \mu_{xy} = -2t_\perp, \tag{2.32}$$

defined by the values of the chemical potential that make the Fermi surface touch the BZ boundaries $|k_z| = \pi$ or $|k_x| = |k_y| = \pi$, respectively. A van Hove singularity marks a singularity in the density of states and takes place when the chemical potential is tuned to an extremum or saddle-point of the dispersion. Examples of the various Fermi surfaces are shown in the phase diagram that we determine numerically and comment on in Subsection 2.5.2, see Fig. 2.9. The shapes include one closed and three open Fermi surfaces. Tuning $t_\perp/t_\parallel$ or $\mu/t_\parallel$ across any of the van Hove lines defined above produces a *Lifshitz transition* [66], at which the topology of the Fermi surface is altered.

2.3.2 Tetragonal Crystal Symmetries

The Hamiltonian of Eq. (2.3) is characterised by a symmetry group composed of a crystal point group G, spin-rotation symmetry SU(2), time-reversal symmetry $\mathcal{T}$, and a gauge symmetry U(1). While the U(1) symmetry is fundamentally broken in the superconducting state, any non-degenerate order parameter $\Delta(\boldsymbol{k})$

respects the remaining symmetries as dictated by invariance of the Hamiltonian under these in our framework [11]. This is in fact already encoded in Eq. (2.22) – in the symmetry properties of the irreducible vertex. Order parameters that break crystal symmetries are beyond the scope of the leading singularity in the normal phase approach considered here. Within a degenerate subspace of orders, however, both time-reversal and point group symmetries can be broken, as discussed in Subsections 2.5.3 and 2.5.4.

The model defined in Eq. (2.29) (and the model studied in Chapter 3) is defined on a tetragonal lattice. A primitive tetragonal lattice is characterised by the in-plane lattice spacing a and the out-of-plane lattice spacing c, as shown in Fig. 2.5. The order parameter deriving from a model defined on such a lattice thus belongs to one of the ten *irreducible representations* (irreps) of the tetragonal point group $G = D_{4h}$ in order to respect the spatial symmetries imposed by the crystal [11]. The irreps have well-defined properties under rotations and reflections allowed by the lattice. Here, we characterise key properties of the order parameters belonging to the various irreps in reciprocal space[10].

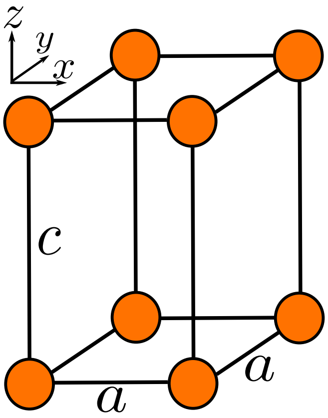

Figure 2.5: Unit cell of the primitive tetragonal lattice, with in-plane lattice constant a and out-of-plane lattice constant c.

A convenient and standardised nomenclature for the order parameter is given by the so-called $\boldsymbol{d}$-vector basis, introduced by Balian and Werthamer (BW) [7].

---

[10] As commented on in Section 2.2, we adopt the convention of scaling crystal momenta k_x and k_y by the lattice constant a, and k_z by the lattice constant c.

Following this convention, the order parameter is parametrised by the scalar spin singlet component d_0, and the vector spin triplet $\boldsymbol{d}$ according to

$$\begin{pmatrix} \Delta_{\uparrow\uparrow}(\boldsymbol{k}) & \Delta_{\uparrow\downarrow}(\boldsymbol{k}) \\ \Delta_{\downarrow\uparrow}(\boldsymbol{k}) & \Delta_{\downarrow\downarrow}(\boldsymbol{k}) \end{pmatrix} = \frac{1}{\sqrt{2}} \begin{pmatrix} -d_x(\boldsymbol{k}) + i d_y(\boldsymbol{k}) & d_z(\boldsymbol{k}) + d_0(\boldsymbol{k}) \\ d_z(\boldsymbol{k}) - d_0(\boldsymbol{k}) & d_x(\boldsymbol{k}) + i d_y(\boldsymbol{k}) \end{pmatrix}, \tag{2.33}$$

where $\Delta_{ss'}(\boldsymbol{k})$ is the order parameter with spin indices s and s'. As ensured by fermionic asymmetry of the two-particle wavefunction (the Pauli principle), the components transform under the parity operation as

$$d_0(-\boldsymbol{k}) = d_0(\boldsymbol{k}), \quad \text{and} \quad \boldsymbol{d}(-\boldsymbol{k}) = -\boldsymbol{d}(\boldsymbol{k}), \tag{2.34}$$

respectively. Table 2.1 summarises the irreps of the tetragonal point group and gives examples of associated order parameter structures in the $\boldsymbol{d}$-vector basis.

In general, the order parameter in any given irrep can be expressed as an infinite sum of its Fourier components (called "lattice harmonics"). In some cases this sum is dominated by the fundamental lattice harmonic. For instance, in the case of the B_{1g} irrep (see Table 2.1), the fundamental lattice harmonic is $\cos(k_x) - \cos(k_y)$, which in the case of small k_x and k_y often is denoted by $d_{x^2-y^2}$ in the literature. This notation is inspired by orbital physics, where the letters $s,\ p,\ d, \ldots$ refer to Cooper pairs of relative angular momentum $l = 0, 1, 2, \ldots$ in a rotational invariant system, respectively. Fermionic asymmetry dictates the Cooper pair to have spins in a singlet or triplet state for even or odd l, respectively. Generally, the solutions to Eq. (2.19) will have contributions from higher lattice harmonics, but for convenience we coin the simplified orbital notation irrespectively in this thesis.

The orbital notation gives valuable information about the nodal structure of the order parameter as imposed by the tetragonal symmetries. For example, $d_{x^2-y^2}$ has nodes along $|k_x| = |k_y|$, and d_{xy} has nodes along $k_x = 0$ and $k_y = 0$. Such nodes – imposed by symmetry – will be denoted by "robust" nodes. Nodes occurring from the interplay of higher lattice harmonics and the particular shape of the Fermi surface will be denoted by "accidental" nodes. In Fig. 2.6 we show simple examples of unconventional order parameters in the 2D Brillouin zone BZ $= [-\pi, \pi]^2$ with a cylindrical Fermi surface drawn in black for reference.

Table 2.1: Irreducible representations (irreps) of the tetragonal point group D_{4h} [11]. Even-parity representations (subscript g) are described by a scalar (d_0) order parameter, whereas odd-parity (subscript u) order parameters are described by a vector ($\boldsymbol{d}$). The second column provides order parameter examples. Here, f_j should be associated with any function that transforms like $\sin k_j$ under the point group operations and f_j^2 with any function that transforms like $\cos k_j$ for $j = x, y, z$. Irreps E_u and E_g are two-dimensional and can favour time-reversal symmetry breaking (TRSB) order parameters as indicated.

Irrep	Order parameter	Name	TRSB
A_{1g}	$d_0(\boldsymbol{k}) = 1,$ $f_x^2 + f_y^2$	s-wave (BCS), generalised s-wave	No
A_{2g}	$d_0(\boldsymbol{k}) = f_x f_y (f_x^2 - f_y^2)$	g-wave	No
B_{1g}	$d_0(\boldsymbol{k}) = f_x^2 - f_y^2$	d-wave	No
B_{2g}	$d_0(\boldsymbol{k}) = f_x f_y$	d-wave	No
E_g	$d_0(\boldsymbol{k}) = f_z (f_x \pm i f_y)$	chiral d-wave	Yes
A_{1u}	$\boldsymbol{d}(\boldsymbol{k}) = f_x f_y f_z (f_x^2 - f_y^2) \hat{z},$ $f_x \hat{x} + f_y \hat{y}$	h-wave, helical p-wave (BW)	No
A_{2u}	$\boldsymbol{d}(\boldsymbol{k}) = f_z \hat{z},$ $f_y \hat{x} - f_x \hat{y}$	p-wave, helical p-wave	No
B_{1u}	$\boldsymbol{d}(\boldsymbol{k}) = f_x f_y f_z \hat{z},$ $f_x \hat{x} - f_y \hat{y}$	f-wave, helical p-wave	No
B_{2u}	$\boldsymbol{d}(\boldsymbol{k}) = f_z (f_x^2 - f_y^2) \hat{z},$ $f_y \hat{x} + f_x \hat{y}$	f-wave, helical p-wave	No
E_u	$\boldsymbol{d}(\boldsymbol{k}) = (f_x \pm i f_y) \hat{z}$	chiral p-wave (ABM)	Yes

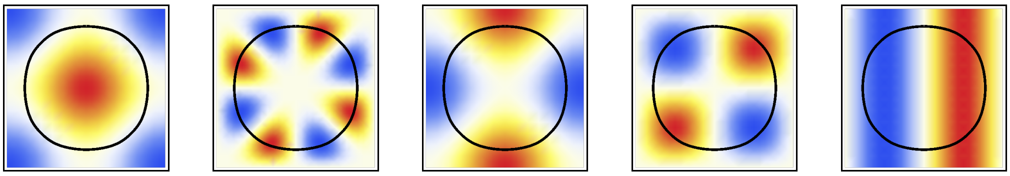
(a) (b) (c) (d) (e)

Figure 2.6: Examples of possible unconventional order parameters consistent with the tetragonal lattice symmetries. The colours reflect the signed magnitude of the order parameter in the 2D BZ, with a cylindrical Fermi surface shown in black for reference. (a) $\cos k_x + \cos k_y$ (A_{1g}), (b) $\sin k_x \sin k_y (\cos k_x - \cos k_y)$ (A_{2g}), (c) $\cos k_x - \cos k_y$ (B_{1g}), (d) $\sin k_x \sin k_y$ (B_{2g}), (e) $\sin k_x$ (E_u).

It should be emphasised that the order parameters provided in the second column of Table 2.1 are merely selectively chosen examples [11] relevant for the models of this thesis. For example, the odd-k_z order parameter $\boldsymbol{d}(\boldsymbol{k}) = f_z(\hat{x} \pm i\hat{y})$, where f_z is any function transforming like $\sin k_z$ under the point group operations, would be another example of an order parameter belonging to the E_u irrep. It should also be noted that irreps E_u and E_g are two-dimensional, whereas the remaining eight irreps are one-dimensional. A consequence of this is that order parameters belonging to either E_u or E_g can favour complex (chiral) combinations of orders to yield an increase in the superconducting condensation energy (see Eq. (2.46)). Complex order parameters are time-reversal symmetry breaking (TRSB), as indicated in the fourth column of Table 2.1. Complex order parameters will be discussed further in Subsection 2.5.4.

Finally, in the case of a single-band model, which is the case throughout this chapter, the $\boldsymbol{d}$-vector is free to rotate. Phrased differently, the absence of spin-orbit coupling (SOC) makes the three spin triplet components d_x, d_y, and d_z degenerate. The presence of SOC pins the direction of $\boldsymbol{d}$ and splits this degeneracy, as we shall elaborate on in the next chapter.

2.4 The Low-Filling Limit

Consider the model in Eq. (2.29) at low filling, such that $n \ll 1$, where n is the electron filling defined in Eq. (2.31). Equivalently, one can define the low-filling limit by $k_F \ll \pi$, where k_F is the Fermi (crystal) momentum. In this limit, the equation defining the Fermi surface, $\xi_{\boldsymbol{k}} = 0$, can be well approximated by expanding $\xi_{\boldsymbol{k}}$ in k_i for $i = x, y, z$. To leading order, the Fermi surface becomes rotationally symmetric around the $\hat{z}$-axis:

$$k_x^2 + k_y^2 + \frac{t_\perp}{t_\parallel} k_z^2 = k_F^2, \qquad k_F = \sqrt{4 + (\mu + 2t_\perp)/t_\parallel}. \tag{2.35}$$

The expression for k_F gives the relationship between the Fermi momentum, the chemical potential, and the electron filling when combined with Fig. 2.4. The surface defined by Eq. (2.35) is either a prolate spheroid or an oblate spheroid for $t_\parallel > t_\perp$ or $t_\parallel < t_\perp$, respectively. Before elaborating on the case of a spheroidal Fermi surface, we first discuss exact results established in the instance of a spherical Fermi surface, $t_{\parallel} = t_{\perp}$.

2.4.1 Spherical Fermi Surface

Defining $t \equiv t_{\parallel} = t_{\perp}$ in this subsection, the Lindhard function of Eq. (2.26) in the low-filling limit evaluates to [15, 43]:

$$\begin{aligned} \chi(\boldsymbol{q}) &= \rho_0 g\Big(\frac{q}{2k_F}\Big), \\ g(x) &= \frac{1}{2} + \frac{1-x^2}{4x} \ln\left|\frac{1+x}{1-x}\right|, \\ \rho_0 &= \frac{k_F}{4\pi^2 t}, \end{aligned} \tag{2.36}$$

with $q = |\boldsymbol{q}|$. The gap equation for even/odd angular momentum,

$$\pm \frac{\rho_0 U^2}{4\pi} \int \mathrm{d}\Omega_{\boldsymbol{k}'}\ \chi(\boldsymbol{k} \pm \boldsymbol{k}')\psi(\boldsymbol{k}') = \lambda\psi(\boldsymbol{k}), \tag{2.37}$$

as per Eq. (2.22), permits exact solutions. Above, the symbol $\mathrm{d}\Omega_{\boldsymbol{k}'}$ is an infinitesimal Fermi surface element around the direction of $\boldsymbol{k}'$. The solutions to Eq. (2.37) are the spherical harmonics, $\psi(\boldsymbol{k}) = Y_l^m(\theta, \phi)$, with a $(2l+1)$-fold degeneracy in m, where we parametrised $\boldsymbol{k} = k_F(\sin\theta\cos\phi,\ \sin\theta\sin\phi,\ \cos\theta)^T$. To obtain the exact eigenvalues, and hence the critical temperature, we express $\chi(\boldsymbol{q})$ as a power series in $q/(2k_F)$, perform the integration term by term[11], and resum the series. For instance, for odd l:

$$\begin{aligned} -\frac{\rho_0 U^2}{4\pi} \int \mathrm{d}\Omega_{\boldsymbol{k}'}\ \chi(\boldsymbol{k} - \boldsymbol{k}')Y_l^m(\theta', \phi') &= -\frac{\rho_0 U^2}{4\pi} \sum_{n=0}^{\infty} \int \mathrm{d}\Omega_{\boldsymbol{k}'}\ \chi^{(n)}(\boldsymbol{k} - \boldsymbol{k}')Y_l^m(\theta', \phi') \\ &= (\rho_0 U)^2 \sum_{n=0}^{\infty} \tilde{\lambda}_l^{(n)} Y_l^m(\theta, \phi) \\ &= (\rho_0 U)^2 \tilde{\lambda}_l Y_l^m(\theta, \phi). \end{aligned} \tag{2.38}$$

Above, the symbol $\chi^{(n)}(\boldsymbol{q}) = -\frac{\rho_0}{4n^2-1}\left[q/(2k_F)\right]^{2n}$ was introduced. The “partial” eigenvalues $\tilde{\lambda}_l^{(n)}$ appearing above turn out to have the structure $\tilde{\lambda}_l^{(n)} = P_l(n)/Q_{l+3}(n)$, where $P_l(n)$ ($Q_l(n)$) is an lth order polynomial in n, the particular form of which is not instructive to discuss here.

---

[11] This works because the spherical harmonics are eigenfunctions of the integral equation at all orders in the $q/(2k_F)$ expansion, individually.

Table 2.2: Exact pairing eigenvalues to one-loop order with a spherical Fermi surface. The first three values here were originally reported by Ref. [67].

Pairing (l)	$\tilde{\lambda}_l = \lambda_l/(\rho_0 U)^2$
s-wave (0)	$+\frac{1}{3}(1+\ln 4) \approx +0.80$
p-wave (1)	$-\frac{1}{5}(\ln 4 - 1) \approx -0.077$
d-wave (2)	$-\frac{1}{105}(16 - 11\ln 4) \approx -0.0072$
f-wave (3)	$-\frac{1}{945}(69\ln 4 - 94) \approx -0.0018$
g-wave (4)	$-\frac{1}{1386}(109 - 78\ln 4) \approx -0.00063$
h-wave (5)	$-\frac{1}{38610}(1770\ln 4 - 2443) \approx -0.00028$
i-wave (6)	$-\frac{1}{64350}(3461 - 2490\ln 4) \approx -0.00014$

The first seven exact eigenvalues $\lambda_l = (\rho_0 U)^2 \tilde{\lambda}_l$ are listed in Table 2.2, demonstrating that the leading instability is p-wave in the weak-coupling low-filling limit. The critical temperature of the pairing states with $l > 1$ decays with l and eventually approaches the law reported by Kohn and Luttinger, cf. Eq. (2.1). The first three eigenvalues of Table 2.2 were initially obtained, by contour integration, in Ref. [67].

In principle, one should also consider the competition with other instabilities at finite momentum, like charge-density and spin-density waves. However, in the weak-coupling limit, the Cooper instability has been shown by renormalisation-group methods to be the only relevant one [57]. Moreover, (anti)ferromagnetic order is also irrelevant at low filling in the weakly coupled Hubbard model [45, 47].

2.4.2 Spheroidal Fermi Surface

Above, it was established that the three-fold degenerate p-wave pairing channel (eigenfunctions $Y_{l=1}^{m}$ for $m = -1, 0, 1$) is favoured in the low-filling weak-coupling limit. As soon as we tune the parameters away from the particular case of $t_{\parallel} = t_{\perp}$, the three-fold degeneracy of the ground state is expected to be lifted. However, how this degeneracy lifts – i.e. determining which states are favoured for $t_{\perp} < t_{\parallel}$ and which for $t_{\perp} > t_{\parallel}$ – is non-trivial. It would be of interest to establish the nature of the eigenvalue splitting away from this parameter line as a function of the Fermi surface warping. The splitting may even have measurable consequences in superfluid helium-3, as discussed in the next subsection.

The spheroidal Fermi surface when $t_\perp \neq t_\|$ can be parametrised by the spheroid *eccentricity*, which we denote by ν ($\tilde{\nu}$) in the prolate (oblate) regime. In Table 2.3 we have summarised the Fermi velocity and the Fermi surface area in these cases. When $t_\perp \neq t_\|$ the denominator of Eq. (2.26) at low filling is modified compared to the spherical case:

Table 2.3: Fermi surface eccentricity, Fermi velocity, and Fermi surface area in the prolate ($t_\| > t_\perp$) and oblate ($t_\| < t_\perp$) regime at low filling. Here θ is the zenith angle.

Regime	Eccentricity	$v_F(\boldsymbol{k})$	$\lvert S_F\rvert$
$t_\| > t_\perp$	$\nu \equiv \sqrt{1-(\frac{t_\perp}{t_\|})^2}$	$2k_F t_\| \sqrt{1-\nu^2\cos^2\theta}$	$2\pi k_F^2(1+\nu^{-1}\arcsin\nu)$
$t_\| < t_\perp$	$\tilde{\nu} \equiv \sqrt{1-(\frac{t_\|}{t_\perp})^2}$	$2k_F t_\| \sqrt{1+\frac{\tilde{\nu}^2}{1-\tilde{\nu}^2}\cos^2\theta}$	$2\pi k_F^2(1+\frac{1}{2\tilde{\nu}}\ln\frac{1+\tilde{\nu}}{1-\tilde{\nu}})$

$$\xi_{\boldsymbol{p}} - \xi_{\boldsymbol{p}+\boldsymbol{q}} = -t_\| \big(q_x^2 + q_y^2 + \frac{t_\perp}{t_\|} q_z^2 + 2\big[q_x p_x + q_y p_y + \frac{t_\perp}{t_\|} q_z p_z\big] + \mathcal{O}(p_i, q_i)^4 \big). \tag{2.39}$$

This expansion is justified at low filling since the Fermi momentum is small compared to π. By rescaling the $\hat{z}$-axis according to $k_z \to \sqrt{t_\|/t_\perp}\,k_z$, we can bring Eq. (2.39) back to the form of the spherical case at the expense of including a Jacobian factor of $\sqrt{t_\|/t_\perp}$ in the Fermi surface integrals. We combine this with the various elements of Table 2.3 in Eq. (2.22) to obtain the dimensionless two-particle vertex in rescaled coordinates, stated here in the triplet channel:

$$\bar{\Gamma}^{\text{prolate}}_{\boldsymbol{k},\boldsymbol{k}'} = -\rho_0 U^2 \frac{1+\nu^{-1}\arcsin\nu}{2(1-\nu^2)} \frac{\chi(\boldsymbol{k}-\boldsymbol{k}')}{[(1-\nu^2\cos^2\theta)\,(1-\nu^2\cos^2\theta')]^{1/4}}, \tag{2.40}$$

$$\bar{\Gamma}^{\text{oblate}}_{\boldsymbol{k},\boldsymbol{k}'} = -\rho_0 U^2 \frac{1-\tilde{\nu}^2}{2} \left[1 + \frac{1}{2\tilde{\nu}} \ln\frac{1+\tilde{\nu}}{1-\tilde{\nu}}\right] \frac{\chi(\boldsymbol{k}-\boldsymbol{k}')}{\big[\big(1+\frac{\tilde{\nu}^2}{1-\tilde{\nu}^2}\cos^2\theta\big)\,\big(1+\frac{\tilde{\nu}^2}{1-\tilde{\nu}^2}\cos^2\theta'\big)\big]^{1/4}}, \tag{2.41}$$

where χ is the same function as in the spherical case (Eq. (2.36)).

A common way to solve integral equations, like Eq. (2.22) in the present case, is to expand the integration kernel and its eigenfunctions in a basis of orthogonal polynomials [68], with further details given in Appendix A. Given that no ϕ'-dependence was introduced in the various new factors of Eq. (2.40) and (2.41) compared to the spherical case, we apply the reasonable ansätze

$$\psi_{p_x \pm ip_y}(\theta, \phi) = \tilde{\psi}(\theta) \exp(\pm i\phi), \tag{2.42}$$

$$\psi_{p_z}(\theta, \phi) = \tilde{\psi}(\theta), \tag{2.43}$$

in the two sectors of interest, corresponding to $m = \pm 1$ and $m = 0$, respectively. When inserting this and integrating over ϕ', we are left with a one-variable integral equation. By further expanding both the integration kernel $\bar{\Gamma}_{\boldsymbol{k},\boldsymbol{k}'}$ and the solutions $\tilde{\psi}$ in orthogonal polynomials, the continuous problem (integral equation) maps onto an infinite-dimensional matrix eigenvalue problem that we solve numerically by truncation.

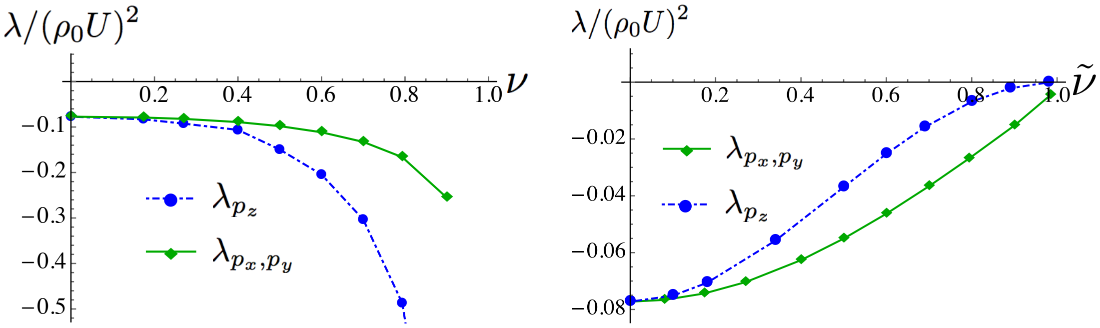

(a) (b)

Figure 2.7: Pairing eigenvalues in the (a) prolate and (b) oblate regime as a function of the Fermi surface eccentricity at low filling. The p-wave value of Table 2.2 is recovered at $\nu, \tilde{\nu} = 0$.

The resulting eigenvalues are shown in Fig. 2.7, revealing that the p_z ($\{p_x, p_y\}$) order is favoured in the prolate (oblate) regime. Corresponding eigenfunctions for three values of the eccentricity are shown in Fig. 2.8, demonstrating that the eigenfunctions barely receive any corrections compared to the spherical harmonics, even for eccentricities close to 1.

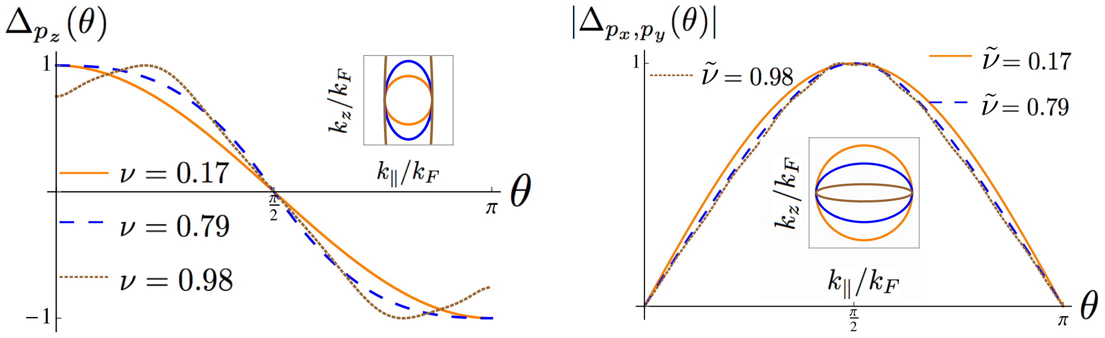

(a) (b)

Figure 2.8: Eigenfunctions in the (a) prolate and (b) oblate regime as a function of the zenith angle at low filling. The insets show projections of the Fermi surfaces to illustrate the warping.

The reason why T_c is enhanced in the prolate case and suppressed in the oblate case can be seen from the θ-dependent factors of Eqs. (2.40) and (2.41). These factors, coming from the inverse Fermi velocity, promote vertical $\theta = 0, \pi$ (horizontal $\theta = \pi/2$) pairing increasingly in ν ($\tilde{\nu}$) in the prolate (oblate) regime. In the prolate regime these factors (which are $\geqslant 1$) contribute to enhanced pairing, whereas the pairing is suppressed in the oblate regime (since the factors are $\leqslant 1$ here). Intuitively, the above observation can be understood in terms of the Fermi surface *self-nesting wave-vectors*, defined as the $\boldsymbol{Q}$ at which the susceptibility peaks. In the triplet channel it is advantageous to have

$$\arg[\Delta(\boldsymbol{k} + \boldsymbol{Q})] = \arg[\Delta(\boldsymbol{k})], \tag{2.44}$$

with $\boldsymbol{k}, \boldsymbol{k} + \boldsymbol{Q} \in S_F$, to achieve the most negative pairing eigenvalue. For a $\{p_x, p_y\}$ order parameter this is achieved with $\boldsymbol{Q} \parallel \hat{z}$, which for a prolate spheroid is also the direction promoting the largest Fermi surface self-overlap when shifting by $\boldsymbol{Q}$. For a p_z order parameter the condition of Eq. (2.44) is satisfied with $\boldsymbol{Q} \perp \hat{z}$, but the Fermi surface self-overlap is reduced relative to the spherical case here.

The splitting of orders away from the spherical case is in principle detectable experimentally via specific heat measurements. While the p_z order parameter has a horizontal line node, the $p_x \pm ip_y$ orders have two point nodes, which yield T^2 and T^3 power laws, respectively, for the electronic specific heat at low temperature compared to the maximal gap[12] (we elaborate on this in Subsection 3.5.1 in the context of Sr_2RuO_4). Alternatively, different dimensionality of the gap nodes implies different values of the specific heat jump at T_c, associated with the release of entropy when the gap opens. The specific heat jump, normalised by the normal-state value, is calculated from averages of the order parameter over the Fermi surface [69]. Using the spherical harmonics as reasonable approximations to the prolate and oblate eigenstates at small eccentricities, the specific heat jump evaluates to

$$\left.\frac{\Delta C}{C_n}\right|_{T=T_c} = \frac{12}{7\zeta(3)} \frac{\left\langle |\psi(\boldsymbol{k})|^2 \right\rangle_{S_F}^2}{\left\langle |\psi(\boldsymbol{k})|^4 \right\rangle_{S_F}} = \begin{cases} \frac{20}{21\zeta(3)} \approx 0.792 & \text{for } \psi(\boldsymbol{k}) = \cos\theta \\ \frac{10}{7\zeta(3)} \approx 1.19 & \text{for } \psi(\boldsymbol{k}) = e^{\pm i\phi}\sin\theta \end{cases}, \tag{2.45}$$

where ζ is the Riemann zeta function, with $\zeta(3) \approx 1.202$, and where $\langle\cdot\rangle_{S_F}$ is an average over the Fermi surface. The corrections to Eq. (2.45), due to the Fermi surface warping, are second order in ν ($\tilde{\nu}$).

2.4.3 Analogy to Helium-3

In contrast to the electronic model on the lattice explored in this chapter, helium-3 (^{3}He) is a neutral fluid that undergoes a phase transition from a Fermi liquid above $T_c = 2.7$ mK to a superfluid below T_c [4, 8]. As a function of temperature and pressure, the superfluid phase diagram of ^{3}He exhibits two distinct p-wave phases, as identified with NMR (we return to this probe in Subsection 3.5.3). At a pressure of around 30 bars and temperatures close to T_c a chiral p-wave phase with $\boldsymbol{d}(\boldsymbol{k}) = (k_x \pm ik_y)\hat{z}$, known as the A-phase or the Anderson–Brinkman–Morel (ABM) phase [5, 6], is realised. At lower pressure and temperature, an isotropic p-wave phase with $\boldsymbol{d}(\boldsymbol{k}) = k_x\hat{x} + k_y\hat{y} + k_z\hat{z}$, known as the B-phase or the Balian–Werthamer phase (BW) [7] phase, is realised. The BW phase is an analogue of the helical p-wave state belonging to the A_{1u} irrep on the tetragonal lattice, as per Table 2.1.

Interestingly, in a superfluid that by many has been considered fully understood, yet another p-wave phase, perhaps yet to be experimentally established in any material, has recently been proposed in ^{3}He confined to strained silica aerogels [70].

---

[12] Similarly, different power laws appear when comparing e.g. the heat conductivity, ultrasound absorption, or the London penetration depth in the cases of point nodes and line nodes, respectively [58].

This newly suggested phase has $\boldsymbol{d}(\boldsymbol{k}) = k_z \hat{z}$, i.e. the gap has a horizontal line node at $k_z = 0$ – it corresponds precisely to the A_{2u} phase found in the prolate Fermi surface low-filling case on the lattice in the preceding subsection. Though merely an analogy to the lattice case, we leave this as an interesting remark that does not appear to have been discussed in the literature.

2.5 Numerical Results

Various studies have previously obtained the weak-coupling phase diagram of the 2D Hubbard model ($t_\perp = 0$ in our model) [15, 49, 51, 53]. Initial studies found a transition from $d_{x^2-y^2}$ to d_{xy} order as the filling was lowered, but this was later refined with the presence of an intermediate pocket of $\{p_x, p_y\}$ order close to $n \approx 0.55$ that had been overlooked [53]. The phase diagram has also been established with random phase approximation (RPA) methods [54, 55, 71]. In general, the RPA phase diagram contains a rich variety of orders, and greater regions of the phase diagram are dominated by d-wave superconductivity at finite U compared to the weak-coupling limit.

The 3D cubic lattice Hubbard model ($t_\perp = t_\parallel$ in our model) has also been studied numerically in the weak-coupling limit [15, 48]. In this case, the lattice symmetries of the octahedral point group O_h are restored, and it was established that a transition from $\{d_{x^2-y^2}, d_{2z^2-x^2-y^2}\}$ order (irrep E_g of O_h) to $\{p_x, p_y, p_z\}$ order (irrep T_{1u} of O_h) takes place when lowering the electron filling through $n \approx 0.32$.

Functional renormalisation-group studies in both the 2D [72, 73] and the 3D [74] Hubbard model have mostly focused on the regime close to half-filling. Here, these studies identify d-wave superconducting orders in agreement with the results discussed above, but depending on the details, antiferromagnetic instabilities tend to dominate at intermediate to strong coupling[13].

Taken together, the above lines, $t_\perp = 0$ and $t_\parallel = t_\perp$, constitute important consistency checks as we here aim to bridge the gap between these limits, as well as

---

[13] At half-filling in the strong-coupling limit, the Hubbard model maps onto the Heisenberg model with antiferromagnetic exchange coupling $J \propto t^2/|U|$ in any dimension [45, 75].

addressing the parameter region $t_\perp > t_\parallel$. In the subsections to follow we present numerical results for the weak-coupling ground state phase diagram, supplemented with examples of orders and pairing eigenvalues.

2.5.1 The Phase Diagram

Numerically, we discretise the Fermi surface, thereby reducing Eq. (2.22) to a regular matrix eigenvalue problem. We use 3000 to 4000 $\boldsymbol{k}$-points typically, and we vary $t_\perp$ (with $t_\parallel = 1.0$ fixed throughout) with a resolution of $\delta t_\perp = 0.1$ for a range of μ-values. Identifying the most negative eigenvalue of $\bar{\Gamma}_{\boldsymbol{k},\boldsymbol{k}'}$ at each parameter point results in the phase diagram shown in Fig. 2.9. In this figure examples of Fermi surfaces at six parameter points are indicated with gray surfaces. The van Hove lines from Eq. (2.32) are shown as black dashed lines, horizontal dotted lines mark cuts for the coupling strengths examined in Subsection 2.5.2, and labelled crosses show the positions of order parameters examined in Subsection 2.5.3.

In the parameter window $(\mu,\ t_\perp) \in [-5, 0] \times [0.0, 1.6]$ we find order parameters belonging to five distinct irreps of D_{4h}. We reproduce previously-established results in aforementioned limits. Specifically, as the chemical potential is lowered from half-filling in the 2D limit $t_\perp = 0$, we recover the transition from B_{1g} to E_u at $n = 0.57$ ($\mu = -1.15$) and the subsequent transition from E_u to B_{2g} at $n = 0.51$ ($\mu = -1.40$), cf. Ref. [53]. The transition from d-wave to p-wave order for $t_\perp = t_\parallel$ is also reproduced as the filling is lowered through $n = 0.32$ ($\mu = -2.46$), cf. Ref. [15].

At low filling, $n < 0.05$ ($\mu < -4.8$), the p-wave orders split, away from $t_\perp = t_\parallel$, in the fashion described analytically in Section 2.4, i.e. such that $\{p_x, p_y\}$ are favoured for $t_\perp < t_\parallel$ and p_z is favoured for $t_\perp > t_\parallel$. Notably, the splitting is opposite at intermediate electron fillings.

2.5.2 Coupling Strengths

In Fig. 2.10 the pairing eigenvalues along the parameter points of the horizontal dotted cuts of Fig. 2.9 are shown. To understand key trends of Fig. 2.10, recall that the Lifshitz transition (van Hove singularity) at $\mu = \mu_{xy} = -2t_\perp$ marks a change in the Fermi surface topology (enhancement of the density of states) due to

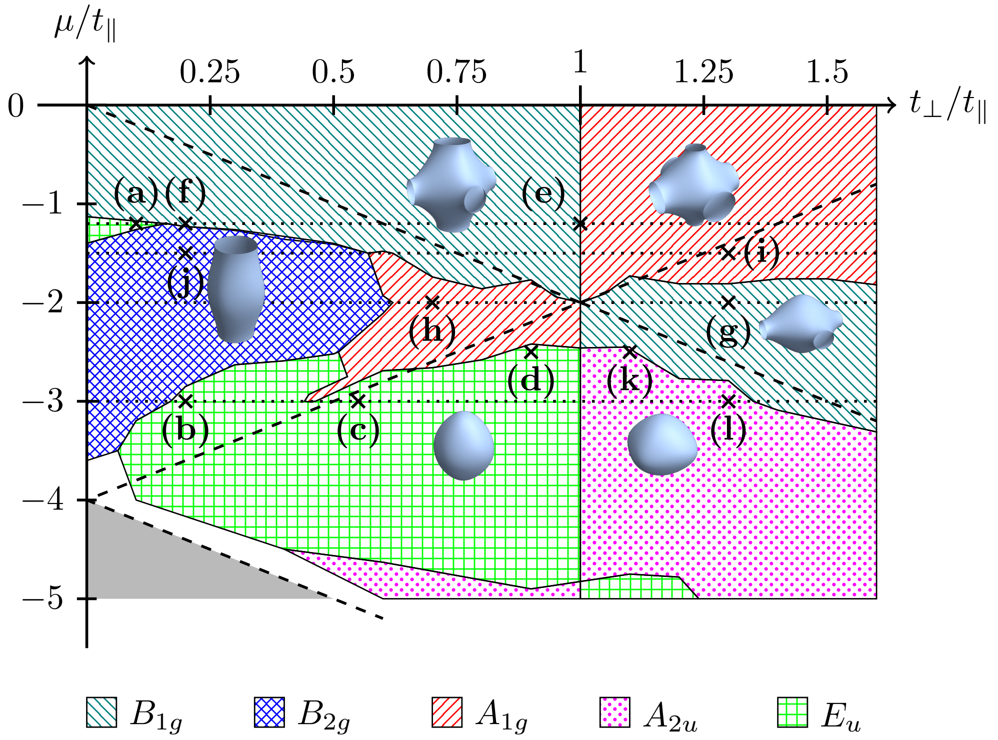

Figure 2.9: The ground state phase diagram of the model in Eq. (2.29) in the weak-coupling limit. The van Hove lines (dashed) of Eq. (2.32) separate four distinct Fermi surface shapes, as exemplified with gray surfaces. The gray shaded area has no Fermi surface, and in the white regions the Fermi surface is too small for the numerical scheme to be trusted. Pairing eigenvalues along the horizontal dotted lines are shown in Fig. 2.10. Order parameters at the positions of the labelled black crosses are examined in Fig. 2.11.

touching of the $k_x, k_y = \pm\pi$ BZ boundaries. Similarly, the Fermi surface touches the $k_z = \pm\pi$ zone boundary at $\mu = \mu_z = -4t_\parallel + 2t_\perp$. The condensation energy of an anisotropic superconductor is given by [69]

$$E_{\text{cond}} = -\frac{1}{2}\langle \rho(\boldsymbol{k})|\Delta(\boldsymbol{k})|^2\rangle_{S_F}, \tag{2.46}$$

where $\rho(\boldsymbol{k})$ is the density of states. Hence, a maximal gap in the regions where the density of states peaks, i.e. at a van Hove singularity, yields a gain in the condensation energy. This is notably the case for the $d_{x^2-y^2}$ order at μ_{xy} and for the $d_{2z^2-x^2-y^2}$ order at μ_z, respectively. Hence, these orders tend to be favoured in vicinity of the respective van Hove lines.

The interpretation is more complicated for the p-wave orders since there are qualitatively opposing mechanisms here. On the one hand, one could argue that

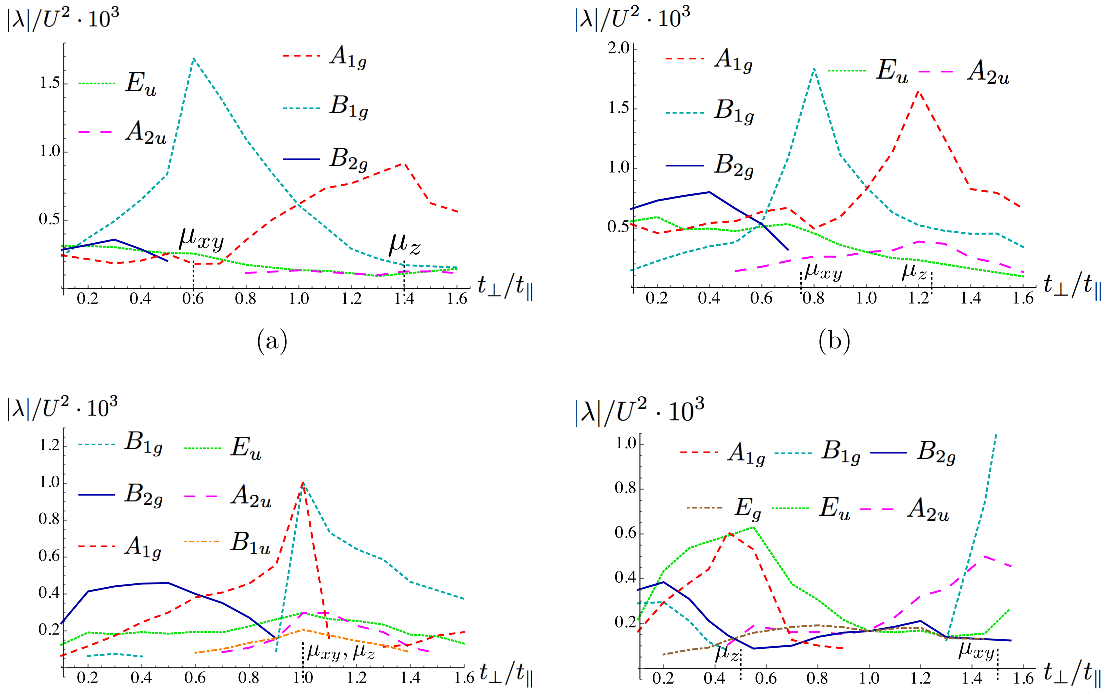

(a) (b)

(c) (d)

Figure 2.10: Leading (negative) pairing eigenvalues at the locations of the dotted lines in Fig. 2.9: $\mu = -1.2, -1.5, -2.0, -3.0$ in (a), (b), (c), (d), respectively. The short vertical dotted lines show the positions of the van Hove points, which tend to favour d-wave orders close to half-filling.

the p_z order would be favoured in vicinity to the μ_z line since this order has a maximal gap magnitude at the extremal values of k_z. On the other hand, a p_z order parameter, being of odd parity, would also have opposite signs at the $k_z = \pm\pi$ zone boundaries. These opposite signs typically leave little room for self-nesting, as per Eq. (2.44). Hence, a simple analytical prediction for regions of favoured p-wave order is not clear-cut and requires a numerical calculation.

2.5.3 Order Parameters

A selection of order parameters, at the locations indicated by labelled crosses in Fig. 2.9, are shown in Fig. 2.11. In Fig. 2.11 (a)–(e) two order parameters are degenerate (by symmetries of the lattice), and we consequentially show the magnitude of a complex combination of order parameters normalised by the maximal

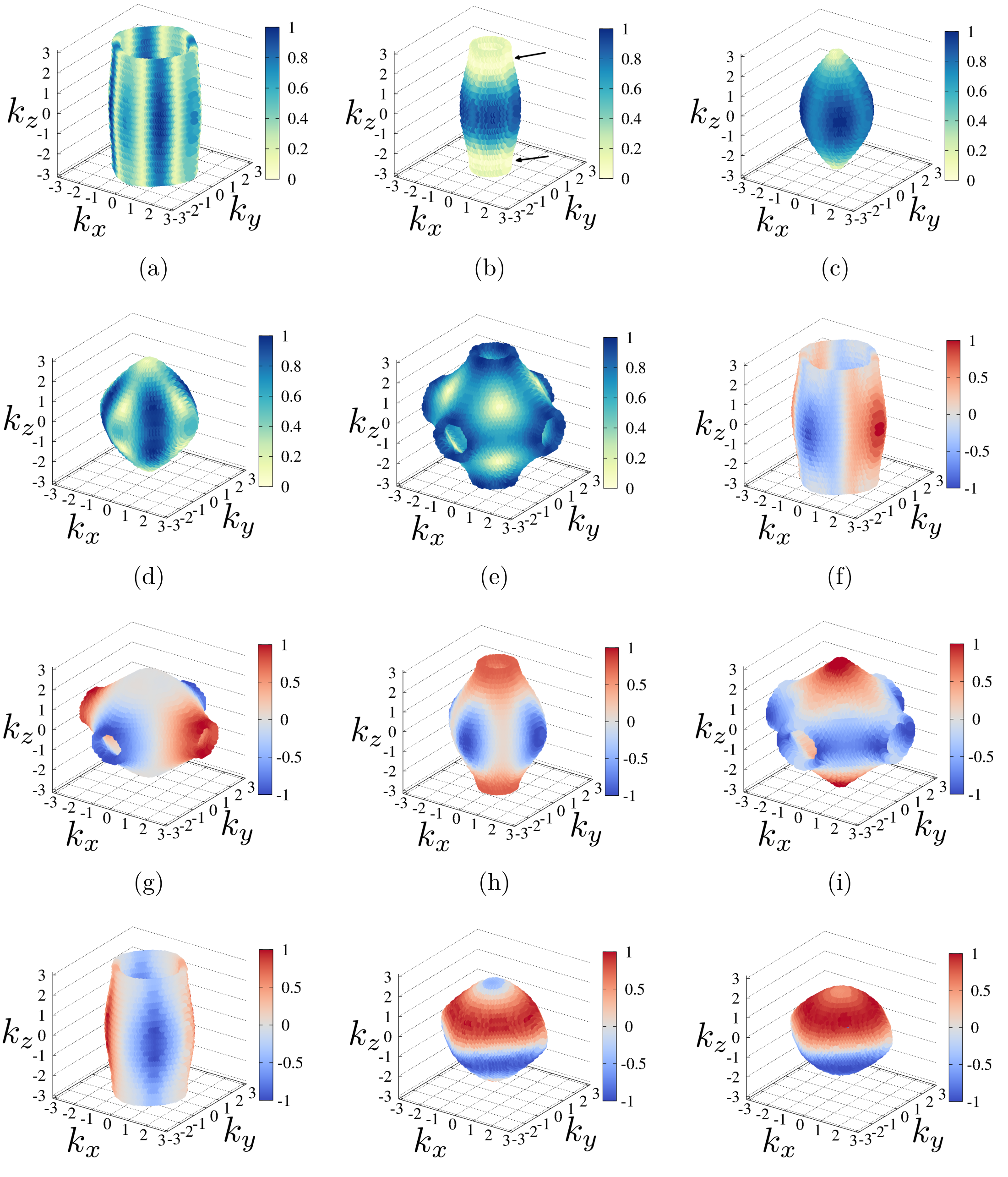

(a) (b) (c)

(d) (e) (f)

(g) (h) (i)

(j) (k) (l)

Figure 2.11: Order parameters on the Fermi surface at the parameter locations indicated with labelled crosses in Fig. 2.9 coloured by the (signed) order parameter magnitude. (a)–(e) Magnitude of complex order parameters $|\Delta(\boldsymbol{k})|$, and (f)–(l) real order parameters $\Delta(\boldsymbol{k})$, normalised by the maximal gap. Order parameters: (a)–(d) $p_x + ip_y$, (e) $d_{x^2-y^2} + id_{2z^2-x^2-y^2}$, (f)–(g) $d_{x^2-y^2}$, (h)–(i) $d_{2z^2-x^2-y^2}$, (j) d_{xy}, and (k)–(l) p_z. The arrows in (b) point at the horizontal line nodes.

gap[14], see also the discussion in Subsection 2.5.4 below. In Fig. 2.11 (f)–(l) we show various real order parameters normalised by the maximal gap.

Related to the discussion of Subsection 2.3.2, we find a rich variety of order parameters with contributions from lattice harmonics beyond the fundamental ones. For instance, the E_u order shown in Fig. 2.11 (a) has a substantial contribution from the next-to-fundamental harmonic $\sin(3k_x) + i\sin(3k_y)$. The resulting gap is highly anisotropic in $\boldsymbol{k}$ and has deep vertical minima, challenging the commonly accepted view that the E_u order is uniform on a cylindrical Fermi surface [79]. An even more striking example is the E_u order realised at lower filling, close to the 2D limit, shown in Fig. 2.11 (b). The slightly warped Fermi surface ($t_\perp = 0.2$) favours a higher lattice harmonic in k_z, which makes the complex $p_x + ip_y$ order acquire horizontal line nodes. Accidental horizontal line nodes are generally unexpected on a fairly 2D Fermi surface.

For closed Fermi surfaces the E_u orders display varied nodal structures, see Fig. 2.11 (c) and (d). Point nodes at the north and south pole, like in Fig. 2.11 (c), is the expectation for a “textbook” chiral p-wave order parameter on a spherical Fermi surface. The p-wave order in Fig. 2.11 (d), however, has a total of ten point nodes, eight of which are the consequences of circular-like, accidental nodes in the p_x and p_y components (similar to those seen in the p_z order of Fig. 2.11 (k)).

The d_{xy} and $d_{x^2-y^2}$ orders on cylinder-like Fermi surfaces, both with robust vertical line nodes, remain overall fairly 2D and dominated by the fundamental lattice harmonic, see e.g. Fig. 2.11 (f) and (j). The structure of $d_{2z^2-x^2-y^2}$ and the locations of its line nodes strongly change character depending on the Fermi surface topology, cf. Fig. 2.11 (h) and (i).

---

[14] Caveat: a two-component order parameter also allows for a nematic combination of orders, like $p_x \pm p_y$, which would break the point group symmetries. A nematic order parameter can be favoured over a chiral one, as determined by minimisation of the free energy [76]. However, no nematic order parameter was found to be favoured within our phase diagram. The compound $\mathrm{Cu}_x\mathrm{Bi}_2\mathrm{Se}_3$ is one of the few real examples of a putative nematic p-wave superconductor [77, 78].

2.5.4 Time-Reversal Symmetry Breaking

Certain regions of the phase diagram in Fig. 2.9 permit degeneracies of orders, as imposed by the lattice symmetries. Examples are shown in Fig. 2.11 (a)–(e). For instance, the p_x and p_y order parameters (irrep E_u of D_{4h}) are ensured degenerate by the tetragonal lattice. Another example is the parameter line $t_\perp = t_\parallel$ at which the octahedral point group symmetries are restored, thus enforcing degeneracy of e.g. the $d_{x^2-y^2}$ and $d_{2z^2-x^2-y^2}$ order parameters (irrep E_g of O_h). In such cases, complex combinations of order parameters are often favoured to minimise the free energy and yield an increase in the superconducting condensation energy, as per the argument given in Subsection 2.5.2 [11].

Chiral complex orders are time-reversal symmetry breaking (TRSB). Here, time-reversal symmetry is encoded by an antiunitary operator $\mathcal{T} = T\kappa$, where κ is the complex conjugation operator, and where T acts on momentum and spin states as $T\,|\psi_s(\boldsymbol{k})\rangle = s\,|\psi_{\bar{s}}(-\boldsymbol{k})\rangle$, with $\bar{s} = -s$. A phase is said to be time-reversal symmetry invariant (TRSI) if the single-particle (Bogoliubov–de Gennes) Hamiltonian $\mathcal{H}$ (as to be shown explicitly in Subsection 3.5.2) commutes with $\mathcal{T}$, $[\mathcal{T}, \mathcal{H}] = 0$ [65, 80]. Correspondingly, if the single-particle Hamiltonian does not commute with this operator, the phase is said to be TRSB.

For TRSB orders the *Chern number* provides a topological distinction of gapped phases in 2D [81]. We elaborate on the classification of topological phases of matter in Chapter 4. The Chern number may be defined for any 2D slice of the 3D Brillouin zone, so long as the magnitude of the gap is non-zero throughout the slice [64, 82]. We choose to define it in terms of k_z-slices of the Fermi sea, denoted by $S_F(k_z)$. The Chern number measures the winding of the complex order parameter phase:

$$C(k_z) = \frac{1}{2\pi} \oint_{S_F(k_z)} \mathrm{d}\boldsymbol{k} \cdot \nabla_{\boldsymbol{k}} \arg\left[\Delta(\boldsymbol{k})\right]. \tag{2.47}$$

As long as the gap does not close along the integrated path, the Chern number takes on integer values, $C(k_z) \in \mathbb{Z}$, and remains invariant under smooth deformations of the order parameter. As k_z varies, the Chern number can discontinuously jump up or down by one unit for each point node the integration path passes through.

For example, the $d_{x^2-y^2} + id_{2z^2-x^2-y^2}$ order shown in Fig. 2.11 (e) has $C = 0$ for all gapped k_z slices[15]. The eight point nodes of this order occur at $|k_x| = |k_y| = |k_z|$ as imposed by symmetry. This order is realised for $-2.46 < \mu < 0$ and $t_\perp = t_\parallel$. The odd-parity complex order parameters of Fig. 2.11 (a)–(d), on the contrary, display various gapped and nodal structures, which is *a priori* unexpected for such a simple single-band model. For instance, the fully gapped order parameter in Fig. 2.11 (a), found at $(\mu, t_\perp) = (-1.2, 0.10)$, has $C(k_z) = -3$. However, the order parameter in Fig. 2.11 (c), found at $(\mu, t_\perp) = (-3.0, 0.55)$, has $C(k_z) = +1$ for $|k_z| < k_{F,z}$ where $k_{F,z}$ is the z-component of the Fermi wave-vector at $k_x = k_y = 0$. The order parameter of Fig. 2.11 (d), found at $(\mu, t_\perp) = (-2.5, 0.90)$, is more exotic and has

$$C(k_z) = \begin{cases} +1 & \text{for } |k_z| < k'_z, \\ -3 & \text{for } k'_z < |k_z| < k_{F,z}, \end{cases} \tag{2.48}$$

where k'_z is the positive z-component of the eight point nodes closest to $k_z = 0$. This latter phase resembles a Weyl superconductor [83], in which bands touch in a linear fashion at Weyl points where the gap vanishes. Finally, a recent study showed that three odd-parity orders found and described here in principle can be distinguished by distinct low-temperature thermal Hall conductivity characteristics [64].

2.6 Range of Validity

The aim of this chapter was to create a simple and transparent platform in which unconventional superconductivity in three dimensions can be described and understood. The phase diagram of Fig. 2.9 might serve as a useful reference for future studies aiming to explore models that stabilise specific p- and d-wave orders. The weak-coupling approach, which dates back to seminal work by Kohn and Luttinger [14], asserts that a perturbative expansion in U/t is justified. As such, the results presented in this chapter are considered asymptotically exact as $U/t \to 0$. An advantage of this approach compared to e.g. advanced Monte Carlo methods [84] is that it is computationally feasible and exhibits appreciable numerical

---

[15] Looking ahead to Chapter 4 and Table 4.1, a $d + id$-wave superconductor formally belongs to class C in the classification of topological superconductors and insulators.

convergence. Secondly, the approximation is well-controlled, making the scheme transparent and allowing for calibration with analytical methods in the low-filling limit (as per Section 2.4) and with e.g. RPA studies in the weak-coupling limit (in which RPA reduces to the weak-coupling approach) for intermediate filling.

Clearly, the anisotropic Hubbard model of Eq. (2.29) is too simple to accurately describe real materials. In most cases, a realistic description of real compounds would require the inclusion of multiple tight-binding terms, multiple orbitals, spin-orbit coupling, and multi-orbital interactions that are rarely weak compared with the bandwidth. On the note of weak interactions, however, it is worth commenting that a recent numerical study suggests that the results obtained at weak coupling might serve as reasonable approximations well beyond the strict regime of $U \ll t$, at least in the 2D Hubbard model close to half-filling [85]. We elaborate on this point in the context of real materials in Subsection 3.4.3. Finally, it deserves being noted that another recent extensive numerical study suggests that the 2D Hubbard model may in fact not support a superconducting ground state in the intermediate U/t regime [86], supposedly the regime that applies to the cuprates.

Chapter 3

Superconductivity in Strontium Ruthenate

Contents

3.1 Introduction

Superconductivity in strontium ruthenate (Sr_2RuO_4, SRO) has accumulated an intriguing history with more than 26 years of theoretical and experimental research. To understand why this particular material merits a continued interest after so many years, with many hundreds of scientific papers published on the topic, it is necessary to review the historical and experimental situation. Since SRO has been subject to an extensive number of experimental and theoretical studies, we can only aim at reviewing a limited subset of the literature[1]. We open this chapter with a

---

[1] Elaborate reviews, some of which in light of recent experimental progress [19] must now be considered out of date, are given in Refs. [79, 87–90].

modest historical and experimental overview of superconductivity in SRO. Towards the end of the introduction we outline the remainder of this chapter.

It should be noted that the experimental front for superconductivity in SRO has been moving rapidly forward recently. To illustrate this, from the appearance of the new nuclear magnetic resonance (NMR) results [19] (which will be described below) until February 2020, on the order of ten experimental preprints have appeared on `arXiv.org`. Our intention with this section is to provide an overview of the historical situation, not to review the ongoing and still evolving experimental effort. Instead, we will discuss some of the most recent developments and interpret our results in light of them in Sections 3.5 and 3.6.

3.1.1 Historical and Experimental Overview

In the early history of high-temperature (high-T_c) superconductivity, a common feature of all high-T_c compounds was that they had copper and a layered perovskite crystal structure. In 1994 superconductivity in SRO – a compound with the same layered structure but without copper – was discovered below the modest critical temperature $T_c \approx 1.5$ K [17]. The perovskite crystal structure, defining a tetragonal lattice, is shown in Fig. 3.1.

The ruthenium t_{2g} electrons, as defined by the electronic orbitals $4d_{xz}$, $4d_{yz}$, and $4d_{xy}$, are believed to be dominantly responsible for the superconductivity in SRO. In reciprocal space these three orbitals hybridise and form three semi-cylindrical Fermi surface sheets, denoted by α, β, and γ. As SRO makes crystals of excellent purity, its Fermi surface sheets have been successfully measured with at least two independent probes, which show excellent agreement: angle-resolved photoemission spectroscopy (ARPES) [92, 93], and de Haas–van Alphen quantum oscillations [87, 94]. In Fig. 3.2 we show a two-dimensional slice of the approximately cylindrical Fermi surface sheets as measured with recent high-resolution ARPES [93].

In the years following the discovery a range of experiments provided strong evidence that superconductivity in SRO is unconventional. Two probes qualitatively

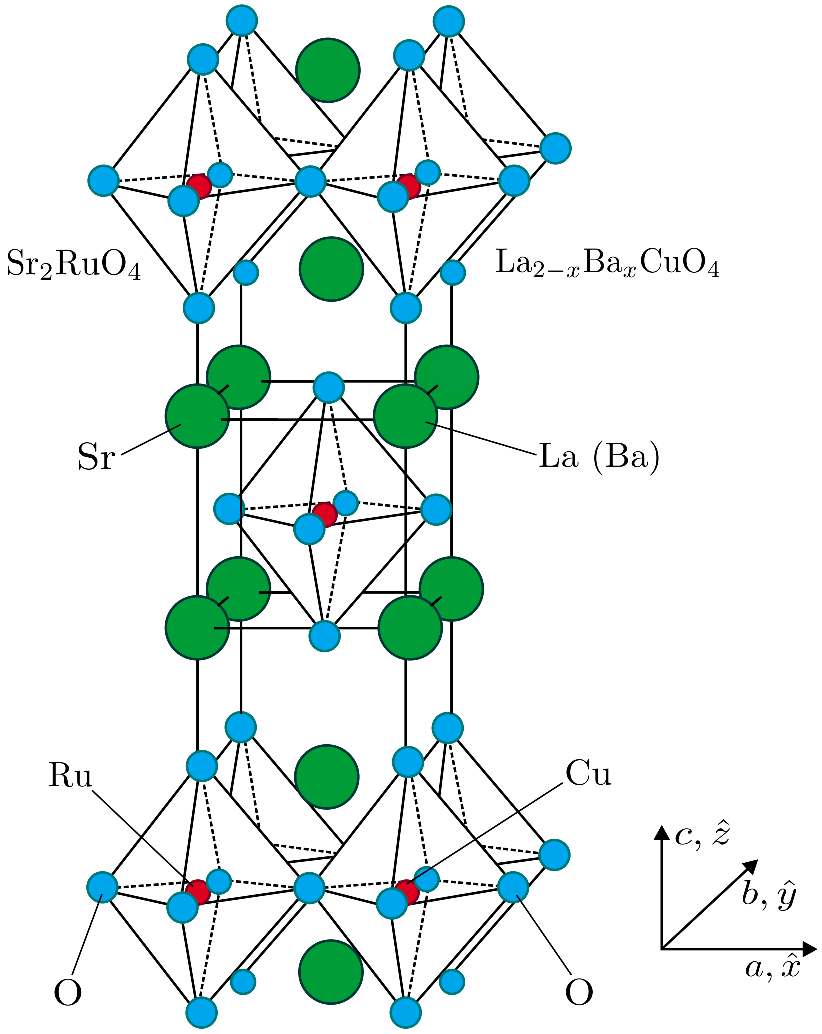

Figure 3.1: Crystal structure of the perovskite Sr_2RuO_4 (SRO) and the high-T_c family $La_{2-x}Ba_xCuO_4$ [91]. For SRO the lattice constants are $a = b = 3.86$ Å and $c = 12.72$ Å. Adapted from [Y. Maeno, T. M. Rice, and M. Sigrist, Physics Today **54**, 1, 42 (2001)], with the permission of the American Institute of Physics.

imply time-reversal symmetry breaking (TRSB) in the superconducting phase[2]. Muon spin rotation (μSR) – a bulk probe where the subsequent decay of polarised muons incident on the sample are correlated with the local magnetic surroundings – hinted at spontaneous magnetic fields generated by chiral currents [96]. The same conclusion was later also reached with the magneto-optic polar Kerr effect [97]. The latter is a surface probe where linearly polarised light incident on the sample surface is reflected as elliptically polarised light after interacting with a magnetic

---

[2] New experimental results indicate that the critical temperature is higher than the temperature where TRSB sets in [95]. This is discussed in Section 3.6.

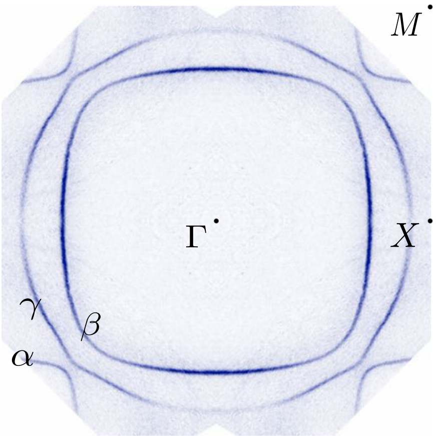

Figure 3.2: Fermi surface sheets α, β, and γ of strontium ruthenate from high-resolution ARPES measurements. The Brillouin zone labels are explained in Fig. 3.5. Figure adapted from Ref. [93]: [A. Tamai et al., Phys. Rev. X **9**, 021048 (2019)] under the terms of the Creative Commmons Attribution 4.0 International license.

environment. If the apparent observations of TRSB indeed are associated with superconductivity in SRO, we emphasise that this is a highly restrictive criterion in terms of the possible order parameters on a tetragonal lattice. From Table 2.1 it is clear that only the two-dimensional representations E_g and E_u offer robust ways of achieving a chiral order parameter. By "robust" we mean disregarding the option of coupling order parameters from different irreducible representations (irreps) – an option we return to in Section 3.6.

For a single-band superconductor with no spin-orbit coupling (SOC), the magnetic response under the application of a small magnetic field (compared with the upper critical field H_{c2}) yields a characteristic zero-temperature value (when normalised appropriately) depending on the order parameter [18, 69], see Fig. 3.12. In SRO NMR Knight shift measurements initially showed no drop in the spin susceptibility below the critical temperature for a magnetic field pointing in the basal plane [98, 99]. In the absence of SOC, such an observation can only be reconciled with a $\boldsymbol{d}$-vector pointing in the $\hat{z}$-direction in the notation of Table 2.1. Hence, these experiments were interpreted as strong evidence of the realisation of a chiral p-wave order parameter (irrep E_u) in SRO. Furthermore, the bulk of the experimental and theoretical studies the years to follow kept a perhaps biased focus on observations supporting the chiral p-wave hypothesis.

If the chiral p-wave hypothesis was found to be true, it would make SRO one of the first chiral p-wave superconductors discovered and a solid-state analogue of superfluid ^{3}He [8, 18]. A 2D chiral p-wave superconductor would also be topological (which is described in Chapter 4). The most remarkable application of a 2D topological superconductor is that it would (in principle) give a platform for topological quantum computation with non-Abelian anyons [21, 23, 28]. Despite strong initial indications of a chiral p-wave phase being realized in SRO, an accumulated series of experiments have raised substantial objections to this interpretation, some of which we highlight below.

In a conventional (BCS) superconductor the density of states drops to zero for energies below the superconducting gap Δ_0. In turn, this yields a specific heat exponentially suppressed below the gap, $C(T) \propto T^{-3/2} \exp[-\Delta_0/(k_B T)]$ [58, 69]. Unconventional superconductors are, on the other hand, characterised by low-lying quasiparticles and nodes in the gap, as explained in Chapter 2. Thus, unconventional superconductors obey instead power law behaviour at low temperature: $C(T) \propto T^n$ with $n = 2$ $(n = 3)$ when the gap has line (point) nodes. Specific heat experiments conducted on SRO result in a $C(T)/T \propto T$ dependence down to temperatures in the mK range [100–102], see Fig. 3.3. The linear tendency implies very deep line-like minima or true line nodes in the gap. Similar conclusions are inferred from thermal conductivity measurements [103, 104], and from acoustic attenuation experiments [105]. Since a "textbook" $p_x + ip_y$ order parameter on a cylindrical Fermi surface would be fully gapped [79], the above experiments lack a crisp explanation in the chiral p-wave scenario.

When uniform strain is applied to a tetragonal crystal in either of the in-plane directions ($\hat{x}$ or $\hat{y}$) the crystal symmetries are broken and the point group symmetries reduced, $D_{4h} \to D_{2h}$. One consequence of this is the lifting of the degeneracy between p_x and p_y orders. At mean-field level in the absence of disorder this degeneracy lifting was predicted to give a T_c-cusp at zero strain (when T_c is plotted as a function of strain) for a two-component order parameter like $p_x \pm ip_y$ [11, 106]. In SRO no cusp is observed [107, 108]. When strained to the vicinity of a van Hove singularity

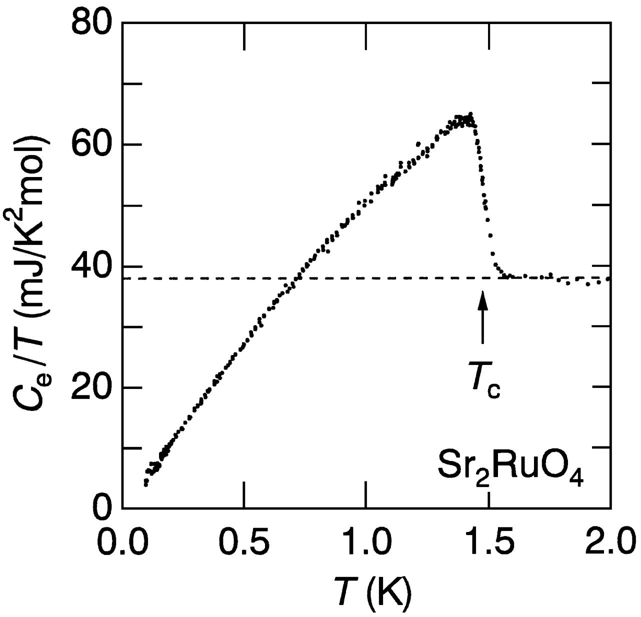

Figure 3.3: Experimentally measured electronic specific heat per temperature, C_e/T, for Sr_2RuO_4. The linear tendency down to mK temperatures implies line-like (near-)nodes in the gap. Figure from Ref. [100], [S. NishiZaki, Y. Maeno, Z. Mao, J. Phys. Soc. Jpn. **69**, 572–578 (2000)], (c) (2000) The Physical Society of Japan.

for the γ band, the behaviour of H_{c2} as a function of strain is reminiscent of that of a d-wave superconductor [108]. A hypothesised solution to this apparent contradiction is the transition between, say, a chiral p-wave to a d-wave order parameter at some intermediate strain value. However, no clear indications of this possibility are revealed when the specific heat is probed continuously under strain[3] [109].

To add to the accumulated set of conflicting evidence, the in-plane NMR Knight shift experiment was recently repeated [19], yielding results that strongly conflict with the original ones [98]. Now, a substantial drop in the spin susceptibility is measured[4] at temperatures of $T \approx 20$ mK. In the absence of SOC this observation would rule out all vectorial order parameters with $\boldsymbol{d} \parallel \hat{z}$. We emphasise, however, that SOC is crucial for the quantitative interpretation of both the NMR results and the normal-state properties of SRO [93, 110, 111]. In a multi-orbital system with strong SOC the analysis for the spin susceptibility is more involved than for

---

[3] This situation should be contrasted with the successful observation of an order parameter transition, such as for UPt_3 [12].

[4] The discrepancy with the original results was explained by heating of the sample when using too high NMR pulse frequencies.

that of a single-band model, as we explain in Subsections 3.5.2 and 3.5.3. The new NMR results have also reassuringly been reproduced by the Ishida group reporting the initial result [20]. When interpreted in isolation, the new NMR results appear compatible with several even-parity order parameters and possibly the helical order parameters, but not a chiral p-wave order parameter.

3.1.2 Motivation and Outline

Arguably, strontium ruthenate has played an important role in the development of our understanding of unconventional superconductivity, independently of which order parameter turns out to be describing the superconducting state of SRO. In many ways, SRO is an ideal testbed for theory to work towards an enhanced understanding of the mechanism(s) of unconventional superconductivity. For $T_c < T < T_{\mathrm{FL}} \approx 25$ K the material has a well-defined Fermi liquid behaviour [87, 112], it makes crystals almost free from disorder [113], and it has a low T_c encouraging the weak-coupling approach. Moreover, there are hundreds of high-quality experimental results spanning wide-ranging probes to compare with.

With exclusive regard to the NMR experiments, the history of SRO has, as explained above, undergone a peculiar turn. Until 2019 the chiral p-wave order parameter appeared to be the only one consistent with the NMR experiment [98]. With the new results [19, 20] the chiral p-wave order parameter appears to be the only option clearly inconsistent with the experiment. To this end, the debate concerning the superconducting order of SRO has largely reopened. There is an explicit call for theory to compare possible order parameters in an unbiased fashion (cf. the irreps listed in Table 2.1). Microscopically calculated order parameters should crucially be quantitatively compared to experimental data, especially the new NMR data, to validate or invalidate the theory.

Most previous microscopic three-band studies of SRO have made use of 2D models[5] [116–118]. This is a reasonable assumption from the perspective of the semi-2D Fermi surface sheets, as detected with quantum oscillations [87, 94]. One

---

[5] Recently, more 3D studies have started to appear, one of which we will comment on in due course [114, 115].

might thus expect the inter-layer hopping to be correspondingly weak. To some extent the semi-2D Fermi surface is deceptive. The band structure reveals a non-negligible k_z-dispersion, at least for the β and γ bands [90, 110, 111]. Moreover, owing to the strong SOC – which is expected to play an important role in SRO [93] – spin correlations and the orbital content were shown to exhibit a substantial k_z-dependence [110, 111]. Furthermore, for an unbiased comparison of all ten irreps that the order parameter can belong to, a 3D model is indeed required. A 3D study can also address the prospects of horizontal line nodes, which in the present case might be unexpected but nevertheless has been proposed repeatedly in the literature over the past two decades [19, 38, 79, 90, 104, 119–122]. This is particularly important in light of the recent experimental progress.

In the remainder of this chapter we present one of the first microscopic calculations of the superconducting order parameter in SRO derived from a 3D three-band model including SOC. We construct an effective tight-binding model by fitting the band structure of a three-band model to the relevant three bands of an existing 17-band model derived from spin-resolved ARPES data [111]. On-site Hubbard–Kanamori type interaction terms are added [123], and the generalised gap equation is solved numerically within the multiband weak-coupling framework. As a function of the (unknown) effective interaction parameter J/U, where J (U) is the spin-spin (density-density) on-site Hubbard strength, we identify two phases: helical p-wave triplet and $d_{x^2-y^2}$-wave singlet for J/U smaller and larger than $J/U \approx 0.15$, respectively.

We further present a detailed comparison of both orders with two key experimental probes: the specific heat and the spin susceptibility as probed via NMR Knight shift. Both orders are roughly found compatible with current data, and we show that they can be distinguished by a future NMR experiment where the magnetic field points out of the basal plane. The chiral p-wave order, numerically competitive with helical order, is found to sharply conflict with the recent NMR experiments [19, 20]. This is a surprising result since chiral p-wave has been the leading order parameter candidate in SRO for more than two decades. We also clarify that horizontal line nodes in the gap, which have been proposed in various previous works, appear unfavoured; the highest-T_c order parameters found have all vertical (near-)nodes. When taking into account recent experimental progress, we conclude the chapter with a discussion of outstanding aspects, primarily the observation of TRSB. Possible outcomes to the long-standing SRO puzzle are discussed in the Subsection 3.6.2.

3.2 A Tight-Binding Model in Three Dimensions

We start by constructing a tight-binding model for the normal state of SRO valid near the Fermi energy. The essential ingredients for this description are the three electronic Ru t_{2g} orbitals $4d_{xz}$, $4d_{yz}$, and $4d_{xy}$. Aided by the spin-orbit coupling [110, 111], hybridisation of these orbitals is responsible for the formation of the three bands that cross the Fermi energy, which are commonly denoted by α, β, and γ [92, 93], see Fig. 3.5 (cf. Fig. 3.2).

3.2.1 A Tight-Binding Ansatz

The starting point is a generic three-orbital tight-binding model:

$$H_0 = \sum_{\boldsymbol{k},s} \boldsymbol{\psi}_s^\dagger(\boldsymbol{k}) \mathcal{H}_s(\boldsymbol{k}) \boldsymbol{\psi}_s(\boldsymbol{k}). \tag{3.1}$$

Here, $\boldsymbol{\psi}_s(\boldsymbol{k}) = [c_{As}(\boldsymbol{k}),\ c_{Bs}(\boldsymbol{k}),\ c_{C\bar{s}}(\boldsymbol{k})]^T$, where $c_{as}(\boldsymbol{k})$ is the annihilation operator of an electron of crystal momentum $\boldsymbol{k}$ and spin s (with $\bar{s} = -s$) on Ru orbital $4d_a$, when using the shorthand orbital notation $A = xz$, $B = yz$, and $C = xy$, as visualised in Fig. 3.4. In the above notation one should understand $s = +1$

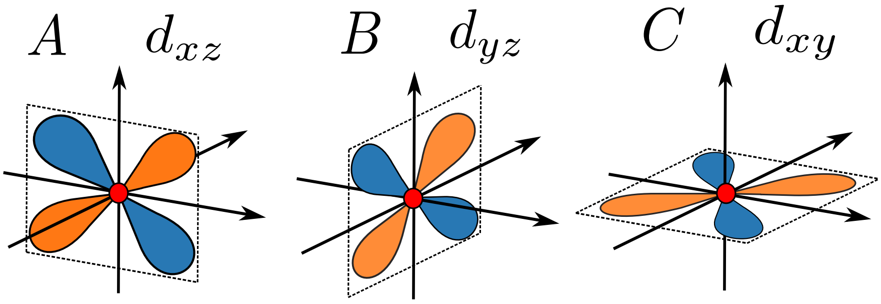

Figure 3.4: The three t_{2g} Ru ($4d$) orbitals included in the effective model, relevant to the Fermi surface physics of Sr_2RuO_4.

as spin $\uparrow$, and $s = -1$ as spin $\downarrow$ when the spins are quantised in the $\hat{z}$-direction. The matrix $\mathcal{H}_s$ has the structure

$$\mathcal{H}_s(\boldsymbol{k}) = \begin{pmatrix} \varepsilon_{AA}(\boldsymbol{k}) & \varepsilon_{AB}(\boldsymbol{k}) - is\eta & \varepsilon_{AC}(\boldsymbol{k}) + i\eta \\ \varepsilon_{BA}(\boldsymbol{k}) + is\eta & \varepsilon_{BB}(\boldsymbol{k}) & \varepsilon_{BC}(\boldsymbol{k}) - s\eta \\ \varepsilon_{CA}(\boldsymbol{k}) - i\eta & \varepsilon_{CB}(\boldsymbol{k}) - s\eta & \varepsilon_{CC}(\boldsymbol{k}) \end{pmatrix}, \tag{3.2}$$

where η parametrises the spin-orbit coupling[6]. For the orbital energies $\varepsilon_{ab}(\boldsymbol{k})$ we account for both intra- and inter-orbital hopping, both in-plane and out-of-plane, consistent with the crystal symmetries. As ansätze for ε_{AA} and ε_{BB} we retain hopping terms up to three sites apart in the basal plane and leading order terms out of the basal plane. Specifically, we let

$$\begin{aligned} \varepsilon_{AA}(k_x, k_y, k_z) &= \varepsilon_{1\mathrm{D}}(k_x, k_y, k_z), \\ \varepsilon_{BB}(k_x, k_y, k_z) &= \varepsilon_{1\mathrm{D}}(k_y, k_x, k_z), \end{aligned} \tag{3.3}$$

where

$$\begin{aligned} \varepsilon_{1\mathrm{D}}(k_\parallel, k_\perp, k_z) = &- 2t_1 \cos\big(k_\parallel\big) - 2t_2 \cos(k_\perp) - 2t_3 \cos\big(2k_\parallel\big) \\ &- 4t_4 \cos\big(k_\parallel\big) \cos(k_\perp) - 4t_5 \cos\big(2k_\parallel\big) \cos(k_\perp) \\ &- 2t_6 \cos\big(3k_\parallel\big) - 2t_7 \cos\left(2t_\perp\right) \\ &- 2t_8 \cos\big(k_\parallel/2\big) \cos(k_\perp/2) \cos(k_z/2) - \mu_{1\mathrm{D}}. \end{aligned} \tag{3.4}$$

For the semi-2D orbital $C = xy$ we treat hopping in the $\hat{x}$ and $\hat{y}$ directions on equal footing:

$$\begin{aligned} \varepsilon_{CC}(\boldsymbol{k}) = &- 2\bar{t}_1 \left[\cos(k_x) + \cos(k_y)\right] - 4\bar{t}_2 \cos(k_x) \cos(k_y) \\ &- 2\bar{t}_3 \left[\cos(2k_x) + \cos(2k_y)\right] - 4\bar{t}_4 \left[\cos(2k_x) \cos(k_y) + \cos(2k_y) \cos(k_x)\right] \\ &- 2\bar{t}_5 \cos(k_z/2) \cos(k_x/2) \cos(k_y/2) - \mu_{2\mathrm{D}}. \end{aligned} \tag{3.5}$$

Finally, we include leading inter-orbital terms:

$$\varepsilon_{AB}(\boldsymbol{k}) = -4\tilde{t}_1 \sin(k_x) \sin(k_y) - 4\tilde{t}_2 \sin(k_x/2) \sin(k_y/2) \cos(k_z/2), \tag{3.6}$$

$$\varepsilon_{AC}(\boldsymbol{k}) = -4\tilde{t}_3 \sin(k_z/2) \cos(k_x/2) \sin(k_y/2), \tag{3.7}$$

$$\varepsilon_{BC}(\boldsymbol{k}) = -4\tilde{t}_3 \sin(k_z/2) \sin(k_x/2) \cos(k_y/2). \tag{3.8}$$

---

[6] Technically, the η-dependence in Eq. (3.2) arises from $H_{\mathrm{SOC}} = 2\eta P_{t_{2g}} \boldsymbol{L} \cdot \boldsymbol{S} P_{t_{2g}}$, where $P_{t_{2g}}$ is a projector onto the t_{2g} triplet shown in Fig. 3.4, and where $\boldsymbol{L}$ ($\boldsymbol{S}$) is the angular momentum (spin) operator [124, 125].

All terms included above are consistent with the symmetries of the tetragonal lattice [126], and the model is considered over the Brillouin zone defined as BZ $= [-\pi,\pi]^2 \times [-2\pi, 2\pi]$. The elongated k_z interval is due to the body-centred tetragonal Brillouin zone which exhibits a shifted stacking (due to the shifted $\mathrm{RuO_2}$ layers) [87]. Our definition above is a choice to ensure that all distinct $\boldsymbol{k}$-points are represented. We have also defined dimensionless momenta: k_x and k_y are measured in units of the in-plane lattice constant a, and k_z is measured in units of the out-of-plane lattice constant c, see Fig. 3.1.

3.2.2 Bands and Pseudo-Spins

The hopping Hamiltonian $\mathcal{H}_s$ is described by orbital (a) and spin (s) degrees of freedom, and it includes SOC as parametrised by η. When diagonalising the matrix $\mathcal{H}_{s=+1}(\boldsymbol{k}) \oplus \mathcal{H}_{s=-1}(\boldsymbol{k})$ the eigenvalues are labelled by band $\mu = \alpha, \beta, \gamma$ and pseudo-spin $\sigma = \pm$ indices:

$$H_0 = \sum_{\boldsymbol{k}} \sum_{\mu,\sigma} \xi_{\mu\sigma}(\boldsymbol{k}) c^\dagger_{\mu\sigma}(\boldsymbol{k}) c_{\mu\sigma}(\boldsymbol{k}). \tag{3.9}$$

The eigenvectors define a unitary transformation between the bases of orbital and spin, and band and pseudo-spin:

$$c^\dagger_{\mu\sigma}(\boldsymbol{k}) = \sum_{a,s} u^{\mu\sigma}_{as}(\boldsymbol{k}) c^\dagger_{as}(\boldsymbol{k}), \quad \text{and} \quad c^\dagger_{as}(\boldsymbol{k}) = \sum_{\mu,\sigma} \left[u^{\mu\sigma}_{as}(\boldsymbol{k})\right]^* c^\dagger_{\mu\sigma}(\boldsymbol{k}). \tag{3.10}$$

The eigenvectors of the matrices $\mathcal{H}_{s=\pm1}$ are related by a combined time-reversal and inversion symmetry[7], and they give rise to a two-fold Kramers degeneracy of the three eigenvalues $\xi_{\mu\sigma=\pm}(\boldsymbol{k}) \equiv \xi_\mu(\boldsymbol{k})$. A convenient choice is to assign $\sigma = +$ to the block $\mathcal{H}_{s=+1}$. If one in addition imposes a $\boldsymbol{k}$-dependent gauge choice for the eigenvectors, the eigenvectors corresponding to pseudo-spin value $\sigma = -$ are uniquely fixed. Such a gauge choice is described in Subsection 3.3.2. The three Fermi surface sheets are defined by $\xi_\mu(\boldsymbol{k}) = 0$, and they are shown in Fig. 3.6 after fixing the tight-binding parameters as described in the following subsection.

---

[7] Inversion symmetry sends $\boldsymbol{k} \to -\boldsymbol{k}$, and time-reversal symmetry involves complex conjugation, sending $\boldsymbol{k} \to -\boldsymbol{k}$, and flipping spins (see Subsection 2.5.4).

3.2.3 Tight-Binding Parameters

The model proposed in Subsection 3.2.1 contains 19 undetermined parameters,

$$\{t\} \equiv \Big\{\{t_i\}_{i=1}^{8}, \{\bar{t}_i\}_{i=1}^{5}, \{\tilde{t}_i\}_{i=1}^{3}, \mu_{\mathrm{1D}}, \mu_{\mathrm{2D}}, \eta\Big\}. \tag{3.11}$$

In this section these parameters are determined by fitting the band structure, via Monte Carlo (MC) sampling, to the three relevant bands of the 17-band model of Ref. [111]. The latter model is based on fitting an extensive tight-binding ansatz to the band structure inferred from spin-resolved ARPES data. To facilitate a combined band structure and orbital content fit, we define a cost function [127]:

$$\begin{aligned} D(\{t\}) \equiv & \sum_{\mu} \sum_{\boldsymbol{k}} w_{\boldsymbol{k}} \big(\xi_{\mu}(\boldsymbol{k}, \{t\}) - \tilde{\xi}_{\mu}(\boldsymbol{k})\big)^2 \\ & + \sum_{\mu} \sum_{\boldsymbol{q} \in S_{\mu}} \bar{w}_{\boldsymbol{q}} \Big(|u_{C\downarrow}^{\mu +}(\boldsymbol{q}, \{t\})|^2 - |\tilde{u}_{C\downarrow}^{\mu +}(\boldsymbol{q})|^2 \Big)^2 . \end{aligned} \tag{3.12}$$

Here, quantities with a tilde refer to those obtained from the model of Ref. [111], and bare quantities to those as obtained with our effective model. The symbols $w_{\boldsymbol{k}}$ and $\bar{w}_{\boldsymbol{q}}$ are chosen energy and orbital weights, respectively. First, we fix $w_{\boldsymbol{k}} = 1.0\ \mathrm{eV}^{-1/2}$ and $\bar{w}_{\boldsymbol{q}} = 0$ for 44 fitting points in a primitive tetragonal unit cell, as shown with crosses in Fig. 3.5 (b). The weights $w_{\boldsymbol{k}}$ are increased by a factor of four for 16 of the $\boldsymbol{k}$-points closest to the Fermi energy and for the high-symmetry points with labels in the inset of Fig. 3.5 (b). Sets $\{t\}$ are drawn from uniform intervals for each MC cycle. A set $\{t\}$ is kept as the new optimal set with probability $\exp\big(-D(\{t\})^{1/2}/T\big)$ if it reduces the value of $D(\{t\})$ compared to the previous optimal set. Here, T is a parameter that we gradually reduce in hope of converging to the global minimum of D. After millions of MC cycles with consecutive narrowing of the parameter ranges for $\{t\}$, we end up with a preliminary band fit.

Secondly, we turn on the orbital fitting weights $\bar{w}_{\boldsymbol{q}} = 2.0$ for all bands, where the $\boldsymbol{q}$'s are momenta on the Fermi surface picked at the three in-plane directions $\theta = 0,\ \pi/6,\ \pi/4$ (θ is defined as the in-plane polar angle relative to the $\hat{x}$-axis) for the three k_z-slices $k_z = 0,\ \pi,\ 2\pi$. We repeat the procedure outlined above to refine the fit and ensure reproduction of the orbital content of the bands compared with Ref. [111].

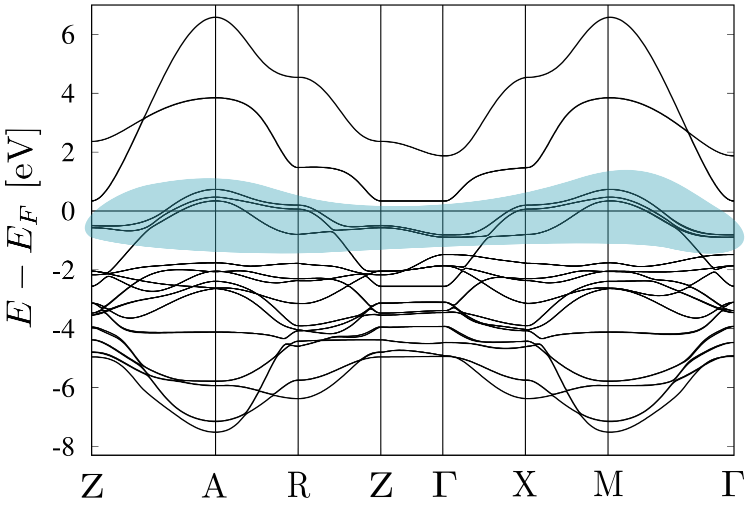

(a)

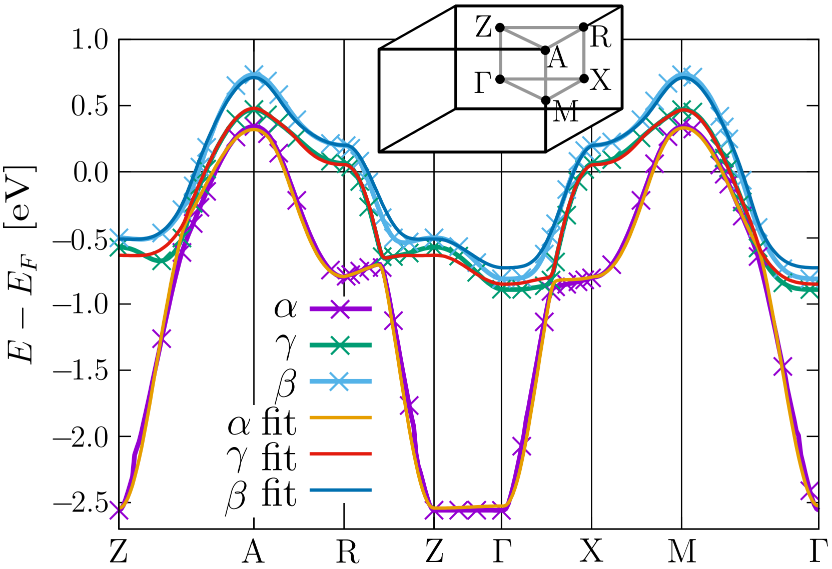

(b)

Figure 3.5: (a) Reproduced band structure of the 17-band tight-binding model proposed in Ref. [111], [C. N. Veenstra et al., Phys. Rev. Lett., **112**, 127002 (2014)], based on spin-resolved ARPES data. The three bands crossing the Fermi energy are highlighted in blue. (b) Optimal band structure fit, at the fitting points marked with crosses, of our effective three-band model to the relevant bands of the 17-band model. The inset of (b) shows the primitive tetragonal unit cell.

The optimal tight-binding parameters found in this way are listed in Tables 3.1, 3.2, and 3.3. Since the threshold for inclusion of terms in the model in Ref. [111] is $\mathcal{O}(10\text{ meV})$, we can only hope to accurately describe tight-binding terms larger than this threshold. Hence, the parameters t_5, t_6, t_7, $\bar{t}_5$, $\tilde{t}_1$, and $\tilde{t}_3$ can and should be discarded to increase numerical efficiency. We note that, surprisingly, the inter-layer term t_8 comes out as the next-to-largest hopping term in Table 3.1, giving strong hints of the deceptive perception that the inter-layer physics of SRO can safely be ignored.

Table 3.1: Tight-binding parameters for Eq. (3.4) obtained with Monte Carlo fitting.

Parameter	t_1	t_2	t_3	t_4	t_5	t_6	t_7	t_8
Value [meV]	257.8	27.8	−35.5	−22.4	−4.7	−2.4	3.2	54.5

Table 3.2: Tight-binding parameters for Eq. (3.5) obtained with Monte Carlo fitting.

Parameter	$\bar{t}_1$	$\bar{t}_2$	$\bar{t}_3$	$\bar{t}_4$	$\bar{t}_5$
Value [meV]	356.8	126.3	17.0	22.3	−4.1

Table 3.3: Tight-binding parameters for Eq. (3.2) obtained with Monte Carlo fitting.

Parameter	μ_{1D}	μ_{2D}	η	$\tilde{t}_1$	$\tilde{t}_2$	$\tilde{t}_3$
Value [meV]	286.9	351.9	59.2	2.0	−15.5	−5.4

The Fermi surface produced with the effective model, using the tight-binding parameters above, is shown in Fig. 3.6, where the bands are coloured by a measure of the orbital content. Note that the α band is dominated by the Ru orbitals $4d_{xz}$ and $4d_{yz}$. In contrast, bands β and γ exhibit strong mixing between the aforementioned orbitals and $4d_{xy}$. Moreover, the k_z-dependence of the orbital mixing is non-negligible on the β band. To provide a quantitative comparison of the Fermi surface produced with our effective model to the model of Ref. [111], Fermi surface k_z

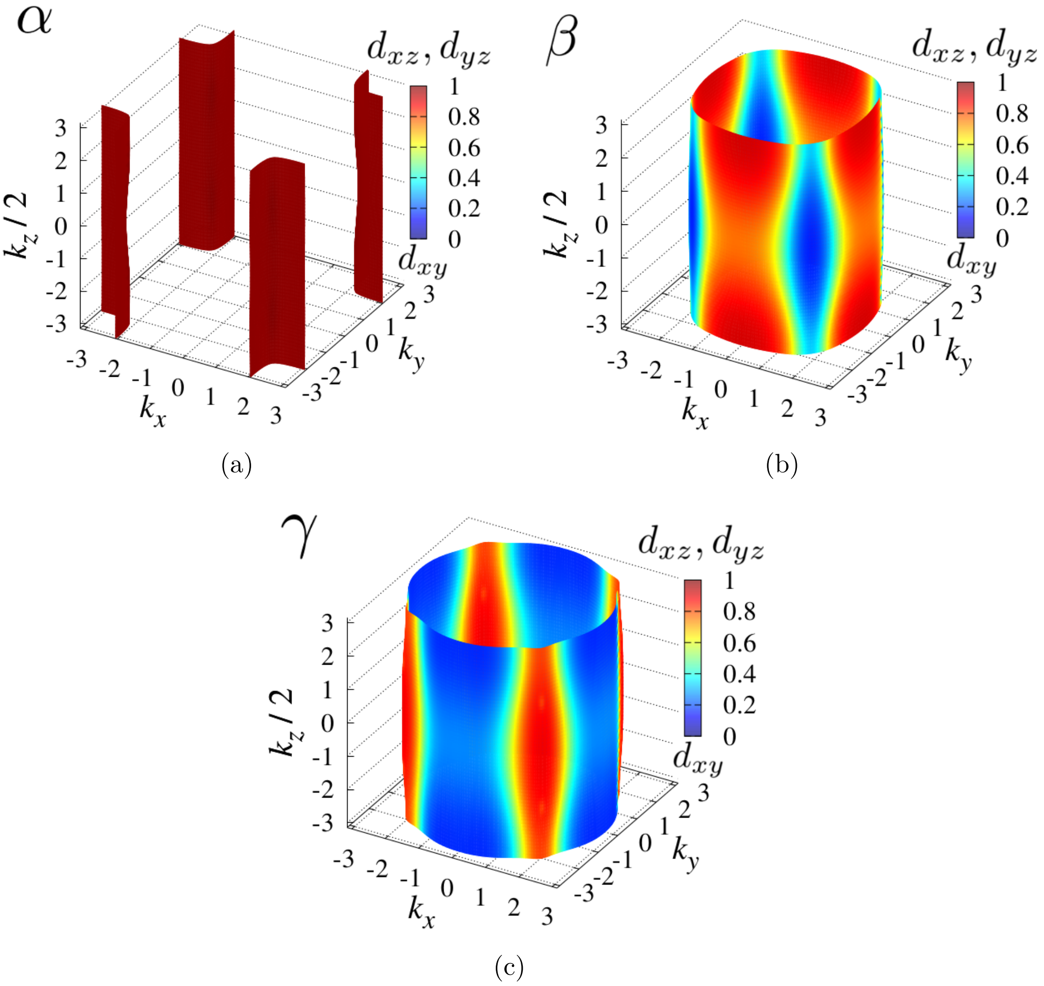

(a)

(b)

(c)

Figure 3.6: Three-dimensional Fermi surface on bands (a) α, (b) β, and (c) γ produced with our effective model colour coded with a measure of the orbital content, $|u^{\mu+}_{A\uparrow}(\boldsymbol{k})|^2 + |u^{\mu+}_{B\uparrow}(\boldsymbol{k})|^2$.

cuts at $k_z = 0,\ 2\pi$ are shown in Fig. 3.7. Though revealing an overall match, the k_z-warping of band β is slightly exaggerated in the effective model. However, this tiny discrepancy is not an unreasonable consequence of the serious and necessary simplification of projecting a 17-band model onto an effective three-band model. Such a simplification is needed to make the numerical procedure realistically feasible.

Finally, it should be commented that determining the global minimum of a high-dimensional function like Eq. (3.12) is not trivial, and our approach does not provide any guarantee of finding it. Furthermore, the energy landscape of $D(\{t\})$ is likely complicated and might contain numerous local minima. However, the quality of the resulting fit shown in Fig. 3.5 is arguably high enough to produce

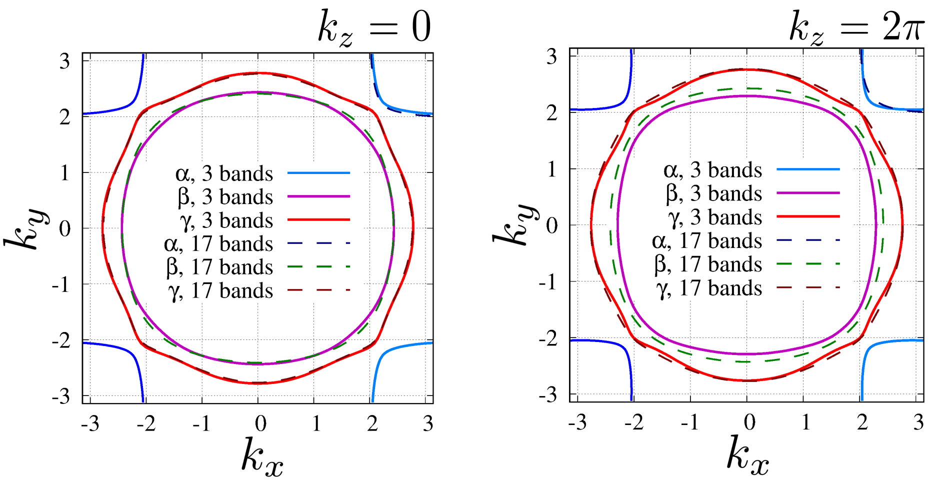

(a) (b)

Figure 3.7: Fermi surface cuts at (a) $k_z = 0$ and (b) $k_z = 2\pi$ for the three-band model of Eq. (3.2) and the 17-band model of Ref. [111].

an accurate, yet effective description of SRO that can serve as a testbed for advanced numerical calculations.

3.3 Weak-Coupling Theory with Multiple Bands

Building on the kinetic Hamiltonian of Eq. (3.1) proposed in the preceding section, we add repulsive on-site interaction terms to the description. Since we effectively treat a model for the $t_{2g} = \{4d_{xz}, 4d_{yz}, 4d_{xy}\}$ electron triplet, the interactions are more complicated than in the single-band case of Chapter 2. When projecting the on-site interactions onto the t_{2g} triplet, the phenomenological Coulomb interactions, known as Kanamori–Hubbard type interactions, read [123]

$$\begin{aligned} H_I = \frac{U}{2} \sum_{i,a,s\neq s'} n_{ias} n_{ias'} + \frac{U'}{2} \sum_{i,a\neq b,s,s'} n_{ias} n_{ibs'} \\ + \frac{J}{2} \sum_{i,a\neq b,s,s'} c^\dagger_{ias} c^\dagger_{ibs'} c_{ias'} c_{ibs} + \frac{J'}{2} \sum_{i,a\neq b,s\neq s'} c^\dagger_{ias} c^\dagger_{ias'} c_{ibs'} c_{ibs}. \end{aligned} \tag{3.13}$$

Here $n_{ias} = c^\dagger_{ias} c_{ias}$ is the density operator on site i and orbital a of spin s. The four phenomenological interaction parameters, U, J, U', and J', stem from Coulomb overlap integrals. From the overlap consideration the parameters are dependent and satisfy $U' = U - 2J$ and $J' = J$ [123]. Below, we will consider the weak-coupling limit in which the leading-order contribution to the two-particle vertex is $\mathcal{O}(U^2)$ such that an overall factor of U^2 can be factorised from the interaction. This leaves the single parameter J/U to characterise the effective interaction. This parameter is considered unknown, as discussed further in Subsection 3.4.1. A justification for employing the weak-coupling approach in the case of SRO is given in Subsection 3.4.3.

3.3.1 Balian–Werthamer Basis with Pseudo-Spins

A natural extension of Subsection 2.3.2 is to define an order parameter basis in which spins are replaced by good quantum numbers in the presence of SOC. It is desirable to arrange this in a fashion that reproduces the Balian–Werthamer basis of Subsection 2.3.2 when turning off SOC. As such, we define a basis at the level of pseudo-spins (and bands), as shown rigorously in Refs. [59, 128]. In this basis the order parameter is parametrised by the scalar pseudo-spin singlet d_0 and the vector pseudo-spin triplet $\boldsymbol{d}$ as

$$\begin{pmatrix} \Delta_{++}(\boldsymbol{k}) & \Delta_{+-}(\boldsymbol{k}) \\ \Delta_{-+}(\boldsymbol{k}) & \Delta_{--}(\boldsymbol{k}) \end{pmatrix} = \frac{1}{\sqrt{2}} \begin{pmatrix} -d_x(\boldsymbol{k}) + i d_y(\boldsymbol{k}) & d_z(\boldsymbol{k}) + d_0(\boldsymbol{k}) \\ d_z(\boldsymbol{k}) - d_0(\boldsymbol{k}) & d_x(\boldsymbol{k}) + i d_y(\boldsymbol{k}) \end{pmatrix}, \tag{3.14}$$

analogous to Eq. (2.33). Here, $\Delta_{\sigma\sigma'}(\boldsymbol{k})$ is the pair correlation between pseudo-spins σ and σ' (i.e. the order parameter) with band indices kept implicit. As still ensured by fermionic asymmetry, cf. Eq. (2.34), the $\boldsymbol{d}$-vector and d_0 have well-defined parity transformations: $d_0(-\boldsymbol{k}) = d_0(\boldsymbol{k})$ and $\boldsymbol{d}(-\boldsymbol{k}) = -\boldsymbol{d}(\boldsymbol{k})$.

3.3.2 Absence of Instability at First Order

With multiple bands and the interactions of Eq. (3.13), the structure of the first-order vertex from Fig. 2.1 (b) is involved compared to the single-band case. In this subsection we prove that, in this more complicated setting, the first-order vertex remains positive semi-definite so long as the ratio J/U is sufficiently small[8]. We quantify what is meant by "sufficiently" below. Negative eigenvalues at tree-level are generally not expected, as per Refs. [15, 116, 128–131], but providing a solid proof would be useful and instructive.

---

[8] A similar argument was originally formulated by Victor Emery (private communication with Steven Kivelson).

When diagonalising $\mathcal{H}_s(\boldsymbol{k})$ the interaction potential is transformed accordingly,

$$\begin{aligned} & V^{\mu_3\sigma_3\mu_4\sigma_4}_{\mu_1\sigma_1\mu_2\sigma_2}(\boldsymbol{k}_1,\boldsymbol{k}_2,\boldsymbol{k}_3,\boldsymbol{k}_4) \\ &\qquad = \sum_{\{a_i\},\{s_i\}} V^{a_3s_3a_4s_4}_{a_1s_1a_2s_2}\; u^{\mu_1\sigma_1}_{a_1s_1}(\boldsymbol{k}_1)u^{\mu_2\sigma_2}_{a_2s_2}(\boldsymbol{k}_2)\left[u^{\mu_3\sigma_3}_{a_3s_3}(\boldsymbol{k}_3)\right]^*\left[u^{\mu_4\sigma_4}_{a_4s_4}(\boldsymbol{k}_4)\right]^*, \end{aligned} \tag{3.15}$$

where the u's are the eigenvectors of $\mathcal{H}_s(\boldsymbol{k})$, as per Eq. (3.10). The interaction potential with spin and orbital indices, as appearing in Eq. (3.15), consistent with H_I from Eq. (3.13) is given by

$$\begin{aligned} V^{a_3s_3a_4s_4}_{a_1s_1a_2s_2} &= U\delta_{a_1a_2}\delta_{a_2a_3}\delta_{a_3a_4}\delta_{s_1\bar{s}_2}\delta_{s_3\bar{s}_4}(\delta_{s_2s_3}-\delta_{s_2s_4}) \\ &\quad + U'(1-\delta_{a_1a_2})(\delta_{a_1a_4}\delta_{a_2a_3}\delta_{s_1s_4}\delta_{s_2s_3}-\delta_{a_1a_3}\delta_{a_2a_4}\delta_{s_1s_3}\delta_{s_2s_4}) \\ &\quad + J(1-\delta_{a_1a_2})(\delta_{a_1a_3}\delta_{a_2a_4}\delta_{s_1s_4}\delta_{s_2s_3}-\delta_{a_1a_4}\delta_{a_2a_3}\delta_{s_1s_3}\delta_{s_2s_4}) \\ &\quad + J'(1-\delta_{a_2a_3})\delta_{a_1a_2}\delta_{a_3a_4}\delta_{s_1\bar{s}_2}(\delta_{s_1s_4}\delta_{s_2s_3}-\delta_{s_1s_3}\delta_{s_2s_4}). \end{aligned} \tag{3.16}$$

There is one diagram contributing to the even-parity vertex at tree-level, which is a multiband variant of Fig. 2.1 (b) corresponding to

$$\begin{aligned} \Gamma^{(1)}_{\mu_1\mu_2}(\boldsymbol{k}_1,\boldsymbol{k}_2) &= V^{\mu_2-\mu_2+}_{\mu_1+\mu_1-}(\boldsymbol{k}_1,-\boldsymbol{k}_1,-\boldsymbol{k}_2,\boldsymbol{k}_2) \\ &= \sum_{\{a_i\},\{s_i\}} V^{a_3s_3a_4s_4}_{a_1s_1a_2s_2}\; u^{\mu_1+}_{a_1s_1}(\boldsymbol{k}_1)u^{\mu_1-}_{a_2s_2}(-\boldsymbol{k}_1)\left[u^{\mu_2+}_{a_3s_3}(\boldsymbol{k}_2)u^{\mu_2-}_{a_4s_4}(-\boldsymbol{k}_2)\right]^*. \end{aligned} \tag{3.17}$$

A gauge choice for the eigenvectors allows us to relate pseudospin $\sigma = -$ to $\sigma = +$. We will adopt the convention of making the $a = C = xy$ component of the eigenvectors real[9], combined with $u^{\alpha-}_{as}(\boldsymbol{k}) = (-1)^{\delta_{a3}}[u^{\alpha+}_{as}(\boldsymbol{k})]^*$. We further enforce $u^{\alpha\sigma}_{as}(-\boldsymbol{k}) = u^{\alpha\sigma}_{as}(\boldsymbol{k})$ as motivated by the fact that $\mathcal{H}_s(-\boldsymbol{k}) = \mathcal{H}_s(\boldsymbol{k})$. Such a relation makes $\Gamma^{(1)}_{\mu_1\mu_2} \in \mathbb{R}$ explicitly.

To proceed, we note the following: A matrix of the form $G = \sum_{n=1}^{M}\alpha_n\left|v_n\right\rangle\left\langle v_n\right|$, made of complex orthogonal vectors $\langle v_n|v_m\rangle \propto \delta_{nm}$ and real coefficients α_n, is positive semi-definite if and only if $\alpha_n \geqslant 0\ \forall\ n$.

Serving as a warm-up exercise, we assume first no SOC and only a U-type interaction (as considered e.g. in Ref. [128]). Time-reversal symmetry in this case ensures that the eigenvectors satisfy $u_{as}(\boldsymbol{k}) = [u_{a\bar{s}}(-\boldsymbol{k})]^*$. The tree-level vertex,

---

[9] Private communication with Thomas Scaffidi.

when explicitly stating the spin indices in this case, is (cf. Eq. (3.17))

$$\begin{aligned} \Gamma^{(1)}_{\uparrow\downarrow}(\boldsymbol{k}_1,\boldsymbol{k}_2) &= U\sum_a u_{a\uparrow}(\boldsymbol{k}_1)u_{a\downarrow}(-\boldsymbol{k}_1)\left[u_{a\downarrow}(-\boldsymbol{k}_2)u_{a\uparrow}(\boldsymbol{k}_2)\right]^* \\ &= U\sum_a |u_{a\uparrow}(\boldsymbol{k}_1)|^2|u_{a\uparrow}(\boldsymbol{k}_2)|^2 \\ &= \left[U\sum_a \big||u_{a\uparrow}|^2\big\rangle\big\langle|u_{a\uparrow}|^2\big|\right]_{\boldsymbol{k}_1,\boldsymbol{k}_2}. \end{aligned} \tag{3.18}$$

Since this matrix explicitly has the same structure as G above, with $\alpha_a = U > 0$, it follows from the comment above that it is positive semi-definite. Note that the vectors and the matrix of Eq. (3.18) become finite-dimensional when the Fermi surface is discretised. One can also check positive semi-definiteness explicitly by using the definition of this property:

$$\langle v|\,\Gamma^{(1)}_{\uparrow\downarrow}\,|v\rangle = U\sum_a \big|\big\langle|u_{a\uparrow}|^2\big|v\big\rangle\big|^2 \geqslant 0 \;\; \forall\,|v\rangle \;\text{ iff }\; U \geqslant 0. \tag{3.19}$$

Clearly, the argument fails when the interaction is attractive $U < 0$.

Including all interaction terms in the multiband case (with $U' = U - 2J$, and $J' = J$) in the presence of SOC, the vertex can after some algebra be recast as

$$\begin{aligned} \Gamma^{(1)}_{\mu_1\mu_2}(\boldsymbol{k}_1,\boldsymbol{k}_2) = U&\sum_{a,s} u^{\mu_1+}_{as}(\boldsymbol{k}_1)u^{\mu_1-}_{a\bar{s}}(-\boldsymbol{k}_1)[u^{\mu_2-}_{a\bar{s}}(-\boldsymbol{k}_2)u^{\mu_2+}_{as}(\boldsymbol{k}_2)]^* \\ &+(U-3J)\sum_{a,\bar{a},s} u^{\mu_1+}_{as}(\boldsymbol{k}_1)u^{\mu_1-}_{\bar{a}s}(-\boldsymbol{k}_1)[u^{\mu_2-}_{\bar{a}s}(-\boldsymbol{k}_2)u^{\mu_2+}_{as}(\boldsymbol{k}_2)]^* \\ &+(U-2J)\sum_{a,\bar{a},s} u^{\mu_1+}_{as}(\boldsymbol{k}_1)u^{\mu_1-}_{\bar{a}\bar{s}}(-\boldsymbol{k}_1)[u^{\mu_2-}_{\bar{a}\bar{s}}(-\boldsymbol{k}_2)u^{\mu_2+}_{as}(\boldsymbol{k}_2)]^* \\ &+J\sum_{a,\bar{a},s_1,s_2} u^{\mu_1+}_{as_1}(\boldsymbol{k}_1)u^{\mu_1-}_{\bar{a}s_2}(-\boldsymbol{k}_1)[u^{\mu_2-}_{as_2}(-\boldsymbol{k}_2)u^{\mu_2+}_{\bar{a}s_1}(\boldsymbol{k}_2)]^*. \end{aligned} \tag{3.20}$$

Above, we introduced the notation $\bar{a} \neq a$, so the double sums over a and $\bar{a}$ are restricted by this criterion. From Eq. (3.20) it is clear that the property of Eq. (3.19) holds as long as $J/U \leqslant 1/3$. Observe thus that positive semi-definiteness is lost as soon as $J/U > 1/3$. The parameter regime $J/U > 1/3$ indicates an effectively attractive interaction, which we consider unphysical for a purely electronic pairing mechanism.

Since the vertex at first order is positive semi-definite, one needs to consider contributions at second order. The (negative-eigenvalue) solutions at second order are only of interest if they belong to the subsector defined by the kernel of the first-order vertex. Otherwise, the repulsive first-order term would be infinitely stronger in the weak-coupling limit. This is taken into account by including a projector onto the kernel of the first-order vertex in the pseudo-spin singlet channel as

$$P_{\mathrm{Ker}\left(\bar{\Gamma}^{(1)}\right)}\bar{\Gamma}^{(2)}P_{\mathrm{Ker}\left(\bar{\Gamma}^{(1)}\right)}, \tag{3.21}$$

where

$$P_{\mathrm{Ker}\left(\bar{\Gamma}^{(1)}\right)} = \sum_{|\psi\rangle\in\mathrm{Ker}\left(\bar{\Gamma}^{(1)}\right)} |\psi\rangle\,\langle\psi|\,. \tag{3.22}$$

In practice, when the Fermi surface is discretised, the dimension of Ker $\left(\bar{\Gamma}^{(1)}\right)$ (i.e. the “unconventional sector”) is very close to the dimension of $\bar{\Gamma}^{(1)}$. For instance, at $J/U = 0.10$ we found only eight positive eigenvalues[10] of $\bar{\Gamma}^{(1)}$ when using roughly 10^4 $\boldsymbol{k}$-points as the (linear) matrix dimension. The most repulsive solution among these eight is (expectedly) the BCS s-wave order parameter.

3.3.3 Second-Order Multiband Vertex

The proof of Subsection 3.3.2 makes it clear that one needs to consider second-order contributions to the two-particle vertex to determine the leading superconducting instability. We are thus interested in the multiband variants of the diagrams of Fig. 2.3. The theory of these diagrams was developed in Refs. [59, 116, 128]. Below, this theory is recapitulated in brief steps.

The generalised Lindhard function reads (cf. Eq. (2.26))

$$\begin{aligned}\chi^{\mu_2\sigma_2\sigma_2'}_{\mu_1\sigma_1\sigma_1'}(\boldsymbol{k}_1,\boldsymbol{k}_2) = -\sum_{\boldsymbol{p}}\sum_{\mu,\mu',\sigma,\sigma'} &\frac{f[\xi_\mu(\boldsymbol{p})] - f[\xi_{\mu'}(\boldsymbol{p}+\boldsymbol{q})]}{\xi_\mu(\boldsymbol{p}) - \xi_{\mu'}(\boldsymbol{p}+\boldsymbol{q})} \\ &\times\, V^{\mu'\sigma'\mu_2\sigma_2}_{\mu_1\sigma_1\mu\sigma}(\boldsymbol{k}_1,\boldsymbol{p},\boldsymbol{p}+\boldsymbol{q},\boldsymbol{k}_2)\; V^{\mu\sigma\mu_2\sigma_2}_{\mu_1\sigma_1'\mu'\sigma'}(-\boldsymbol{k}_1,\boldsymbol{p}+\boldsymbol{q},\boldsymbol{p},-\boldsymbol{k}_2),\end{aligned} \tag{3.23}$$

where $\boldsymbol{q} = \boldsymbol{k}_1 - \boldsymbol{k}_2$, and where the interaction potentials on the second line are given by Eq. (3.15). By direct insertion of Eq. (3.15), and by assuming the continuum limit $\sum_{\boldsymbol{p}} \to \frac{1}{(2\pi)^3}\int \mathrm{d}\boldsymbol{p}$, we readily have a recipe for calculating Eq. (3.23) in terms

---

[10] Using the numerical tolerance $|\lambda|/U < 10^{-11}$ eV^{-1} to define Ker $\left(\bar{\Gamma}^{(1)}\right)$.

of the eigenvalues and eigenvectors of $\mathcal{H}_s(\boldsymbol{k})$:

$$\begin{aligned}\chi^{\mu_2\sigma_2\sigma_2'}_{\mu_1\sigma_1\sigma_1'}(\boldsymbol{k}_1,\boldsymbol{k}_2) = &-\sum_{\{a_i\},\{s_i\}}\sum_{\{a_i'\},\{s_i'\}} V^{a_3s_3a_4s_4}_{a_1s_1a_2s_2}\,V^{a_3's_3'a_4's_4'}_{a_1's_1'a_2's_2'} \\ &\times u^{\mu_1\sigma_1}_{a_1s_1}(\boldsymbol{k}_1)\left[u^{\mu_2\sigma_2}_{a_4s_4}(\boldsymbol{k}_2)\right]^* u^{\mu_1\sigma_1'}_{a_1's_1'}(-\boldsymbol{k}_1)\left[u^{\mu_2\sigma_2'}_{a_4's_4'}(-\boldsymbol{k}_2)\right]^* \\ &\times \frac{1}{2}\int_{\mathrm{BZ}}\frac{\mathrm{d}\boldsymbol{p}}{(2\pi)^3}\sum_{\mu,\mu',\sigma,\sigma'}\frac{f[\xi_\mu(\boldsymbol{p})]-f[\xi_{\mu'}(\boldsymbol{p}+\boldsymbol{q})]}{\xi_\mu(\boldsymbol{p})-\xi_{\mu'}(\boldsymbol{p}+\boldsymbol{q})} \\ &\times u^{\mu\sigma}_{a_2s_2}(\boldsymbol{p})\left[u^{\mu'\sigma'}_{a_3s_3}(\boldsymbol{p}+\boldsymbol{q})\right]^* u^{\mu'\sigma'}_{a_2's_2'}(\boldsymbol{p}+\boldsymbol{q})\left[u^{\mu\sigma}_{a_3's_3'}(\boldsymbol{p})\right]^*.\end{aligned} \tag{3.24}$$

The factor of $\frac{1}{2}$ above is included to account for the elongated Brillouin zone in the $\hat{z}$-direction, as explained in Subsection 3.2.1. Next, we define the parity-projected linear combinations

$$(\chi_\pm)^{\mu_2\sigma_2\sigma_2'}_{\mu_1\sigma_1\sigma_1'}(\boldsymbol{k}_1,\boldsymbol{k}_2) = -\frac{1}{2}\left[\chi^{\mu_2\sigma_2\sigma_2'}_{\mu_1\sigma_1\sigma_1'}(\boldsymbol{k}_1,\boldsymbol{k}_2) \pm \chi^{\mu_2\sigma_2\sigma_2'}_{\mu_1\sigma_1\sigma_1'}(\boldsymbol{k}_1,-\boldsymbol{k}_2)\right]. \tag{3.25}$$

In the pseudo-spin singlet channel (even parity), the second-order contribution is then expressed compactly as

$$\Gamma^{(2)}_{d_0d_0} = (\chi_+)^{+-}_{+-} - (\chi_+)^{-+}_{+-}, \tag{3.26}$$

when leaving the $\boldsymbol{k}$-dependencies and the band indices implicit. In the pseudo-spin triplet channel (odd parity), the effective vertex in the $\boldsymbol{d}$-vector basis of Subsection 3.3.1 takes the block structure

$$\Gamma^{(2)}_{\boldsymbol{dd}} = \begin{pmatrix}\Gamma^{(2)}_{d_zd_z} & 0 & 0 \\ 0 & \Gamma^{(2)}_{d_xd_x} & \Gamma^{(2)}_{d_xd_y} \\ 0 & \Gamma^{(2)}_{d_yd_x} & \Gamma^{(2)}_{d_yd_y}\end{pmatrix}. \tag{3.27}$$

The various components above are related to the odd-parity vertex function as follows:

$$\Gamma^{(2)}_{d_zd_z} = (\chi_-)^{+-}_{+-} + (\chi_-)^{-+}_{+-}, \tag{3.28}$$

$$\Gamma^{(2)}_{d_xd_x} = \frac{1}{2}\left[(\chi_-)^{++}_{++} - (\chi_-)^{--}_{++} - (\chi_-)^{++}_{--} + (\chi_-)^{--}_{--}\right], \tag{3.29}$$

$$\Gamma^{(2)}_{d_xd_y} = \frac{i}{2}\left[-(\chi_-)^{++}_{++} - (\chi_-)^{--}_{++} + (\chi_-)^{++}_{--} + (\chi_-)^{--}_{--}\right], \tag{3.30}$$

$$\Gamma^{(2)}_{d_yd_x} = -\frac{i}{2}\left[-(\chi_-)^{++}_{++} + (\chi_-)^{--}_{++} - (\chi_-)^{++}_{--} + (\chi_-)^{--}_{--}\right], \tag{3.31}$$

$$\Gamma^{(2)}_{d_yd_y} = \frac{1}{2}\left[(\chi_-)^{++}_{++} + (\chi_-)^{--}_{++} + (\chi_-)^{++}_{--} + (\chi_-)^{--}_{--}\right]. \tag{3.32}$$

This establishes the technology required to calculate the multiband generalisation of Eq. (2.23):

$$\bar{\Gamma}_{d_i d_j;\mu_1\mu_2}(\boldsymbol{k}_1,\boldsymbol{k}_2) = \sqrt{\frac{\rho_{\mu_1}\bar{v}_{\mu_1}}{v_{\mu_1}(\boldsymbol{k}_1)}}\Gamma^{(2)}_{d_i d_j;\mu_1\mu_2}(\boldsymbol{k}_1,\boldsymbol{k}_2)\sqrt{\frac{\rho_{\mu_2}\bar{v}_{\mu_2}}{v_{\mu_2}(\boldsymbol{k}_2)}}, \tag{3.33}$$

where i, j run over $0, x, y, z$, and where $\boldsymbol{k}_1$ ($\boldsymbol{k}_2$) runs over Fermi surface sheet S_{μ_1} (S_{μ_2}). The band-dependent density of states, Fermi velocity, and average Fermi velocity are defined as in Eq. (2.24) with appropriate band indices added.

3.4 Numerical Results

In this section we present results for the leading pairing eigenvalues and order parameters obtained numerically as a function of the unknown interaction parameter J/U. In Section 3.5 the results are compared with two key experimental probes: the specific heat [100] and the magnetic susceptibilty as probed via the NMR Knight shift [19, 20].

Numerically, we follow the procedure of Chapter 2, i.e. we discretise the Fermi surface making Eq. (3.33) a finite-dimensional matrix to be diagonalised. The computational complexity of this task should not be underestimated. Naively, a single evaluation of Eq. (3.24) involves $2^8 \cdot 3^8 \approx 1.7 \cdot 10^6$ terms just from the spin and orbital sums. This number is of course reduced substantially due to the form of Eq. (3.16), but it highlights the fact that an efficient evaluation of $\chi^{\mu_2\sigma_2\sigma_2'}_{\mu_1\sigma_1\sigma_1'}$ is key to the feasibility of the calculation. We use around 3000 $\boldsymbol{k}$-points for each of the three Fermi surface sheets and regularise the integrand of Eq. (3.24) (evaluating the Lindhard function at a negligibly small but finite frequency). Although finite size effects are unavoidable numerically, the eigenvalues are expected to have converged within a few percent tolerance in the present context – as checked by varying the integration resolution. Since we need to compute the eigenvalues and eigenvectors of $\mathcal{H}_s$ repeatedly for different $\boldsymbol{k}$-values, an analytic routine for the diagonalisation of 3×3 Hermitian matrices is used [132]. We employ around 500 computing cores – computing sub-blocks of the matrix in Eq. (3.33) simultaneously in `Fortran 90` – over the duration of a few weeks to obtain the results presented below.

3.4.1 Coupling Strengths

The eigenvalues of the leading order parameters are presented in Fig. 3.8 for all irreps[11] and for the interaction parameter range $J/U \in [0.04, 0.20]$. This J/U range is motivated by various RPA [133, 134], one-dimensional renormalisation group [135], mean-field [136], and advanced density functional theory [134] studies, in which estimates for J/U are centred around $J/U \approx 0.1$ but range between 0.059 and 0.23. Based on the leading eigenvalues of Fig. 3.8 (highest T_c) we identify two regimes: for $J/U < 0.15$ pseudo-spin triplet helical p-wave (A_{1u}) order is favoured, and for $J/U > 0.15$ pseudo-spin singlet $d_{x^2-y^2}$-wave (B_{1g}) order is favoured.

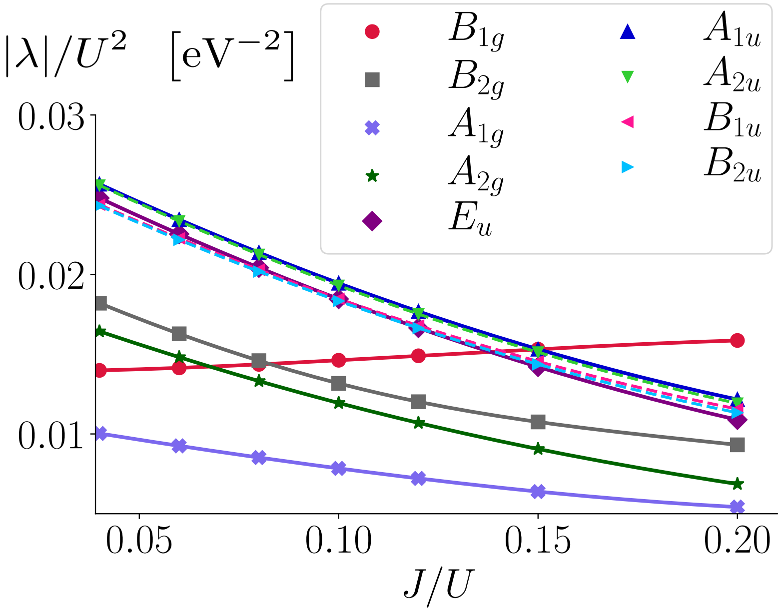

Figure 3.8: Leading (negative) pairing eigenvalues at second order as a function of the ratio of the spin-spin to the density-density interaction strength, J/U. The results are labelled by which irrep (see Table 2.1) the corresponding order parameter belongs to.

Compared to a previous weak-coupling study in 2D [116], in which a transition from chiral to helical p-wave order is found around $J/U \approx 0.06$, the helical sector is here marginally enhanced. All the odd-parity order parameters display the same qualitative trend in J/U, and the splitting between them remains small throughout. The splitting of the four helical states (irreps A_{1u}, A_{2u}, B_{1u}, and B_{2u}) is a small effect

---

[11] The E_g irrep does not appear in this figure because these states appear highly disfavoured. This is commented on below.

that crucially relies on the presence of $J/U \neq 0$, $\eta \neq 0$, and $\varepsilon_{AB} \neq 0$. The splitting order (and size) described here is consistent with that of 2D [116, 137]. Furthermore, the precise dependence of the splitting as a function of SOC and the inter-orbital ε_{AB} strength was recently revisited both analytically and numerically in 2D [138]. This analysis finds, via a Ginzburg–Landau approach, that chiral p-wave order is roughly speaking increasingly suppressed compared to the leading helical order as a function of increasing SOC and Hund's coupling, consistent with our 3D results.

The even-parity states display qualitatively different trends in J/U. In particular, the $d_{x^2-y^2}$-wave eigenvalue is enhanced with increasing Hund's coupling and enters the phase diagram in the weak-coupling limit, which was not found in 2D previously [116]. However, RPA studies do find this state favoured for intermediate values of the on-site interaction U, and it tends to be increasingly favoured with increasing J/U [117, 118, 138].

In three dimensions the possibility of an even-parity TRSB order parameter (irrep E_g) emerges. Such an order parameter has the structure $d_0 = f_z(f_x \pm i f_y)$ in the notation of Table 2.1, thereby having a robust horizontal line node at $k_z = 0$. This order was proposed as a way to reconcile nodal behaviour inferred from specific heat measurements with the observation of TRSB [121]. Interest in this state was further fueled by field-angle-dependent specific heat measurements [122], which suggested the presence of horizontal line nodes. It was recently proposed that an E_g order parameter can be stabilised by certain odd-k_z SOC terms for sufficiently large values of J/U [114]. In our weak-coupling calculation we find no evidence of this state being favoured in the considered J/U range. Instead, it appears highly disfavoured with a typical eigenvalue of $\lambda_{E_g}/\lambda_{B_{1g}} = \mathcal{O}(10^{-2})$. For instance, at $J/U = 0.20$ the leading candidate has $\lambda_{E_g}/\lambda_{B_{1g}}\big|_{J/U=0.20} \approx 0.03$ and thus does not come close to competing with the remaining nine orders shown of Fig. 3.8.

3.4.2 Order Parameters

To compare the two highest-T_c phases found numerically, we study the leading helical order parameter at $J/U = 0.06$ and the leading even-parity order parameter at

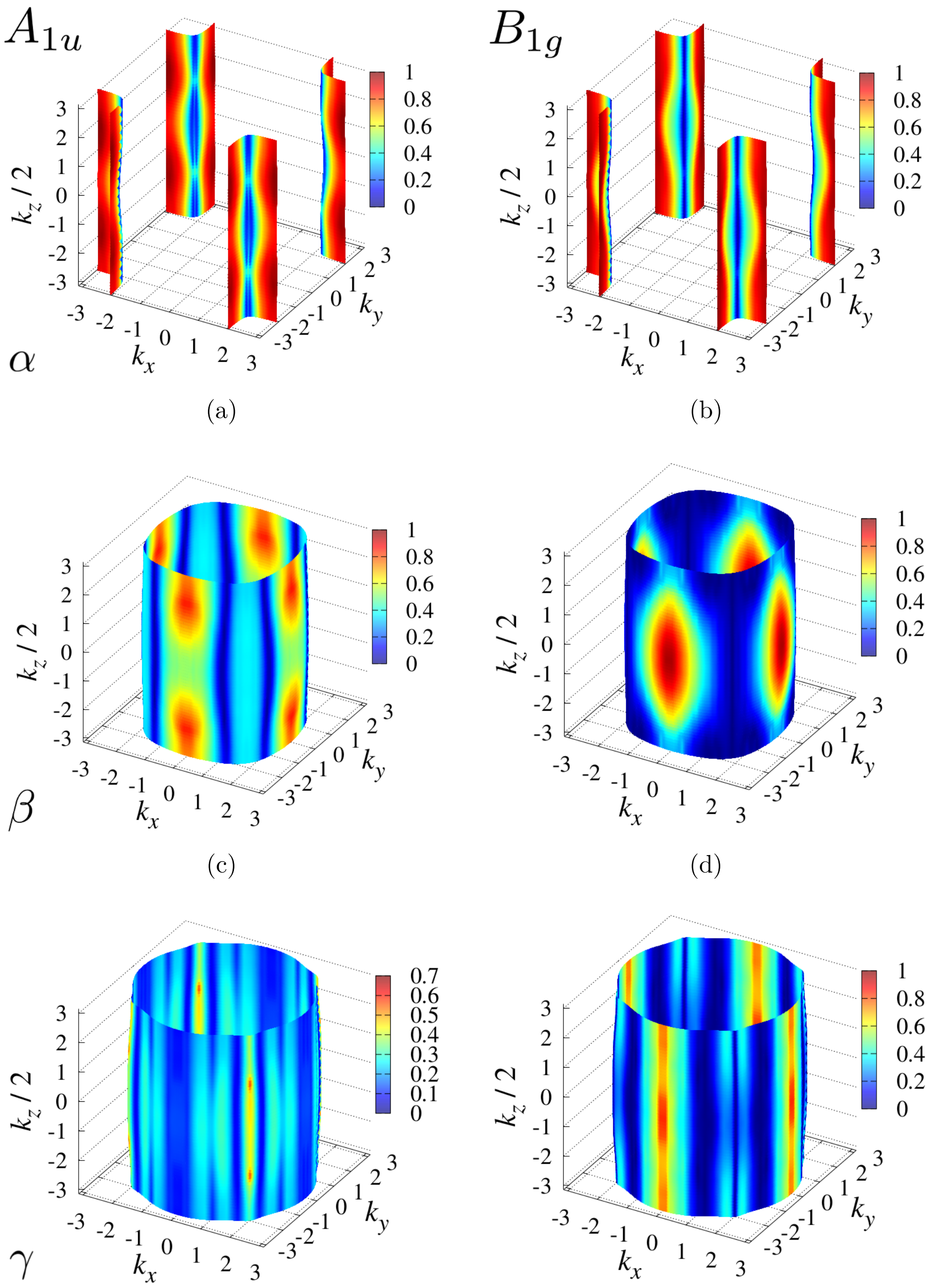

(a) (b)

(c) (d)

(e) (f)

Figure 3.9: Order parameter magnitude $|\Delta_\mu(\boldsymbol{k})|$ (colour coded) on the three Fermi surface sheets $\mu = \alpha, \beta, \gamma$ of (a), (c), (e) the leading helical p-wave order parameter (irrep A_{1u}) at $J/U = 0.06$, and (b), (d), (f) the leading even-parity $d_{x^2-y^2}$-wave order parameter (irrep B_{1g}) at $J/U = 0.20$. The order parameters are normalised by their the maximal value.

$J/U = 0.20$ as representative results. The J/U-dependence of the order parameters (their $\boldsymbol{k}$-structure) remain fairly weak in the entire range considered. Consequentially, the specific heat and the magnetic susceptibility, studied in Subsections 3.5.1 and 3.5.3, respectively, depend weakly on J/U. In Fig. 3.9 we display the magnitude of the leading helical and even-parity order parameters on the Fermi surface. To highlight further quantitative features, the same order parameters taken at the three cuts $k_z = 0, \pi, 2\pi$ are shown in Fig. 3.10.

A "textbook" helical (or chiral) p-wave order parameter on a cylindrical Fermi surface is naively expected to be fully gapped and approximately uniform. In sharp contrast, the helical order parameter in Fig. 3.9 (a), (c), (e), and Fig. 3.10 (a), (c), (e) is highly anisotropic on all three bands and displays deep vertical minima. The gap on β exhibits so deep minima that they can not practically be distinguished from accidental nodes given current experimental probes. Numerically, we find $\min_\theta |\Delta_\beta(\theta, k_z \approx \pi)| \lesssim 0.02\Delta_0$, where Δ_0 is the maximal gap and θ is the in-plane polar angle. The locations of these minima (see Fig. 3.10 (c)) are in agreement with previous predictions from 2D studies [104, 116, 139]. Highly anisotropic order parameters were also found in previous weak-coupling [116], RPA [117, 118, 138], and functional renormalisation group studies [140] in two dimensions. Despite the k_z-dependence in the order parameters on all bands, the order parameters remain overall fairly 2D, confirming the general expectation for such a layered perovskite material.

The $d_{x^2-y^2}$-wave order parameter shown in Fig. 3.9 (b), (d), (f), and Fig. 3.10 (b), (d), (f) has robust vertical line nodes along $|k_x| = |k_y|$. In addition, the sheets β and γ have large regions with a suppressed gap, implying a high residual density of states and low-temperature quasiparticles, to be discussed further in Subsection 3.5.1. The gap on sheets β and γ exhibits accidental vertical line nodes in addition to the robust ones along $|k_x| = |k_y|$.

3.4.3 Limitations of the Method

Before turning to how the results compare with experiments, we comment on the limitations of our model. In most real materials structurally similar to SRO

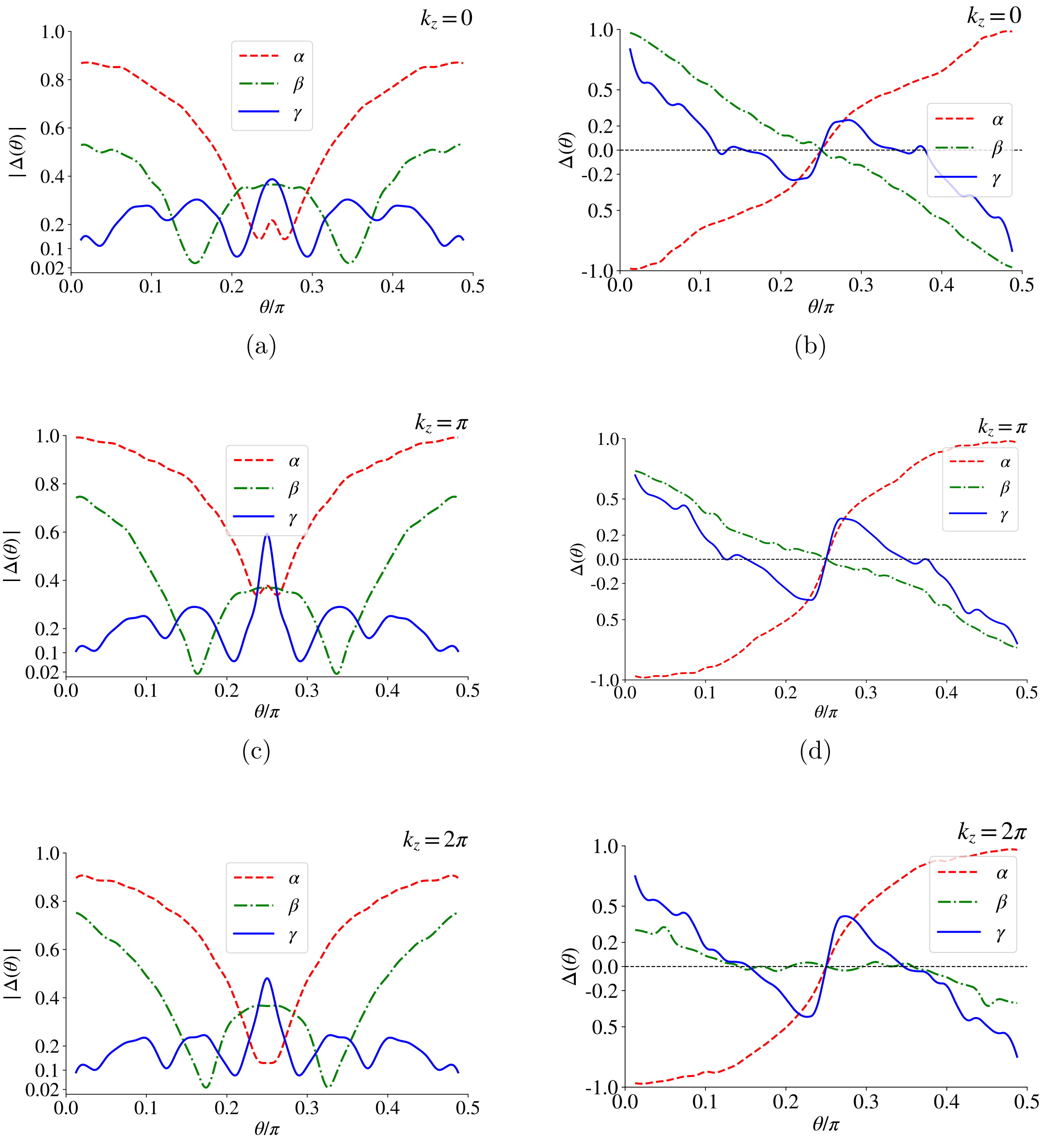

(a) (b)

(c) (d)

(e) (f)

Figure 3.10: In-plane cuts for the magnitude of (a), (c), (e) the helical order parameter at $J/U = 0.06$, and (b), (d), (f) the $d_{x^2-y^2}$-wave order parameter at $J/U = 0.20$. The in-plane angle θ is measured from (π, π, k_z) for the α Fermi surface sheet, and from $(0, 0, k_z)$ for sheets β and γ.

the weak-coupling limit is not expected to be strictly satisfied. Typical estimates of U fall in the $\mathcal{O}(\text{eV})$ range [133–136], which might seem devastating for the outlook of the approach taken here.

However, it should first be emphasised that $T_c/E_F \approx \mathcal{O}(10^{-4})$ in SRO, which is orders of magnitude below values applicable to the strongly coupled cuprates. Compared with the original Kohn–Luttinger estimate of Eq. (2.1), there is thus hope that the weak-coupling framework can capture the quantitatively correct T_c/E_F.

Secondly, previous studies of the Hubbard model have indicated that certain quantities, such as the ground state energy, can be well approximated by the weak-coupling results beyond $U/t > 1$ [141, 142]. As far as superconductivity is concerned, a recent survey compared three numerical methods for a single-band 2D Hubbard model close to half-filling for a range of coupling strengths [85]. This study found that both the superconducting order parameters and their ordering in the spectrum depended weakly on U, suggesting a smooth crossover from weak to strong coupling. One might reasonably expect this to carry over to 3D. However, as mentioned in Section 2.6, we stress that superconductivity in the 2D Hubbard model remains a controverisal topic [86].

Finally, all numerical methods have weaknesses, and the weak-coupling scheme is one of the few controlled and realistically feasible approaches given the complexity of our calculation.

3.5 Comparison with Experiment

Having identified two distinct orders in the effective model for SRO, the next task is to calculate experimentally relevant probes for which the two phases can be distinguished. In light of the recent pivotal development for the NMR Knight shift measurements [19, 20], the magnetic susceptibility is a highly relevant quantity to compare for the two identified orders. This is done in Subsection 3.5.3. First, in Subsection 3.5.1, we compute another long-standing and experimentally relevant probe, namely the specific heat [90, 100–102, 109].

3.5.1 Specific Heat

We adopt the commonly accepted convention of assuming that the temperature-dependent order parameter factorises as

$$\Delta_\mu(T,\boldsymbol{k}) = \Delta(T)\Delta_\mu(\boldsymbol{k}), \tag{3.34}$$

where $\Delta_\mu(\boldsymbol{k})$ is the weak-coupling order parameter of band μ, which satisfies $\max_{\boldsymbol{k},\mu}|\Delta_\mu(\boldsymbol{k})| = 1$. We further assume that $\Delta(T)$ has a BCS-like temperature-dependence[12] [58]. For an isotropic BCS superconductor, the overall size of the gap would follow from the well-known relation $\Delta(0)/(k_BT_c) = \pi\exp(-\gamma)$ [58], where $\gamma \approx 0.5772$ is the Euler–Mascheroni constant. This relation is, however, modified for an anisotropic superconductor; the generalised relation reads [69]

$$\frac{\Delta(0)}{k_BT_c} = \pi\exp\bigl(-\gamma - \bigl\{\ln|\Delta|\bigr\}_{\mathrm{FS}}\bigr), \tag{3.35}$$

where we introduced the averaging symbol

$$\bigl\{\ln|\Delta|\bigr\}_{\mathrm{FS}} \equiv \frac{\sum_\mu \int_{S_\mu} \mathrm{d}\boldsymbol{k}\, \frac{|\Delta_\mu(\boldsymbol{k})|^2}{v_\mu(\boldsymbol{k})} \ln|\Delta_\mu(\boldsymbol{k})|}{\sum_\nu \int_{S_\nu} \mathrm{d}\boldsymbol{k}\, \frac{|\Delta_\nu(\boldsymbol{k})|^2}{v_\nu(\boldsymbol{k})}}. \tag{3.36}$$

Hence, if we take the experimental value of $T_c \approx 1.48$ K as input [79], the function $\Delta_\mu(T,\boldsymbol{k})$ is fully determined, given the results of Section 3.4.

The specific heat for a multiband superconductor comes from the expression of the entropy in a fermion gas [58],

$$S = -2k_B \sum_{\boldsymbol{k},\mu} \Bigl[f[E_\mu(\boldsymbol{k})]\ln f[E_\mu(\boldsymbol{k})] + \bigl(1 - f[E_\mu(\boldsymbol{k})]\bigr)\ln\bigl(1 - f[E_\mu(\boldsymbol{k})]\bigr)\Bigr]. \tag{3.37}$$

Here, $E_\mu(\boldsymbol{k}) = \sqrt{\xi_\mu^2 + |\Delta_\mu(T,\boldsymbol{k})|^2}$, and $f(E) = (1+\exp(\beta E))^{-1}$ is the Fermi function. The specific heat follows from standard thermodynamic relations as

$$\begin{aligned} C(T) &= T\frac{\partial S}{\partial T} = 2\sum_{\boldsymbol{k},\mu} E_\mu(\boldsymbol{k}) \frac{\mathrm{d}f(E_\mu(\boldsymbol{k}))}{\mathrm{d}T} \\ &= \frac{2}{k_BT^2}\int_{-\infty}^{\infty} \mathrm{d}\xi_\mu \left\langle \frac{\xi_\mu^2 + \Delta(T)^2|\Delta_\mu(\boldsymbol{k})|^2 - \frac{T}{2}\frac{\partial\Delta(T)^2}{\partial T}|\Delta_\mu(\boldsymbol{k})|^2}{4\cosh^2(\frac{E_\mu(\boldsymbol{k})}{2k_BT})} \right\rangle_{\mathrm{FS}}, \end{aligned} \tag{3.38}$$

---

[12] To be precise, we utilise the numerical approximation $\Delta(T)/\Delta(0) \approx \tanh\bigl(1.74\sqrt{T_c/T - 1}\bigr)$ which approximates the numerical solution to the gap equation in the entire temperature range with sufficient precision for our purposes.

where the Fermi surface average is evaluated according to

$$\langle A\rangle_{\mathrm{FS}} \equiv \sum_{\mu} \frac{\rho_\mu}{|S_\mu|} \int_{S_\mu} \mathrm{d}\boldsymbol{k}\; A. \tag{3.39}$$

One can validate the derivation by evaluating Eq. (3.38) in the normal state, in which $\Delta = 0$. As such, the normal-state specific heat per temperature, denoted by γ_n, is obtained:

$$\gamma_n \equiv \frac{C_n(T)}{T} = \frac{2}{k_B T^3} \sum_{\mu} \rho_\mu \int_{-\infty}^{\infty} \mathrm{d}\xi \frac{\xi^2}{4\cosh^2(\frac{\xi}{2k_B T})} = 4k_B^2 \zeta(2) \sum_{\mu} \rho_\mu, \tag{3.40}$$

Above, ζ is the Riemann zeta function, with $\zeta(2) = \pi^2/6$. This recovers the multiband version of the well-known (electronic) linear contribution to the specific heat of a metal [58].

It is convenient to normalise Eq. (3.38) by the normal-state value to obtain an expression that can be computed numerically and directly compared with experiment:

$$\frac{C(T)}{T\gamma_n} = \frac{3}{4\pi^2 (k_B T)^3 \sum_\nu \rho_\nu} \int_{-\infty}^{\infty} \mathrm{d}\xi \left\langle \frac{\xi^2 + \Delta(T)^2 |\Delta_\mu(\boldsymbol{k})|^2 - \frac{T}{2}\frac{\partial \Delta(T)^2}{\partial T} |\Delta_\mu(\boldsymbol{k})|^2}{\cosh^2(\frac{E_\mu(\boldsymbol{k})}{2k_B T})} \right\rangle_{\mathrm{FS}}. \tag{3.41}$$

For the two order parameters studied in Subsection 3.4.2 Eq. (3.41) is evaluated numerically; the results are shown in Fig. 3.11. The specific heat for both orders are shown along with the experimental values adapted from Ref. [100] for reference. Both helical p-wave and d-wave orders reproduce the overall tendencies of the experimental values. The vertical minima in the helical order parameter, in particular on bands β and γ, are deep enough to make the specific heat drop exponentially below a temperature of about $T/T_c \lesssim 0.05$, as revealed by Fig. 3.11 (a). Temperatures of $T \approx 70$ mK might be accessible experimentally, but resolving the difference between linearity and exponential suppression at such low temperatures is likely to remain problematic practically[13]. The d-wave order, as noted before, exhibits substantial regions of the Fermi surface with a suppressed gap in addition to robust vertical line nodes. This results in low-lying quasiparticles and a residual heat

---

[13] At low temperatures contributions to the specific heat from impurity spins make accurate measurements problematic.

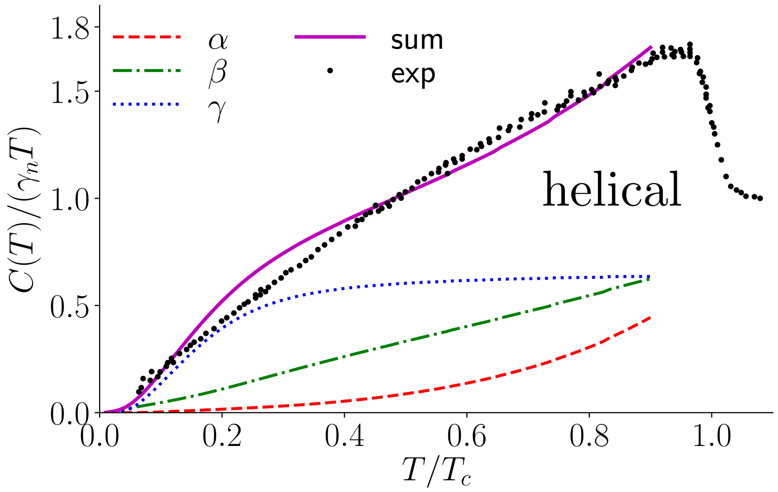

(a)

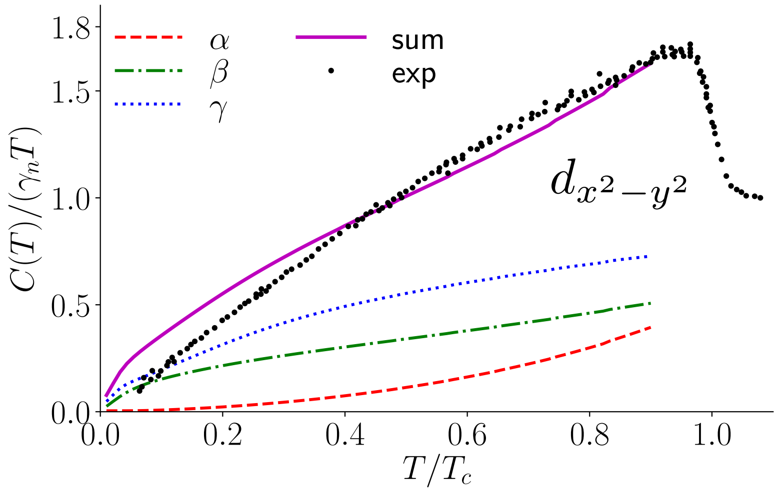

(b)

Figure 3.11: The calculated specific heat divided by temperature and the normal-state value, γ_n, as per Eq. (3.41). The results are shown for (a) the helical p-wave order parameter (irrep A_{1u}) at $J/U = 0.06$, and (b) the $d_{x^2-y^2}$-wave order parameter (irrep B_{1g}) at $J/U = 0.20$. Dashed, dot dashed, and dotted lines indicate contributions from the α, β, and γ bands, respectively. The results are compared to experimental values (black dots), adapted from Ref. [100], see Fig. 3.3.

capacity at low temperatures, providing a slight deviation from the experiment. Despite this, the match between the experiment and the specific heat for d-wave order is arguably more convincing qualitatively than the match with helical order. Note that although the experimental curve is relatively linear and featureless, a comparable gap on all three bands seems necessary to reproduce the delicate sum of band-contributions that the experimental data impose [90, 116, 143].

Recent thermal conductivity measurements were interpreted to suggest that vertical line nodes are present on all three bands [103]. In a subsequent calculation it was shown that deep minima in odd-parity order parameters actually would suffice to explain the thermal conductivity data [104]. Hence, it appears likely that both orders found and discussed here would be in agreement with the experiment. Serving as a future direction, it would be desirable to perform a microscopic calculation to evaluate this quantitatively.

To summarise, both the helical p-wave and the d-wave order parameters practically exhibit nodal behaviour. Consequentially, distinguishing these orders from the specific heat appears difficult. However, it should be noted that the deep minima in the gap on sheets β and γ for the helical order are shifted from the diagonal $\theta = \pi/4$ line. Probes sensitive to the $\boldsymbol{k}$-structure of the gap, like scanning tunnelling microscopy (STM), are in principle capable of detecting this shift. Recently, STM measurements were performed [144]. The experimental results appear to be most consistent with B_{1g} order parameter symmetry.

3.5.2 Magnetic Susceptibility: Derivation

Another experimental probe useful to consider is the spin susceptibility, as measured via the NMR Knight shift [19, 20]. Consider first the normal-state Hamiltonian in the presence of an external magnetic field:

$$H = H_0 + H_S + H_L. \tag{3.42}$$

Here, H_0 is the normal-state Hamiltonian in the absence of a magnetic field, as given by Eq. (3.1). The Zeeman coupling between the magnetic field $\boldsymbol{H}$ and spins $\boldsymbol{S}$ is denoted by H_S, and the Zeeman coupling between $\boldsymbol{H}$ and the orbital degrees of freedom is denoted by H_L. The various terms are explicitly given by (cf. Ref. [145]):

$$H_0 = \sum_{\boldsymbol{k},s,s'} \sum_{a,b,c} \left(\varepsilon_{ab}(\boldsymbol{k}) + i\eta\epsilon_{abc}\sigma^c_{ss'}\right) c^\dagger_{as}(\boldsymbol{k}) c_{bs'}(\boldsymbol{k}), \tag{3.43}$$

$$H_S = -2\mu_B \boldsymbol{H} \cdot \boldsymbol{S} = -\mu_B \sum_{\boldsymbol{k},s,s'} \sum_{a,b} H_b \sigma^b_{ss'} c^\dagger_{as}(\boldsymbol{k}) c_{as'}(\boldsymbol{k}), \tag{3.44}$$

$$H_L = -\mu_B \boldsymbol{H} \cdot \boldsymbol{L} = -\mu_B i \sum_{\boldsymbol{k},s} \sum_{a,b,c} H_c \epsilon_{abc} c^\dagger_{as}(\boldsymbol{k}) c_{bs}(\boldsymbol{k}). \tag{3.45}$$

Above, $\varepsilon_{ab}(\boldsymbol{k})$ are the orbital energies as determined in Subsection 3.2.1, σ^a is the a'th Pauli matrix, and ϵ_{abc} is the Levi–Civita symbol, with a, b, c running over Ru $4d$ orbitals xz, yz, xy (with the shorthand notation A, B, C, respectively). Moreover, μ_B is the Bohr magneton, and the vacuum permeability was fixed to $\mu_0 = 1$.

When recast as matrices we have

$$H = \sum_{\boldsymbol{k}} \boldsymbol{\psi}^\dagger(\boldsymbol{k})\big(\mathcal{H}_0(\boldsymbol{k}) + \mathcal{H}_S + \mathcal{H}_L\big)\boldsymbol{\psi}(\boldsymbol{k}), \tag{3.46}$$

$$\boldsymbol{\psi}(\boldsymbol{k}) = [c_{A\uparrow}(\boldsymbol{k}), c_{B\uparrow}(\boldsymbol{k}), c_{C\downarrow}(\boldsymbol{k}), c_{A\downarrow}(\boldsymbol{k}), c_{B\downarrow}(\boldsymbol{k}), c_{C\uparrow}(\boldsymbol{k})]^T. \tag{3.47}$$

Due to broken time-reversal symmetry in the presence of the magnetic field, the pseudo-spin blocks $\sigma = +$ and $\sigma = -$ are no longer degenerate, and we need to consider the full 6×6 structure explicitly. The Fermi surface sheets, defined by $\xi_{\mu\sigma}(\boldsymbol{k}) = 0$, correspondingly split in σ for each band. To state the matrices of Eq. (3.46) explicitly, we still have $\mathcal{H}_0(\boldsymbol{k}) = \mathcal{H}_{s=+1}(\boldsymbol{k}) \oplus \mathcal{H}_{s=-1}(\boldsymbol{k})$, with $\mathcal{H}_s(\boldsymbol{k})$ as given in Eq. (3.2). In terms of the magnetic field components H_i for $i = x, y, z$, the matrices $\mathcal{H}_S$ and $\mathcal{H}_L$ take the forms:

$$\mathcal{H}_S = -\mu_B \left(\begin{array}{ccc|ccc} H_z & 0 & 0 & H_x - iH_y & 0 & 0 \\ 0 & H_z & 0 & 0 & H_x - iH_y & 0 \\ 0 & 0 & -H_z & 0 & 0 & H_x + iH_y \\ \hline H_x + iH_y & 0 & 0 & -H_z & 0 & 0 \\ 0 & H_x + iH_y & 0 & 0 & -H_z & 0 \\ 0 & 0 & H_x - iH_y & 0 & 0 & H_z \end{array}\right), \tag{3.48}$$

and

$$\mathcal{H}_L = -\mu_B i \left(\begin{array}{ccc|ccc} 0 & 0 & -H_y & 0 & H_z & 0 \\ 0 & 0 & H_x & -H_z & 0 & 0 \\ H_y & -H_x & 0 & 0 & 0 & 0 \\ \hline 0 & H_z & 0 & 0 & 0 & -H_y \\ -H_z & 0 & 0 & 0 & 0 & H_x \\ 0 & 0 & 0 & H_y & -H_x & 0 \end{array}\right). \tag{3.49}$$

Finally, we define the matrix $U(\boldsymbol{k})$ to diagonalise $\mathcal{H}_0(\boldsymbol{k}) + \mathcal{H}_S + \mathcal{H}_L$. Along with the energies $\xi_{\mu\sigma}(\boldsymbol{k})$, calculating the components of $U(\boldsymbol{k})$ is enough to establish the magnetisation in the normal state, as described below.

For a tetragonal lattice the susceptibility tensor is diagonal [146]. When the external magnetic field is applied along coordinate direction $\hat{\imath}$, $\boldsymbol{H} \parallel \hat{\imath}$, and we consider the magnetic response along the same direction, the normal-state magnetisation elements can be defined as thermal expectation values (cf. Ref. [118]):

$$\mathcal{M}^{ii} \equiv \frac{1}{2} \sum_{a,s_1,s_2} \sigma^i_{s_1 s_2} M^{s_1 s_2}_a \Big|_{\boldsymbol{H} \| \hat{i}}, \tag{3.50}$$

$$M^{s_1 s_2}_a = \mu_B \sum_{\boldsymbol{k}} \left\langle c^\dagger_{a s_1}(\boldsymbol{k}) c_{a s_2}(\boldsymbol{k}) \right\rangle. \tag{3.51}$$

Note that the magnetic field couples to the physical spin (not to pseudo-spin). The transformation between electronic operators in orbital and spin basis (indexed by a and s), and band and pseudo-spin basis is given by Eq. (3.10). We combine this transformation with the thermal expectation values

$$\left\langle c^\dagger_{\mu\sigma}(\boldsymbol{k}) c_{\nu\sigma'}(\boldsymbol{k}) \right\rangle = f\left[\xi_{\mu\sigma}(\boldsymbol{k})\right] \delta_{\mu\nu} \delta_{\sigma\sigma'}, \tag{3.52}$$

where f is the Fermi function, to obtain the normal-state magnetisation matrix elements as

$$M^{s_1 s_2}_a = \mu_B \sum_{\boldsymbol{k},\mu,\sigma} \left[u^{\mu\sigma}_{a s_1}(\boldsymbol{k})\right]^* u^{\mu\sigma}_{a s_2}(\boldsymbol{k}) f(\xi_{\mu\sigma}(\boldsymbol{k})). \tag{3.53}$$

In order to extend the framework to the superconducting state (at mean-field level), we add superconducting terms to the Hamiltonian in Eq. (3.42):

$$H_\Delta = \sum_{\boldsymbol{k}} \sum_{a_1,a_2,s,s'} \Delta^{a_1 a_2}_{s_1 s_2}(\boldsymbol{k}) c^\dagger_{a_1 s}(\boldsymbol{k}) c^\dagger_{a_2 s'}(-\boldsymbol{k}) + \text{h.c.}, \tag{3.54}$$

where $\Delta^{a_1 a_2}_{s_1 s_2}(\boldsymbol{k})$ is the order parameter in orbital and spin basis. For the various order parameter channels, as defined in the $\boldsymbol{d}$-vector basis of Subsection 3.3.1, we decompose the components $\Delta^{a_1 a_2}_{s_1 s_2}(\boldsymbol{k})$ in the same fashion according to

$$\Delta^{a_1 a_2}_{(d_0,\boldsymbol{d}),s_1 s_2}(\boldsymbol{k}) = \left[\left(\Delta^{a_1 a_2}_{d_0}(\boldsymbol{k}) \mathbb{1} + \sum_{j=x,y,z} \Delta^{a_1 a_2}_{d_j}(\boldsymbol{k}) \sigma_j\right) i\sigma_y\right]_{s_1 s_2}. \tag{3.55}$$

The individual order parameter components appearing on the right hand side of Eq. (3.55), $\Delta^{a_1 a_2}_{d_i,s_1 s_2}(\boldsymbol{k})$ for $i = 0, x, y, z$, are related to the order parameter in band and pseudo-spin basis obtained numerically in Section 3.4, $\Delta^{\mu}_{d_i,\sigma_1\sigma_2}(\boldsymbol{k})$, via the transformation

$$\Delta^{a_1 a_2}_{d_i,s_1 s_2}(\boldsymbol{k}) = \sum_{\mu,\sigma_1,\sigma_2} \Delta^{\mu}_{d_i,\sigma_1\sigma_2}(\boldsymbol{k}) \left[u^{\mu\sigma_1}_{a_1 s_1}(\boldsymbol{k}) u^{\mu\sigma_2}_{a_2 s_2}(-\boldsymbol{k}) + u^{\mu\sigma_2}_{a_1 s_1}(\boldsymbol{k}) u^{\mu\sigma_1}_{a_2 s_2}(-\boldsymbol{k})\right]. \tag{3.56}$$

Above, $u_{as}^{\mu\sigma}(\boldsymbol{k})$ are still components of the eigenvectors of $\mathcal{H}_0(\boldsymbol{k})$, crucially in the absence of the magnetic field.

Adding the superconducting terms results in a doubling of the matrix size as compared to the normal state. The full Hamiltonian, with energies $E_{\mu\sigma}(\boldsymbol{k})$, is by particle-hole symmetry subject to a $\pm E$ symmetry in the spectrum. The electron operators are correspondingly expressed as combinations of particles (u's) and holes (v's):

$$c_{as}(\boldsymbol{k}) = \sum_{\mu,\sigma} \left[u_{as}^{\mu\sigma}(\boldsymbol{k}) c_{\mu\sigma}(\boldsymbol{k}) + v_{as}^{\mu\sigma}(-\boldsymbol{k}) c_{\mu\sigma}^{\dagger}(-\boldsymbol{k})\right]. \tag{3.57}$$

Carrying out the same computation as before now results in (cf. Eq.(3.53))

$$\begin{aligned} M_a^{s_1 s_2} = \mu_B \sum_{\boldsymbol{k},\mu,\sigma} \Big(&\left[u_{as_1}^{\mu\sigma}(\boldsymbol{k})\right]^* u_{as_2}^{\mu\sigma}(\boldsymbol{k}) f(E_{\mu\sigma}(\boldsymbol{k})) \\ &+ \left[v_{as_1}^{\mu\sigma}(-\boldsymbol{k})\right]^* v_{as_2}^{\mu\sigma}(-\boldsymbol{k}) \left[1 - f(E_{\mu\sigma}(-\boldsymbol{k}))\right] \Big). \end{aligned} \tag{3.58}$$

Finally, we define a proxy of the Knight shift K^i as the ratio of the magnetic susceptibility tensor component χ^{ii} in the superconducting to the normal-state value χ_n^{ii} as

$$K^i(T) \equiv \frac{\chi^{ii}(T)}{\chi_n^{ii}} = \frac{\delta\mathcal{M}^{ii}(T)}{\delta\mathcal{M}_n^{ii}}. \tag{3.59}$$

Here, δ refers to an infinitesimal increment in the external magnetic field strength when being in the linear response regime (meaning at sufficiently small external magnetic fields). Numerically, the momentum sums of Eq. (3.58) at finite temperature requires knowledge of the order parameter away from the Fermi surface. To facilitate this we adopt the approach of Ref. [118]: for a given $\boldsymbol{k}$ we associate to it the order parameter on the Fermi surface closest to $\boldsymbol{k}$ multiplied with a Gaussian damping factor, where the damping exponent is proportional to the distance between $\boldsymbol{k}$ and the Fermi surface[14].

---

[14] The final result, i.e. value of K^i, is practically insensitive to the damping strength for reasonably weak damping strengths.

3.5.3 Magnetic Susceptibility: Evaluation

Numerically, Eq. (3.59) is evaluated for the leading A_{1u} and E_u order parameters at $J/U = 0.06$, and for the leading B_{1g} order parameter at $J/U = 0.20$. In the results presented below the orbital coupling $\mathcal{H}_L$ was left out for the reason that in all cases checked it turned out to give only minor corrections to K^i. Moreover, it remains unclear from the experiment whether the $\mathcal{H}_L$ term is actually probed. Investigating this term in detail is left for future work.

In the absence of SOC and with a single band, the analysis greatly simplifies, as summarised in Fig. 3.12. The resulting spin susceptibility for an in-plane magnetic field in the singlet channel is in this case related to the so-called Yosida function $Y(T)$ [18]. Though the specific shape of $Y(T)$ depends on where the order parameter is nodal, the limit $\lim_{T\to 0} Y(T) = 0$ is independent of the nodal configuration. In contrast, the $T = 0$ value of the spin susceptibility in the spin triplet channel distinguishes the helical p-wave states ($\frac{1}{2}$) from the chiral p-wave (1) state. Values of $K^x(T = 0)$ and $K^z(T = 0)$ in the case of SRO are listed in Table 3.4, where we contrast the results with those expected for the "textbook" cases of Fig. 3.12.

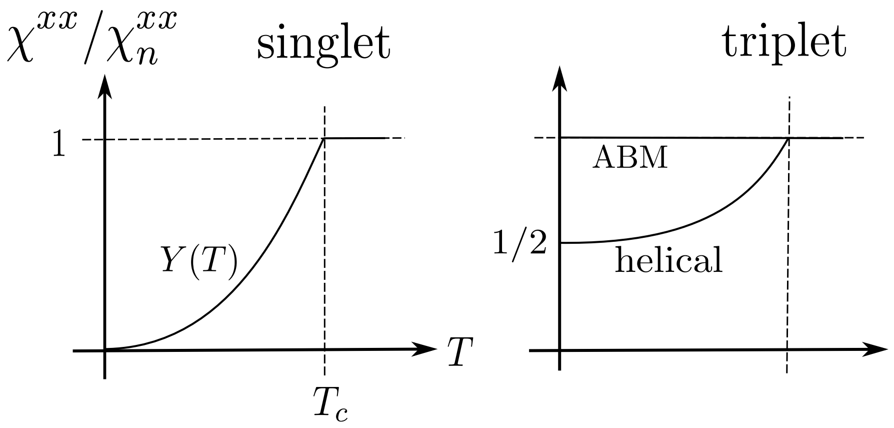

Figure 3.12: The spin susceptibility as a function of temperature for an in-plane magnetic field, $\chi^{xx}(T)$, per normal-state value, χ_n^{xx}, with a cylindrical Fermi surface in the absence of SOC. Left: spin singlet; the spin susceptibility is goverened by the Yosida function, $Y(T)$, that goes to zero as $T \to 0$ irrespectibly of the order parameter details. Right: spin triplet; the chiral p-wave state (ABM) yields no drop in $\chi^{xx}(T < T_c)/\chi_n^{xx}$, whereas the drop is to $\frac{1}{2}$ at $T = 0$ for the helical states. Figure inspired by Ref. [69].

Table 3.4: Computed magnetic susceptibility normalised by the normal-state value at zero temperature, $K^i(T=0) = \chi^{ii}(T=0)/\chi^{ii}_n$, for SRO. The values in parenthesis show the results expected for “textbook” order parameters without SOC.

Irrep	Name	$K^x(T=0)$	$K^z(T=0)$
B_{1g}	d-wave	0.45 (0.0)	0.59 (0.0)
A_{1u}	helical p-wave (BW)	0.59 (0.5)	0.97 (1.0)
E_u	chiral p-wave (ABM)	0.99 (1.0)	0.58 (0.0)

With SOC present the spin singlet and spin triplet mix and form Cooper pairs of well-defined pseudo-spin. The mixing results in similar values of $K^x(T=0)$ for the helical and d-wave cases: $K^x_{B_{1g}}(T=0) = 0.45$ at $J/U = 0.20$ and $K^x_{A_{1u}}(T=0) = 0.59$ at $J/U = 0.06$. Both these numbers are in vicinity of the experimental value of $K^x(T = 20\text{ mK}) \approx 0.5$ [19], for which the uncertainty is likely greater than 0.1. These numbers should be contrasted with the chiral p-wave case, which sharply conflicts with the experiment: $K^x(T=0) = 0.99$. Taking into account that chiral p-wave has been the prevailing hypothesis for the order parameter of SRO for about two decades, this is a surprising result.

The temperature-dependent spin susceptibility results are shown in Fig. 3.13 for (a) an in-plane magnetic field, and for (b) an out-of plane magnetic field. The drop in K^x to around 0.5, as observed at $T = 20$ mK [19], was recently reproduced by the Ishida group in Ref. [20]. In the latter experiment, the temperature-dependence of the Knight shift was also measured, which we have plotted for two oxygen sites in Fig. 3.13 (a) for comparison. Taking into account the experimental precision, it is problematic to clearly distinguish helical p-wave from d-wave order. However, the d-wave order is arguably in better agreement with the experimental data at low temperatures. Our results appear in good agreement with those of a recent RPA study in 2D [118], despite somewhat different $\boldsymbol{k}$-dependencies of the order parameters.

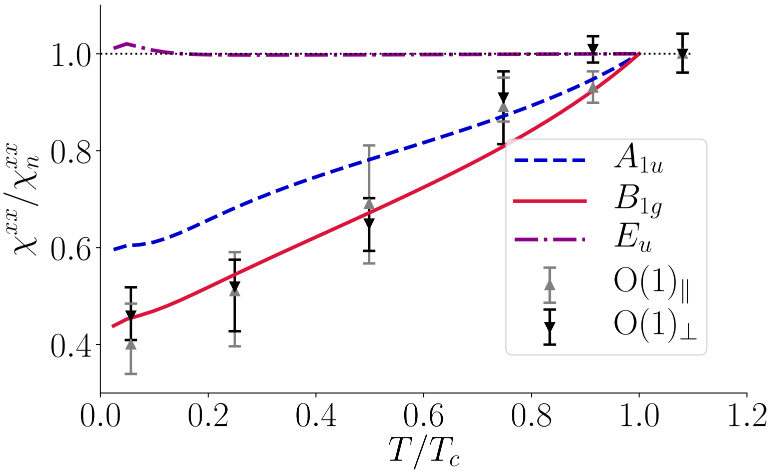

(a)

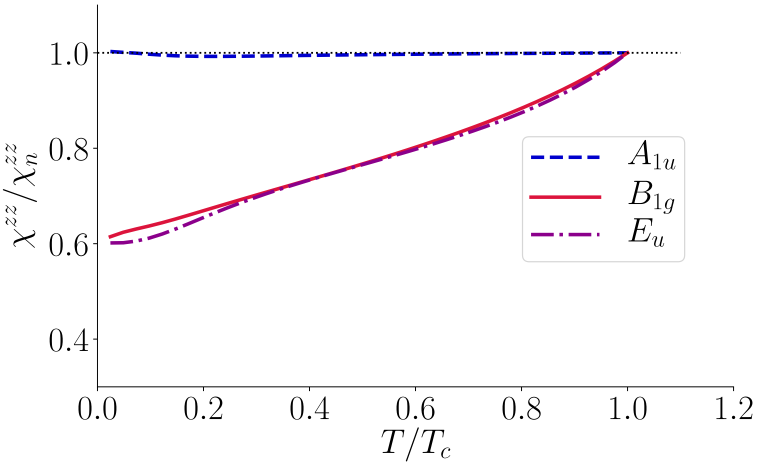

(b)

Figure 3.13: The calculated temperature-dependent spin susceptibility normalised by the normal-state value. Results are shown for the E_u and A_{1u} orders obtained at $J/U = 0.06$, and for the B_{1g} order obtained at $J/U = 0.20$. In (a) the external magnetic field points in the basal plane, and the triangles show the recent experimental data for two different oxygen positions from Ref. [20]. In (b) the magnetic field points out of the basal plane, for which there is not yet published data.

As Fig. 3.13 (b) demonstrates, having the experiment repeated for an out-of-plane magnetic field would offer a crisp distinction between helical p-wave and d-wave order. We consider this a crucial outstanding piece in the long-standing and renewed puzzle of determining the superconducting order in SRO. However, due to the small value of $\mu_0 H_{c2}(T \approx 0.1\text{ K})|_{\boldsymbol{H}\parallel\hat{z}} \approx 60$ mT [147] for out-of-plane fields (cf. $\mu_0 H_{c2}(T \approx 20\text{ mK})|_{\boldsymbol{H}\parallel\hat{x}} \approx 1.2$ T [19]), retrieving the desirable data appears difficult, at least in the unstrained material.

3.6 Concluding Remarks and Outstanding Aspects

3.6.1 Summary

In Sections 3.2 and 3.3 a 3D three-band model for SRO in the weak-coupling limit was proposed. With this model we found, in Section 3.4, a close competition of even- and odd-parity order parameters in the physically interesting range of the interaction parameter J/U. We found an odd-parity helical p-wave (A_{1u}) state to be favoured for Hund's couplings $J/U < 0.15$, and an even-parity d-wave (B_{1g}) state to be favoured for $J/U > 0.15$. Both orders have vertical (near-)nodes, resulting in them being difficult to distinguish via the specific heat, at least for temperatures above a few tens of mK. In the presence of an external magnetic field we calculated the spin susceptibility for the most relevant order parameters. Although the chiral p-wave state was found to clearly conflict with the experiment [19, 20], the helical p-wave and the d-wave orders both appear to be in fairly good agreement with currently available data. However, we pointed to the observation that a successful repetition of the experiment with an out-of-plane magnetic field has the potential of crisply distinguishing between the two cases.

The main and prominent experimental observation that our results appear to starkly conflict with is TRSB [96, 97], an issue that warrants discussion. Below this issue is addressed, with three possible outcomes highlighted.

3.6.2 Possible Outcomes and Outlook

As indicated in Table 2.1 only the two-dimensional representations E_u and E_g would be ensured by the point group symmetries to favour a chiral order parameter with TRSB. Based on the results presented in this chapter, however, both of these sectors appear unlikely to be realised in SRO. An E_u order parameter with $\boldsymbol{d} \parallel \hat{z}$ conflicts with the new NMR experiments [19, 20], and an E_g order parameter appears to be strongly disfavoured microscopically, at least at weak coupling. However, an E_g order parameter was recently shown to be stabilised by inclusion of certain

$\boldsymbol{k}$-dependent SOC terms at orbital level for sufficiently large Hund's coupling[15] J/U [114]. Such an order parameter would possibly be consistent with very recent thermodynamic measurements, suggesting a jump in the shear elastic modulus c_{66} [148, 149]. It would explain evidence of horizontal nodes reported in a specific heat experiment [122] but, however, conflict with indications of vertical line nodes inferred by heat conductivity [103] and STM [144]. One should not dismiss this option, but the overall disfavour of such an order parameter suggests that one should at least explore alternative scenarios.

One can imagine, as proposed in previous work [118, 150, 151], that order parameters from different irreps are nearly degenerate and result in TRSB, as e.g. demonstrated with a quartic order Ginzburg–Landau theory for nearly-degenerate s- and d-wave orders in Ref. [152]. This proposal is potentially supported by the numerical observations of closely competing orders in SRO, both in 2D [116–118], and now in 3D. The unpleasant side of this suggestion is that, in the unstrained material, it would require fine-tuning of parameters to get a near-degeneracy, which would thus be model and method sensitive. However, a very recent μSR study under strain indicates that superconductivity and TRSB indeed onset at slightly different temperatures in the unstrained material [95], potentially supporting the hypothesis of an accidental near-degeneracy. Moreover, these temperatures, T_c and T_{TRSB}, show different dependencies on strain (T_{TRSB} close to no dependence). Relatedly, it was recently hypothesised that if one assumes a near-degeneracy between $d_{x^2-y^2}$ and $g_{xy(x^2-y^2)}$, a substantial body of the experiments can be reconciled [153]. Such a near-degeneracy has not yet been found in any microscopic calculation using a realistic band structure. A phase boundary between d- and g-wave was identified in the 2D extended Hubbard model [154], so the inclusion of longer-range interactions may support the above hypothesis.

---

[15] As proved in Subsection 3.3.2 the two-particle vertex in the Cooper channel is only positive semi-definite for $J/U < 1/3$. For $J/U > 1/3$ the effective interaction becomes attractive and allows for instabilities even at $\mathcal{O}(U)$, something Ref. [114] proposes as a possible scenario. In our model, the leading instability for $J/U > 1/3$ appears as a fully gapped phase in the A_{1g} channel, inconsistent with experiment.

Finally, another possibility is that further experimental results have to be discarded and that evidence of TRSB in SRO might be spurious, unrelated to superconductivity, or require alternative explanations, at least in the bulk [155, 156]. Although microscopic theories for explaining the Kerr experiment (a surface probe) have been developed [157, 158], quantitative estimates remain somewhat difficult to fully reconcile with the experiment [97]. We note that no well-established microscopic theory of TRSB deriving from μSR exists in the literature[16]. In the end, there is a need for combined theoretical and experimental effort in the future to resolve the issue of explaining TRSB in SRO. Andrew P. Mackenzie recently summarised the situation regarding the superconducting order of SRO [159]:

> "*However, it is important that this is all done with cool heads and open minds. The extreme viewpoint of either clinging on to the triplet interpretation or throwing it out of the window without trying to revisit the outstanding mysteries would be equally unhelpful as the field moves forward. It seems to me that the two biggest issues will be establishing whether time reversal symmetry is really broken at T_c, and increasing efforts to perform measurements sensitive to parity.*"

Though there are theoretical options left for an odd-parity order parameter being realised, most of the recent experiments conducted on SRO, when taken in isolation, provide evidence of *d*-wave. This includes NMR [19, 20] and polarised neutron scattering [160], high precision heat capacity [109], heat conductivity [103], ultrasound spectroscopy [148], and quasiparticle interference (STM) directly probing the gap [144].

---

[16] Private communication with Steven H. Simon and Stephen Blundell.

Chapter 4

Majorana Modes in Topological Superconductors

Contents

4.1 Introduction

Throughout the history of condensed matter theory a cornerstone has been to classify all possible phases of a given system. With the advent of the quantum Hall [161] and fractional quantum Hall effect [162] in the 1980s, it was to become evident that such a classification requires, in some instances, knowledge that goes beyond the system symmetries and that is deeply rooted in topology. The connection to topology is more than a mathematical curiosity as it was later understood how *topologically ordered matter* has potential intriguing applications to quantum computing. Below, we present an overview of these ideas before an outline of this chapter is provided.

4.1.1 Topological Superconductivity

As demonstrated in seminal work over the last three decades, gapped Hamiltonians of non-interacting[1] fermions permit a classification of possible topological phases in terms of the presence or absence of three non-spatial symmetries at single-particle level, and the number of spatial dimensions [65, 80, 81, 163].

The three symmetries can be taken to be particle-hole symmetry (PHS) which exchanges the roles of particle (creation) and hole (annihilation) operators, time-reversal symmetry (TRS) which reverses time, and the sublattice or "chiral" symmetry (SLS) which is defined as a product of the two former. The (antiunitary) PHS and TRS can be either absent (denoted by 0), or present and then square to either $+1$ or -1 when implemented as an operator acting on the single-particle Hamiltonian. Combined with the presence (1) or absence (0) of the combined SLS, this results in the classification known as the "tenfold way" in Table 4.1.

Table 4.1: Topological classification of gapped single-particle Hamiltonians of fermions [81]. Here, systems are characterised by the presence (± 1) or absence (0) of time-reversal symmetry (TRS), particle-hole symmetry (PHS), sublattice symmetry (SLS), and by the number of spatial dimensions. The distinct topological phases each class supports is indicated by a topological invariant which in the non-trivial cases takes on either two values, $\mathbb{Z}_2$, or a countable infinity of values, $\mathbb{Z}$ or $2\mathbb{Z}$. Classes D, DIII, C, CI apply to superconducting mean-field systems.

Class	TRS	PHS	SLS	1D	2D	3D
A	0	0	0	–	$\mathbb{Z}$	–
AIII	0	0	1	$\mathbb{Z}$	–	$\mathbb{Z}$
AI	$+1$	0	0	–	–	–
BDI	$+1$	$+1$	1	$\mathbb{Z}$	–	–
D	0	$+1$	0	$\mathbb{Z}_2$	$\mathbb{Z}$	–
DIII	-1	$+1$	1	$\mathbb{Z}_2$	$\mathbb{Z}_2$	$\mathbb{Z}$
AII	-1	0	0	–	$\mathbb{Z}_2$	$\mathbb{Z}_2$
CII	-1	-1	1	$2\mathbb{Z}$	–	$\mathbb{Z}_2$
C	0	-1	0	–	$2\mathbb{Z}$	–
CI	$+1$	-1	1	–	–	$2\mathbb{Z}$

---

[1] Or weakly interacting with respect to the energy scale set by the gap.

In this framework gapped phases of matter are structured into equivalence classes, where the equivalence relation is associated with smooth deformations of Hamiltonians such that the single-particle symmetries are preserved and the gap does not close[2]. Hamiltonians belonging to the same equivalence class are ascribed to the same (topological) phase of matter, labelled by a *topological invariant*.

The three rightmost columns of Table 4.1 indicate whether or not topological phases exist, and in the non-trivial cases which values the topological invariant takes on. The details of calculating the topological invariant depend on both the class and the number of dimensions. Serving as an example, the Chern number of Eq. (2.47) is precisely the integer-valued topological invariant for classes D and C in the 2D case. The predictive power of the invariant is revealed through the *bulk-boundary correspondence*, which relates the topological invariant – a bulk quantity – to the number of gapless excitations localised on boundaries and defects. In certain superconductors these gapless quasiparticle excitations can be non-Abelian anyons, which we introduce properly below.

The classes D, DIII, CI, and C of Table 4.1 are applicable to Bogoliubov–de Gennes (BdG) Hamiltonians and hence to superconductors within a mean-field treatment. Serving as examples encountered in the previous chapters, the ABM phase belongs to class D, and the BW phase to class DIII. Both classes D and DIII, the former breaking and the latter preserving TRS, support topological phases. We denote superconductivity with topologically non-trivial phases by *topological superconductivity* (TSC) in the remainder of this chapter.

4.1.2 Anyons

In the late 1970s it was theoretically appreciated that confining identical particles to two spatial dimensions has fundamental consequences for quantum statistics [25, 26]. This turns out to be very relevant for TSC in 2D. In essence, the topological properties of the configuration space of two identical particles in 2D allows the wavefunction to acquire an arbitrary phase factor, $\exp(i\vartheta)$, when interchanging

---

[2] Caveat: the equivalence classes are also insensitive to the addition or removal of trivial bands. This is called *stable equivalence* [81].

the particle positions. This should be contrasted with 3D where this statistical phase is restricted to either $\vartheta = \pi$ (fermions) or $\vartheta = 0$ (bosons). Quasiparticles with a statistical phase different from 0 and π are called *anyons*, and a system with anyonic quasiparticle excitations will be referred to as *topologically ordered matter* [28]. In a system of N anyons the multi-particle trajectories, that take the set of anyons from some initial positions into the same final positions, are topologically associated with elements of the braid group B_N (in contrast to the permutation group S_N in 3D), as explained further in Subsection 4.4.1. Anyons are either Abelian or non-Abelian [164], determined by whether the representations of the braiding operations commute or not, respectively.

Non-commutativity of the (representation of the) braid group operations gives rise to an intriguing application of non-Abelian anyons: *topological quantum computation*. A quantum computer exploits the superposition principle by coherently acting on states in a Hilbert space. In tasks like prime number factorisation [29], and quantum simulations [30, 31], a quantum computer is, in terms of computation time, expected to outperform a classical computer exponentially in the problem "size". In a topological quantum computer one imagines braiding non-Abelian anyons to accomplish quantum computation in a fashion that by nature is immune to errors, at least in principle. Such immunity to errors is rooted in the non-local properties of the information units made from anyonic quasiparticles (called quantum bits, or qubits in the convenient case of two-level systems). However, the protection relies on having the zero-energy quasiparticles separated from the bulk states by a sizable energy gap (compared to e.g. temperature), which in practice poses a serious challenge.

The anyonic quasiparticles in topological superconductors are known as *Majorana zero modes* (MZMs), named after Ettore Majorana who first demonstrated that the Dirac equation permits a basis of real solutions [165]. In BdG systems MZMs appear as neutral quasiparticles of zero energy localised on domain walls and in isolated vortex cores [21–23, 166]. Majorana zero modes are candidate non-Abelian anyons, with arguably the simplest possible structure. We shall focus on MZMs in 2D systems. In 2D, vortex cores are point-like defects. In this case the bulk-boundary correspondence predicts that both classes D and DIII from Table 4.1 support zero-energy bound states localised in the vortex core [81]. However, only the topologically ordered phase of class D supports a single isolated MZM in the core (for a vortex of vorticity one)[3], which would then be protected by symmetry.

Over the last two decades the quest for realising MZMs in condensed matter systems has intensified [32], mainly due to the potential applicability to topological quantum computation. Candidate systems for realising MZMs have included the fractional quantum Hall Moore–Read Pfaffian state [21, 24, 167], nanowire devices [22, 168–170], quantum anomalous Hall insulators [171], and vortex cores in proximity-induced [172–174] or iron-based superconductors [175–177].

4.1.3 Outline

In a topological superconductor with two isolated vortices the ground state is two-fold degenerate. The two ground states, $\{|0\rangle, |1\rangle\}$, are defined by the presence or absence of a single fermionic mode – a qubit – constructed as a linear combination of the two real MZMs in the Fermi sea. Unitary operations within the ground state manifold, exploiting the non-Abelian properties to manipulate qubit states, is the essence of topological quantum computation[4].

If the two vortices are not isolated but instead separated by a distance comparable to the superconducting coherence length inter-vortex tunneling (hybridisation) lifts the ground state degeneracy, resulting in a two-level system of finite energy difference. Crucially, the hybridisation, and the inter-vortex force derived from this, is sensitive to the qubit state. Hence, as we will explain below, the finitely separated two-vortex system offers an indirect route to reading out the qubit state.

---

[3] In the case of class DIII, in contrast, the Kramers degeneracy owing to TRSI implies Majorana doublets in the vortex core.

[4] An anyonic theory is characterised by its *fusion rules*, which give information about the formation of new anyons when bringing two initial anyons together. For Majorana zero modes σ (also called "Ising anyons"), the crucial fusion rule is $\sigma \times \sigma = 1 + \psi$, where $\times$ is the fusion operator, 1 is the vacuum, and ψ is a fermion [28]. Thus, two Majoranas can fuse to either one or zero fermions. Caveat: if the total number of electrons is fixed, there is a fermion parity constraint, meaning that the fusion channel of two vortices is fixed, see also footnote 7. One would therefore strictly need four vortices to build one qubit.

Qubit read-out is an essential outstanding puzzle in any topological quantum computation protocol [32, 34].

Since the 1960s it has been known that vortex cores in type-II superconductors host a tower of sub-gap states. The low energy sub-gap states are roughly equally-spaced in energy, where the level-spacing is approximately $\delta_\varepsilon \approx \frac{\Delta_0^2}{E_F}$, with Δ_0 the maximal gap and E_F the Fermi energy [36]. In most superconductors $\Delta_0 \ll E_F$, which is believed to severely limit the temperature, $k_B T < \delta_\varepsilon$, to access the MZMs without exciting the sub-gap states.

In this chapter we study MZMs occurring in vortices of a topological superconductor. We review a framework for examining chiral p-wave superconductors, and we calculate basic properties of the low-lying in-gap states in an isolated vortex. Using a statistical mechanical approach, we then study the two-vortex system at finite temperature. We quantify the impact of thermally occupying in-gap states on the hybridisation of two MZMs. Finally, we add value to this consideration by discussing a novel protocol to achieving qubit read-out via the inter-vortex force derived from the hybridisation. The chapter is concluded with a material-oriented outlook.

4.2 A Framework for Topological Superconductivity

Around the beginning of this century Kitaev demonstrated that a 1D chiral p-wave superconducting chain supports localised Majorana zero modes on its boundary [22]. The 1D Kitaev chain represents the simplest example of the paradigm for topological superconductivity, yet it has putative direct applications [178, 179]. A 2D analogue of the model was studied by Volovik [180] and by Read and Green [21]. The latter model is more representative of a number of 2D systems [32, 172, 181].

Instead of aiming to capture the microscopic details of a specific system, we take on a simpler approach by considering the 2D Read–Green model of a chiral p-wave superconductor [21, 180], i.e. class D in the nomenclature of Table 4.1. The reason for this is two-fold. First, our primary focus is to examine the consequences of thermally occupying in-gap states. As such, it is convenient to choose a well-understood model that offers transparency and consistency checks. Second, our goal is not to make accurate system specific predictions, but rather to capture generic features of low-temperature anyonic quasiparticles in topological superconductors. In this section we review the basic properties of the low-lying in-gap states associated with an isolated vortex in the Read–Green model.

4.2.1 The $p + ip$ Model

In the BdG description of a spinless $p{+}ip$ superconductor (i.e. with pairing symmetry $p_x + ip_y$) quasiparticle excitations are fully characterised by the particle-hole spinor $\boldsymbol{\Psi}_n = (u_n,\ v_n)^T$, where particle and hole coefficients are denoted by u_n and v_n, respectively. The quasiparticles are obtained as solutions to the eigenvalue problem $\mathcal{H}\boldsymbol{\Psi}_n = \frac{\varepsilon_n}{2}\boldsymbol{\Psi}_n$, or explicitly [21]

$$\begin{pmatrix} -\frac{1}{2m}\nabla^2 - E_F & \frac{1}{2k_F}\big\{\Delta(\boldsymbol{r}), \partial_x + i\partial_y\big\} \\ -\frac{1}{2k_F}\{\Delta^*(\boldsymbol{r}), \partial_x - i\partial_y\} & \frac{1}{2m}\nabla^2 + E_F \end{pmatrix} \begin{pmatrix} u_n(\boldsymbol{r}) \\ v_n(\boldsymbol{r}) \end{pmatrix} = \frac{\varepsilon_n}{2} \begin{pmatrix} u_n(\boldsymbol{r}) \\ v_n(\boldsymbol{r}) \end{pmatrix}, \tag{4.1}$$

where m is the effective electron mass, k_F (E_F) is the Fermi momentum (energy), $\Delta(\boldsymbol{r})$ is the superconducting pairing potential, and ε_n is the n'th energy level. The factor of $\frac{1}{2}$ in the energies is introduced to make ε_n the energy difference between particle and hole excitations around the Fermi sea. This is convenient since the BdG Hamiltonian of Eq. (4.1) exhibits a particle-hole symmetry $\{\mathcal{H},\ \Xi\} = 0$, with $\Xi = \tau_x\kappa$, where τ_x is a Pauli matrix acting on the particle-hole spinor and κ is the complex conjugation operator. This operator relates quasiparticle and quasihole excitations according to

$$\Xi\boldsymbol{\Psi}_n = \boldsymbol{\Psi}^*_{-n}, \tag{4.2}$$

where the index n refers to a solution of energy $+\varepsilon_n/2$ and $-n$ to a solution of energy $-\varepsilon_n/2$, thus enforcing the spectrum to be symmetric around the Fermi energy. The quasiparticle (annihilation) operators are superpositions of electrons and holes, with weights determined by the coefficients appearing above,

$$\gamma_n = \int \mathrm{d}\boldsymbol{r}\left[u^*_n(\boldsymbol{r})c(\boldsymbol{r}) + v^*_n(\boldsymbol{r})c^\dagger(\boldsymbol{r})\right], \tag{4.3}$$

where $c(\boldsymbol{r})$ annihilates a spinless electron at position $\boldsymbol{r}$. The quasiparticles satisfy the fermionic commutation relations

$$\{\gamma_n,\, \gamma_m^\dagger\} = \delta_{nm}. \tag{4.4}$$

For this to be consistent with Eq. (4.3) the orthogonality condition

$$\int \mathrm{d}\boldsymbol{r} \left[u_n^*(\boldsymbol{r}) u_m(\boldsymbol{r}) + v_n^*(\boldsymbol{r}) v_m(\boldsymbol{r})\right] = \delta_{nm} \tag{4.5}$$

is imposed. For $n = m$ this relation fixes normalisation.

4.2.2 Majorana Zero Modes

In the special case of a zero-energy mode, the particle-hole operator transforms $\boldsymbol{\Psi}_0$ onto itself according to Eq. (4.2), which means that

$$\Xi \boldsymbol{\Psi}_0 = \boldsymbol{\Psi}_0^* \quad \Rightarrow \quad u_0(\boldsymbol{r}) = v_0^*(\boldsymbol{r}). \tag{4.6}$$

It is convenient to redefine the normalisation for zero modes,

$$\{\gamma_n,\, \gamma_m\} = 2\delta_{nm}, \tag{4.7}$$

such that $\gamma_n^2 = 1$, and $\int \mathrm{d}\boldsymbol{r}\, |u_0(\boldsymbol{r})|^2 = 1$. In this case the BdG equations can be solved exactly in the presence of a vorticity-ℓ vortex for which $\Delta(\boldsymbol{r}) = \Delta_0 f(r) e^{i\ell\theta}$. Here, $f(r)$ is the (real) radial profile of the vortex such that $\lim_{r\to\infty} f(r) = 1$, and θ is the polar angle. The BdG equations decouple and become redundant; they turn into the single complex differential equation

$$\frac{1}{2m}\left(\nabla^2 + E_F\right) u_0(\boldsymbol{r}) + \frac{\Delta_0}{k_F}\sqrt{f(r)}\, e^{i\theta(\ell/2+1)} \left(\frac{\partial}{\partial r} + \frac{i}{r}\frac{\partial}{\partial \theta}\right)\left[\sqrt{f(r)}\, e^{i\theta\ell/2} u_0^*(\boldsymbol{r})\right] = 0. \tag{4.8}$$

Only for odd ℓ does this equation exhibit a robust (independent of the details of f) zero-energy solution [166]. For odd ℓ one can take $u_0(\boldsymbol{r}) = e^{i\theta(\ell+1)/2} u_0(r)$ to make the remaining equation for $u_0(r)$ real. By further assuming $f(r) = \tanh(r/\xi)$ to be a reasonable description of the singly quantised vortex $\ell = 1$ [58], one arrives at the following expression for the particle-hole-spinor of the MZM:

$$\boldsymbol{\Psi}_0(\boldsymbol{r}) = \begin{pmatrix} u_0(\boldsymbol{r}) \\ v_0(\boldsymbol{r}) \end{pmatrix} = \mathcal{N} \frac{J_1\left(r\sqrt{2mE_F - 1/\xi^2}\right)}{\cosh(r/\xi)} \begin{pmatrix} ie^{i\theta} \\ -ie^{-i\theta} \end{pmatrix}, \tag{4.9}$$

where $\mathcal{N}$ is a normalisation constant, and J_1 is a Bessel function of the first kind. Above, $\xi = v_F/\Delta_0$, with v_F being the Fermi velocity, is the *superconducting coherence length.*

In the case of N vortices at positions $\{\boldsymbol{R}_j\}_{j=1}^{N}$ one can, in the same fashion, make the heuristic multi-vortex approximation for the order parameter

$$\Delta(\boldsymbol{r}) = \Delta_0 \prod_{j=1}^{N} f(|\boldsymbol{r} - \boldsymbol{R}_j|) e^{i \arg(\boldsymbol{r}-\boldsymbol{R}_j)}. \tag{4.10}$$

This approximation is expected to break down if the inter-vortex distance is small compared to ξ.

4.2.3 Excited Sub-Gap States

In seminal work Caroli, de Gennes, and Matricon (CdGM) derived expressions for vortex-bound states in a type-II superconductor [36]. The main result of this work is the presence of a tower of equally-spaced energy levels (Fig. 4.1), with an energy spacing of roughly

$$\delta_\varepsilon \approx \frac{\Delta_0^2}{E_F}, \tag{4.11}$$

where Δ_0 is the full gap and E_F is the Fermi energy. The quantity δ_ε is called the *minigap*, see Fig. 4.1. The in-gap states, which are commonly denoted by CdGM states, are bound states exponentially localised over the scale of ξ near

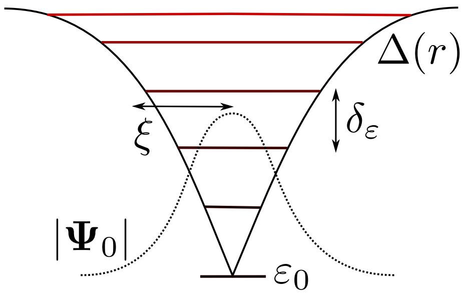

Figure 4.1: Cartoon of the vortex core profile $\Delta(r) = |\Delta(\boldsymbol{r})|$ and the sub-gap CdGM levels of a singly quantised vortex. The low-lying CdGM states are characterised by an energy spacing of δ_ε, called the minigap, above the ground state. The ground state has a particle-hole spinor $\boldsymbol{\Psi}_0$ and energy level ε_0, and the bound states are localised in the vortex core over the scale of the coherence length ξ.

the vortex core. In p-wave superconductors the CdGM states in single-vortex systems have been extensively characterised [182–184]. For an odd-ℓ vortex, with $\Delta(\boldsymbol{r}) = \Delta_0 f(r) e^{i\ell\theta}$, the CdGM energy levels are given by

$$\varepsilon_m = m\delta_\varepsilon, \tag{4.12}$$

where $m \in \mathbb{Z}$. The minigap can be approximately obtained by following the procedure demonstrated by CdGM. Their procedure amounts to assuming a simplified gap profile. In particular, one may solve the BdG equations formally for the two cases $f(r \to 0) = 0$ (vortex core) and $f(r \gg |\ell| k_F^{-1}) = 1$ (making use of the asymptotic forms of Bessel functions), and match the two solutions at some "core radius" $r = r_c$ [36, 183], which results in

$$\delta_\varepsilon \approx \frac{2m\Delta_0^2}{k_F^2} \frac{\int_0^\infty \mathrm{d}\rho\, f(\rho\xi)/\rho \exp\bigl(-2\int_0^\rho \mathrm{d}\rho'\, f(\rho'\xi)\bigr)}{\int_0^\infty \mathrm{d}\rho\, \exp\bigl(-2\int_0^\rho \mathrm{d}\rho'\, f(\rho'\xi)\bigr)}, \tag{4.13}$$

where $\rho = r/\xi$ is dimensionless length, and where we emphasise that $f(\rho)$ depends on ℓ, crucially such that the asymptotic behaviour $f(\rho) \sim \rho^{|\ell|}$ as $\rho \to 0$ is recovered[5]. In the case of a singly quantised vortex, as described in the preceding subsection, Eq. (4.13) evaluates to

$$\delta_\varepsilon \approx \frac{7\zeta(3)}{\pi^2} \frac{\Delta_0^2}{E_F}, \tag{4.14}$$

where ζ is the Riemann zeta function.

4.3 The Two-Vortex System at Finite Temperature

To exploit the MZMs in isolated vortex cores, it is commonly believed that the temperature should be minimised as far as possible to avoid thermal activation of the in-gap (CdGM) states. In most of the known material candidates, however, this poses a rather pessimistic outlook since $\Delta_0 \ll E_F$ typically. In Sr_2RuO_4, for instance, $\Delta_0 \approx 10^{-3} E_F \approx 4$ K, which presumably makes vortex cores swamped

---

[5] This behavior is expected from the non-linear Schrödinger equation $\frac{\mathrm{d}^2 f}{\mathrm{d}\rho^2} + \frac{1}{\rho}\frac{\mathrm{d}f}{\mathrm{d}\rho} + (1 + \frac{\ell^2}{\rho^2}) f = f^3$, which has the small-$\rho$ (hence small-f) solutions $J_\ell(\rho) \sim \rho^{|\ell|}$.

with in-gap states. However, novel iron-based superconductors have Δ_0 on the order of the Fermi energy, drastically improving this issue, as will be discussed towards the end of this chapter.

With respect to the prospects of measuring the Majorana qubit state, it is useful to revisit the role of the CdGM sub-gap states, in particular at non-negligible temperatures compared to the gap. In this section, we do so using a statistical mechanical approach in a minimal two-vortex $p + ip$ system. The two Majorana modes localised in the two vortex cores define a single qubit. As we will show, the qubit state is reflected in the inter-vortex hybridisation – and in the inter-vortex force derived from this – when the distance between the two vortices is finite. This offers a route to achieve read-out of the qubit as discussed in Section 4.4. Below we shall define the *parity contrast* as a key quantity reflecting the feasibility of achieving read-out. The parity contrast is studied both numerically and analytically, with asymptotically exact results extracted in the low-temperature limit.

4.3.1 Restricted Grand Canonical Ensemble

In a particle-hole symmetric spectrum with energy levels $\pm\varepsilon_n/2$ and chemical potential $\mu = 0$, the grand canonical partition function takes the standard form

$$\mathcal{Z}_0 = \prod_n 2\cosh\left(\beta\varepsilon_n/2\right), \tag{4.15}$$

where the product runs over n such that $\varepsilon_n \geqslant 0$, and where $\beta = 1/(k_B T)$. Since the fermion number modulo 2 is conserved in a superconductor, we project the partition function onto the two sectors of even ($P = +1$) and odd ($P = -1$) fermionic parity [185–187]:

$$\begin{aligned} \mathcal{Z}_\pm &= \frac{1}{2}\prod_n e^{\beta\varepsilon_n/2}\Big[\prod_m (1 + e^{-\beta\varepsilon_m}) \pm \prod_l (1 - e^{-\beta\varepsilon_l})\Big] \\ &= \frac{1}{2}\mathcal{Z}_0\Big[1 \pm \prod_m \tanh\left(\beta\varepsilon_m/2\right)\Big]. \end{aligned} \tag{4.16}$$

To see explicitly that this construction works, consider a system with three (positive) energy levels $\{\varepsilon_i/2\}_{i=0}^{2}$. Truncating the spectrum like this is a reasonable approximation to the two-vortex system in the low-temperature limit. If $\beta^{-1} \ll \varepsilon_2$

the states involving occupancy of higher levels are suppressed by Boltzmann factors and can be ignored. From Eq. (4.16) we have

$$\mathcal{Z}_+ = e^{\frac{\beta}{2}(\varepsilon_0+\varepsilon_1+\varepsilon_2)} + e^{\frac{\beta}{2}(-\varepsilon_0-\varepsilon_1+\varepsilon_2)} + e^{\frac{\beta}{2}(-\varepsilon_0+\varepsilon_1-\varepsilon_2)} + e^{\frac{\beta}{2}(\varepsilon_0-\varepsilon_1-\varepsilon_2)}, \tag{4.17}$$

$$\mathcal{Z}_- = e^{\frac{\beta}{2}(-\varepsilon_0+\varepsilon_1+\varepsilon_2)} + e^{\frac{\beta}{2}(\varepsilon_0-\varepsilon_1+\varepsilon_2)} + e^{\frac{\beta}{2}(\varepsilon_0+\varepsilon_1-\varepsilon_2)} + e^{\frac{\beta}{2}(-\varepsilon_0-\varepsilon_1-\varepsilon_2)}. \tag{4.18}$$

The occupancy configurations involved in $\mathcal{Z}_\pm$ are shown pictorially in Fig. 4.2, in which each occupied quasiparticle (quasihole) level is marked with a coloured dot above (below) the Fermi sea. The occupancy configurations have an even (odd) number of occupied quasiparticle levels in parity sector $P = +1$ ($P = -1$).

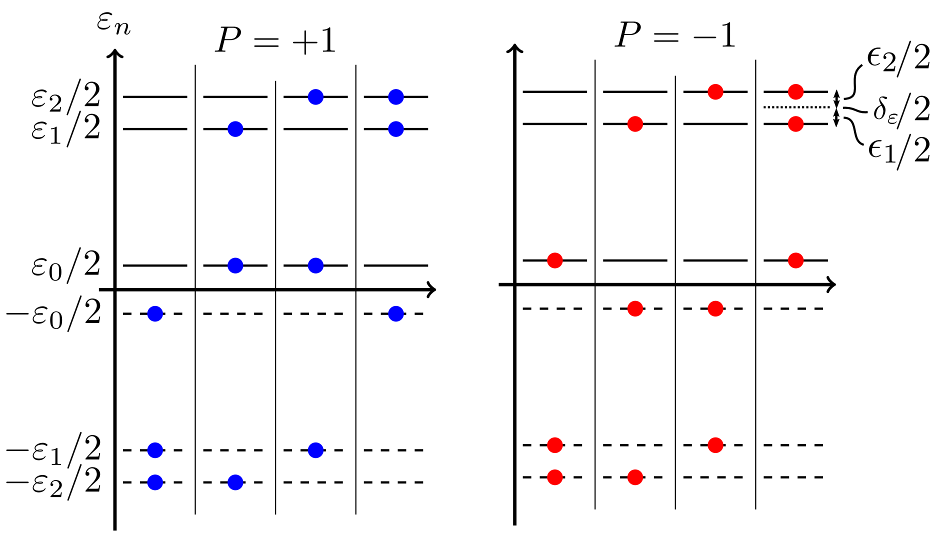

(a) (b)

Figure 4.2: Occupancy configurations in the two parity sectors $P = \pm 1$ for a truncated-level system. Coloured dots above the Fermi sea indicate the occupation of a quasiparticle level. (a) $P = +1$: even number of quasiparticle excitations, (b) $P = -1$: odd number of quasiparticle excitations. The labels in the upper right indicate the minigap δ_ε and deviations from the minigap ϵ_i, defined in Eq. (4.21), caused by inter-vortex hybridisation.

We define the free energy in the two parity sectors as

$$F_\pm = -\frac{1}{\beta} \ln \mathcal{Z}_\pm. \tag{4.19}$$

Serving as a measure of the contrast between the two parity sectors at finite temperature, the *parity contrast* is defined as the difference

$$\Delta F \equiv F_- - F_+ = \frac{1}{\beta} \ln \left(\frac{\mathcal{Z}_+}{\mathcal{Z}_-} \right). \tag{4.20}$$

As motivated in the beginning of this section, the parity contrast reflects the parity-dependent contribution to the inter-vortex hybridisation. It incorporates the effect of thermal scrambling from in-gap states, thereby quantifying how quantum information is hidden at finite temperature [188]. We are interested in measurable consequences deriving from the parity contrast [170]. In particular, the derivative of Eq. (4.20) with respect to the inter-vortex separation yields the parity-dependent inter-vortex force contribution, which can be measured [189]. We elaborate on practical aspects of how to achieve read-out in reality, which to a great extent is an unresolved problem [34], in Section 4.4. For now we will think of the parity contrast as a measure of the possibility of probing the Majorana qubit state.

4.3.2 Effective Low-Temperature Model

We pursue the effective model of Eqs. (4.17) and (4.18). As merely a convenient change of notation, we define

$$\varepsilon_1 \equiv \delta_\varepsilon - \epsilon_1, \quad \text{and} \quad \varepsilon_2 \equiv \delta_\varepsilon + \epsilon_2, \tag{4.21}$$

where the ϵ_i's are (small) deviations from the minigap δ_ε, see Fig. 4.2. This notation is motivated by the numerical results of Subsection 4.3.4, in which it is established how the two-vortex levels hybridise at finite inter-vortex separation. The small deviations are expected to decay like $\epsilon_i \propto \exp(-R/\xi)$, where R is the inter-vortex distance. Using this notation Eqs. (4.17) and (4.18) are recast as

$$\mathcal{Z}_\pm = 2\exp(\pm\beta\varepsilon_0/2)\left[\exp(\mp\beta\varepsilon_0)\cosh\left(\beta\frac{\epsilon_1+\epsilon_2}{2}\right) + \cosh\left(\beta\left[\delta_\varepsilon + \frac{\epsilon_2-\epsilon_1}{2}\right]\right)\right], \tag{4.22}$$

and the parity contrast becomes

$$\Delta F = \varepsilon_0 + \frac{1}{\beta}\ln\frac{\exp(-\beta\varepsilon_0)\cosh\left(\beta\frac{\epsilon_1+\epsilon_2}{2}\right) + \cosh\left(\beta[\delta_\varepsilon + \frac{\epsilon_2-\epsilon_1}{2}]\right)}{\exp(+\beta\varepsilon_0)\cosh\left(\beta\frac{\epsilon_1+\epsilon_2}{2}\right) + \cosh\left(\beta[\delta_\varepsilon + \frac{\epsilon_2-\epsilon_1}{2}]\right)}. \tag{4.23}$$

Here, the zero-temperature result $\Delta F(T=0)$ appears as the first term, and the non-analytic finite-temperature correction is given by the second term. This correction is always negative (in the physical range for the parameters involved), reflecting that thermal activation of the excited states is exclusively destructive in terms of having a large parity contrast (cf. Ref. [170]). For temperatures below the minigap, $\beta\delta_\varepsilon \gg 1$, the above expression takes on the approximate form

$$\Delta F \approx \varepsilon_0 - \frac{4}{\beta}\cosh\big(\beta\frac{\epsilon_1+\epsilon_2}{2}\big)\sinh(\beta\varepsilon_0)\exp\big(-\beta(\delta_\varepsilon+[\epsilon_2-\epsilon_1]/2)\big), \tag{4.24}$$

which shows explicitly the thermal suppression factor $\exp(-\beta\delta_\varepsilon)$. It deserves commenting that although thermal activation of the CdGM states reduces the parity contrast and hence hides quantum information, the global fermion parity is perfectly conserved at finite temperature as long as the Majoranas do not interact with each other nor with the CdGM states [188].

4.3.3 The Thermodynamic Limit

To treat temperatures above the minigap rigorously, consider next an arbitrary number of vortex core states (leaving the truncated-level system). The parity contrast of Eq. (4.20) then takes the form

$$\Delta F = \frac{1}{\beta}\ln\frac{1+\prod_m \tanh(\beta\varepsilon_m/2)}{1-\prod_n \tanh(\beta\varepsilon_n/2)}. \tag{4.25}$$

In the two-vortex system at infinite inter-vortex distance, there is no hybridisation, and the system has two copies of the single-vortex CdGM levels along with one fermionic zero-energy level constituted by the two MZMs. When the two vortices are separated by a finite distance, the single-vortex levels are expected to hybridise. It is therefore reasonable to label the CdGM levels such that

$$\varepsilon_0 < \varepsilon_1 \leqslant \varepsilon_2 < \varepsilon_3 \leqslant \varepsilon_4 < \ldots, \tag{4.26}$$

where "$\leqslant$" becomes "$=$" in the infinite-separation limit. If the temperature is well above at least one of the sub-gap levels $\varepsilon_n \ll \beta^{-1} \ll \Delta_0$, we can approximate $\tanh(\beta\varepsilon_m/2) \approx \beta\varepsilon_m/2\ \forall m \leqslant n$. This results in the approximate parity contrast

$$\Delta F \approx \varepsilon_0(\beta/2)^n \prod_{m=1}^{n}\varepsilon_m \prod_{l=n+1}^{\infty}\tanh(\beta\varepsilon_l/2). \tag{4.27}$$

Here, the string of tanh's will be reasonably close to unity since $\beta\varepsilon_l > 1$ for $l \geqslant n+1$ by assumption. When simply replacing the string by 1, the parity contrast has the simple approximate temperature-dependence $\Delta F \sim T^{-n}$, where n is the number of occupied CdGM levels on average (not including ε_0). How good of an approximation this is will be quantified in Subsection 4.3.4.

The above treatment can be justified in cases where there is a sizable minigap so that the temperature can be resolved on a finer scale than the minigap. This is likely the case in several novel iron-based putative (surface-)TSCs [175], which we elaborate on in Subsection 4.4.2. However, in most known cases, Δ_0 is orders of magnitude smaller than E_F, making the minigap tiny and the vortex cores swamped with in-gap states. This is for instance the situation in most proximity-induced topological superconductors [174], and in recently reported superconducting Pb monolayers [190]. In this latter situation we instead consider a continuum version of Eq. (4.25) [170] by introducing $\rho_0 \equiv 1/\delta_\varepsilon$ as a density of states in the vortex core. The parity contrast now becomes

$$\begin{aligned}\Delta F = \frac{1}{\beta} \ln\coth\Big(\frac{1}{2}\ln\coth(\beta\varepsilon_0/2) + \frac{1}{2}\int_{\delta_\varepsilon}^{\infty} \mathrm{d}E\,\rho_0 \ln\coth(\beta E/2) \\ + \frac{1}{4}\ln\coth(\beta\delta_\varepsilon/2)\Big).\end{aligned} \tag{4.28}$$

The term on the second line above appears when the sum of evenly-spaced levels is replaced by a trapezoidal rule integral. To recast this expression into something more useful, we employ

$$\begin{aligned}h(x) &= \int_x^{\infty} \mathrm{d}y \ln\coth y \\ &= \frac{\pi^2}{24} + \frac{1}{2}\big[\ln\tanh x \ln(1+\tanh x) + \mathrm{Li}_2(1-\tanh x) + \mathrm{Li}_2(-\tanh x)\big] \\ &= \frac{\pi^2}{8} + x(\ln x - 1) + \mathcal{O}(x^3),\end{aligned} \tag{4.29}$$

where $\mathrm{Li}_2(x) = -\int_0^x \mathrm{d}u\, \frac{\ln(1-u)}{u}$ is the dilogarithm function. Using Eq. (4.29) in Eq. (4.28) we arrive at

$$\Delta F = \varepsilon_0\sqrt{2\rho_0 k_B T}\exp\left(-\frac{\pi^2}{4}\rho_0 k_B T\right)\exp\left(1+\mathcal{O}([\rho_0 k_B T]^{-2})\right), \tag{4.30}$$

where it is still assumed that $k_B T \ll \Delta_0$. The exponential suppression in $\rho_0 k_B T$ strongly suggests that it will most likely not be possible to resolve the parity contrast at realistic temperatures in the context of small minigaps. Therefore, Eq. (4.30) goes to the core of what is mainly a material issue, namely to engineer clean topological superconductors with Δ_0 on the order of E_F.

4.3.4 Inter-Vortex Hybridisation

It is desirable to solve the BdG equations of Eq. (4.1) numerically as a function of the inter-vortex distance $R = |\boldsymbol{R}_1 - \boldsymbol{R}_2|$, using the multi-vortex ansatz of Eq. (4.10). We consider the dimensionless parameters $E_F = 3$, $\Delta_0 = 1$, and $mk_F^2 = 54$. These parameters are not chosen to accurately describe a specific system, but rather to produce a number of sub-gap states reminiscent of that found in iron-based compounds [177, 191]. The BdG equations are solved by discretisation on an open slab of size no smaller than $20\xi \times 18\xi$ with Dirichlet boundary conditions.

From the CdGM approximation of Eq. (4.14) one expects low-lying levels at integer multiples of roughly $\frac{\delta_\varepsilon}{2\Delta_0} \approx \frac{7\zeta(3)}{6\pi^2} \approx 0.1421$ when $R \gg \xi$. The first sub-gap energy levels as a function of R/ξ are displayed in Fig. 4.3, with the lower panel showing colour maps of $|\boldsymbol{\Psi}_n(\boldsymbol{r})| = (|u_n(\boldsymbol{r})|^2 + |v_n(\boldsymbol{r})|^2)^{1/2}$ for the three lowest-lying states. At large vortex-vortex distances the CdGM level estimates are seen to agree reasonably well with numerics, despite $\Delta_0 \ll E_F$ not being satisfied. In the limit $R \gg \xi$ we expectedly recover doubly degenerate CdGM levels as formed by two copies of the single-vortex system. In the same limit, the two vortices each host a MZM – with associated quasiparticle operators denoted by γ_1 and γ_2 – which combine into a single fermionic mode, $\gamma_1 + i\gamma_2$, of zero energy. This fermionic mode is the topological qubit.

For smaller separations the levels are clearly seen to hybridise, and the hybridisation exhibits oscillations in R/ξ. These features resemble the result of the technical ground state overlap calculation reported in Refs. [82, 192]:

$$\varepsilon_\pm \approx \mp \frac{4\Delta_0}{\pi^{3/2}} \frac{\cos\left(k_F R + \frac{\pi}{4}\right)}{\sqrt{k_F R}} \exp(-R/\xi), \tag{4.31}$$

strictly valid when $R \gg \xi$ and $k_F\xi \ll 1$. The energies $\varepsilon_\pm$ are related to ε_0 appearing in the above section as $\varepsilon_0 = \varepsilon_+ - \varepsilon_-$. The notation suggests that the occupancy of

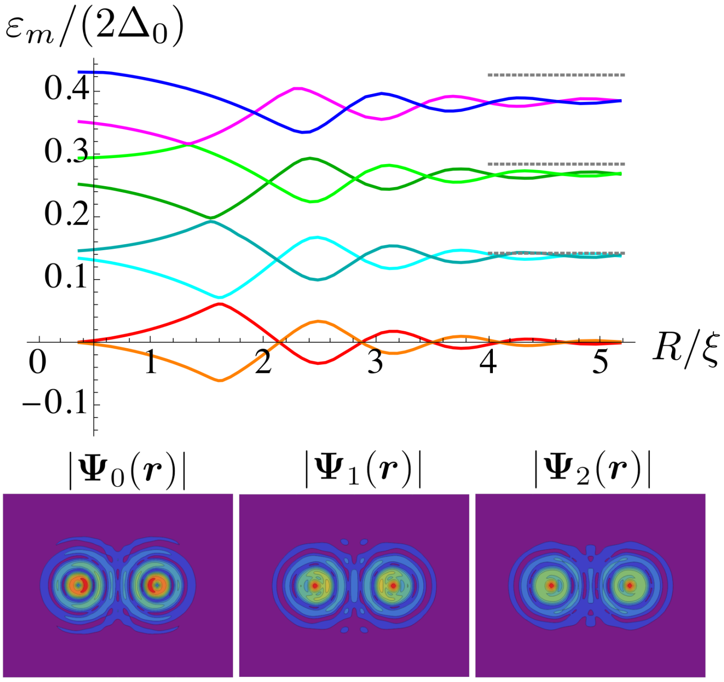

Figure 4.3: The first energy levels of the two vortex system, normalised by the asymptotic gap, as a function of the inter-vortex distance. The gray dotted lines show the result expected from the CdGM formula of Eq. (4.13), in the limit $R/\xi \to \infty$. The lower panels display colour maps of the three lowest-lying states for $R/\xi = 3.0$ on a slab of size $8\xi \times 6\xi$.

the qubit $n = 0, 1$ corresponds to parity $P = +, -$, respectively. For completeness, we outline the steps of a similar overlap calculation in Appendix B on an annulus geometry. The oscillations of the excited CdGM states numerically appear to be slightly shifted. These shifts are reminiscent of the shift associated with the Bessel functions (cf. Eq. (4.9)), of which argument increase with the energy, appearing in the wavefunctions of the single-vortex solutions [183]. The small-argument behaviour of the Bessel functions is indeed confirmed close to the vortex core, as shown in the lower panel of Fig. 4.3.

A caveat with the open geometry considered here is the presence of boundary states. These boundary states are induced by the positive circulation of the two vortices, and they are subject to an energy spacing set by v_F/L, where L is the length of the sample boundary. One way to get rid of the boundary states completely is to instead solve the system on a closed geometry and reverse the circulation of one vortex (i.e. replace one vortex by an anti-vortex) [21, 182]. Note, however, that this is physically different from the vortex-vortex system. On a spherical geometry, with the vortex and the anti-vortex placed on antipodal points, the spatial oscillations of the energy levels, for instance, disappear [182].

One might worry that the boundary states could depend on the inter-vortex distance with oscillations similar to the vortex-bound states. Such a dependence could cause the background energy, appearing as $-\frac{1}{2}\sum_n \varepsilon_n$ when diagonalising the BdG Hamiltonian, to conspire against the oscillations seen in Fig. (4.3). Fortunately, so long as the edge is far from the vortices (compared to ξ), we checked that this background energy[6] does not exhibit oscillations, and that the ground state level oscillations are clearly visible on top of this background. In fact, the background energy displays a $\ln(R/\xi)$ dependence, which is assigned to the expected contribution from the mutual Lorentz repulsion [58]. In the case of a vortex-anti-vortex pair, the same background arises but with a negative prefactor, reflecting mutual attraction in this case.

In Figs. 4.4 and 4.5 we show the impact of temperature on the free energy and the parity contrast, as elaborated on in theory in Subsection 4.3.1. In Fig. 4.4

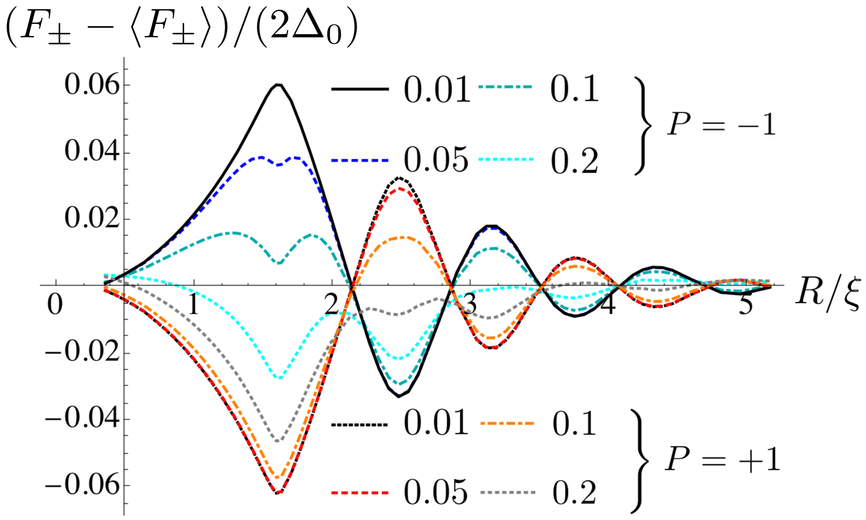

Figure 4.4: The parity-restricted free energy $F_{P=\pm}$ as a function of inter-vortex separation R. Line labels refer to the value of $k_B T/(2\Delta_0)$. For clarity, the free energy averaged over R, denoted by $\langle F_\pm \rangle$, has been subtracted off. Note that the zero-temperature limit yields $\pm\varepsilon_0/(2\Delta_0)$ as shown in Fig. 4.3.

---

[6] With the sum restricted to the first 150 energies.

the free energy from Eq. (4.16) is evaluated numerically for several values of the temperature, with the line labels giving the value of $k_BT/(2\Delta_0)$ in the two parity channels. To make the comparison to the low-temperature limit easier, the free energy averaged over R, denoted by $\langle F_\pm \rangle$, was subtracted off in the figure. A non-trivial smearing of the levels becomes evident roughly as k_BT surpasses the energy of the first excited state. For temperatures close to the second CdGM level the oscillations of $F_\pm$ become less clear and the period distorted.

For a quantitative evaluation of the parity contrast as a function of temperature, see Fig. 4.5. Here, the parity contrast at $R/\xi = 3$ normalised by the zero-temperature

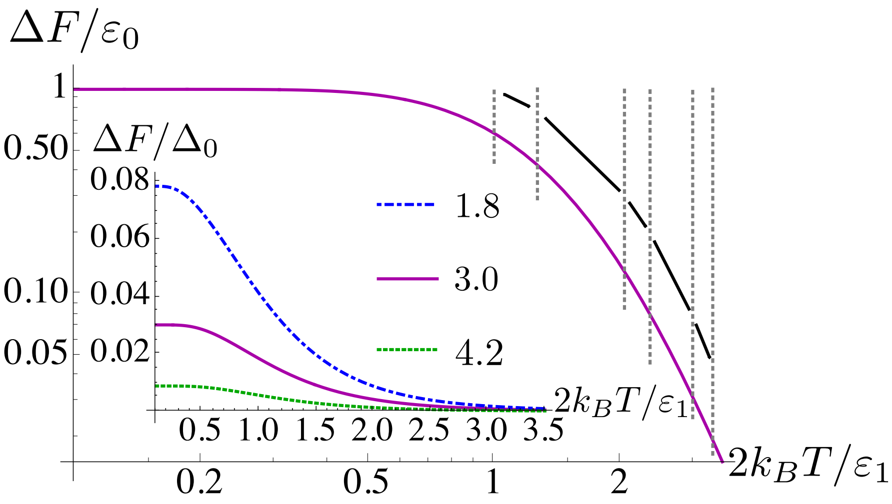

Figure 4.5: The parity contrast ΔF at $R/\xi = 3$ normalised by the lowest-lying level as a function of temperature normalised by the first excited level, on a log-log scale. The gray dotted lines indicate the CdGM levels (cf. Fig. 4.3), and the broken black lines show the rough estimate $\Delta F \approx \varepsilon_0 (\beta/2)^n \prod_{m=1}^{n} \varepsilon_m$, see Eq. (4.27). The inset shows the parity contrast with linear axes for three values of R/ξ as described by the labels.

result is shown as a function of temperature normalised by the first excited level on a log-log scale. The inset shows the same function (but normalised instead by the full gap Δ_0) with linear axes, and for three different values of R/ξ (given in the labels). In the main frame the CdGM levels with gray dashed lines are also shown (cf. Fig. 4.3 at $R/\xi = 3$). Moreover, the full black lines show the simple prediction of Eq. (4.27), $\Delta F \approx \varepsilon_0 (\beta/2)^n \prod_{m=1}^{n} \varepsilon_m$, when replacing $\tanh(\beta\varepsilon_l/2)$ by 1 for all $l > n$. Though this simple approximation is off by a factor of around 2, it essentially captures the trend of the curve.

Having shown how the parity contrast reduces as excited states are thermally activated, we now turn to how one in principle might probe a read-out of the qubit and the practical limitations to overcome in order to achieve this goal.

4.4 Aspects of Qubit Read-Out

In the preceding section the vortex-vortex hybridisation at finite temperature was examined. We focused on the free energy difference between the two parity sectors, dubbed the parity contrast.

In this section, we will demonstrate how this quantity can prove useful in reading out the state of the Majorana qubit. All protocols for Majorana based quantum computation rely on read-out of the qubit state. The importance of this step should not be underestimated, and it can be considered one of the major challenges to overcome in order to achieve topological quantum computation in practice [32, 34]. First, we review the non-Abelian properties of MZMs. Then, we propose an idealised read-out protocol. In relation to the proposed protocol, possible practical limitations are discussed, such as ways of controlling vortices and *quasiparticle poisoning*, where the latter poses a leading threat to successful quantum computation with Majorana modes.

4.4.1 Braiding

The particular algebra of Eq. (4.7), defined by Eq. (4.3), in a spin triplet superconductor in $2+1$ dimensions has fundamental implications for quantum statistics, as demonstrated by Ivanov [23] and reviewed in Refs. [28, 32]. Here, we state how this algebra gives rise to non-Abelian statistics.

In a system of $2N$ isolated vortices, each carrying a MZM in the vortex core, the ground state is 2^N-fold degenerate[7]. We are interested in adiabatic swapping of vortex positions when the vortices are well-separated compared to the coherence length. Here, "adiabatic" refers to slow motion compared to the time scale set by the energy gap $\hbar/\Delta_0$. We discuss further motion constraints in Subsection 4.4.2.

---

[7] Technically, the ground state manifold is partitioned into two 2^{N-1}-fold degenerate sectors, each with well-defined fermionic parity, as explained in Subsection 4.3.1.

By “swapping of vortex positions” we mean spatial exchange of vortices such that the initial set of vortex positions is mapped onto itself. Such an exchange can always be encoded through a sequence of pairwise exchanges of neighboring vortices. A key insight provided by Ivanov is that the pairwise exchange of vortices is a projective[8] representation of the braid group B_{2N} [23]. There are $2N-1$ generators of the braid group B_{2N}, denoted by $\{\sigma_i\}_{i=1}^{2N-1}$, which are defined to encode the clockwise exchange of a pair of two neighbouring vortices such that the path does not enclose any other than the two being exchanged. These braid group generators satisfy the defining relations

$$\sigma_i\sigma_j = \sigma_j\sigma_i \quad \text{for} \quad |i-j| \geqslant 2, \tag{4.32}$$

$$\sigma_i\sigma_{i+1}\sigma_i = \sigma_{i+1}\sigma_i\sigma_{i+1}. \tag{4.33}$$

A representation of these generators, satisfying $\sigma_i(\gamma_j) = U_i\gamma_j U_i^\dagger$, relevant for how the MZMs braid was pointed out by Ivanov [23]:

$$U_i = \exp\left(\frac{\pi}{4}\gamma_{i+1}\gamma_i\right) = \frac{1}{\sqrt{2}}\left(1 + \gamma_{i+1}\gamma_i\right). \tag{4.34}$$

These unitary operators are clearly non-commuting, and so they give rise to non-Abelian statistics, making MZMs candidate non-Abelian anyons. Unfortunately, the unitary braiding operators alone are not enough to span a gate set allowing universal quantum computation [28]. However, the non-topological addition needed to achieve universal quantum computation can in principle be implemented with promisingly high error thresholds [193].

In addition to a non-topological gate required to achieve universal quantum computation with Majorana modes, a read-out scheme for Majorana qubits is required. Here, we sketch an idealised read-out protocol. Consider a topological superconductor (TSC) harbouring a stationary or pinned vortex (A), and a mobile vortex (M), each hosting a MZM. If A and M are well-separated, one can approximate the ground states by the even (+) and odd (−) parity particle-hole spinors [82, 192]

$$\boldsymbol{\Psi}_\pm = \frac{1}{\sqrt{2}}(\boldsymbol{\Psi}_\mathrm{A} \pm i\boldsymbol{\Psi}_\mathrm{M}), \tag{4.35}$$

---

[8] By “projective” we mean up to an overall Abelian phase factor originating from the time-evolution.

where the relative phase factor is fixed by the particle-hole operator, $\boldsymbol{\Psi}_{-} = \Xi\boldsymbol{\Psi}_{+}$.

We are interested in measuring which of the two sectors (±) the system is in. For this purpose, consider the thought experiment of Fig. 4.6, where we show three vortices, A, B, and M, each hosting a MZM[9]. To measure the fermion parity of the qubit constituted by MZMs in vortices A and M, we imagine M being directed towards A (step a). We will not go into detail here of how controlled vortex motion might be achieved in practice, but a brief overview of (successful) techniques is surveyed in Subsection 4.4.2. When the distance between A and M becomes comparable to the coherence length ξ, the states $\boldsymbol{\Psi}_{\mathrm{A}}$ and $\boldsymbol{\Psi}_{\mathrm{M}}$ of Eq. (4.35) hybridise with a parity-dependent sign. The parity-dependent hybridisation results in a small force contribution to the repulsive Lorentz force exerted mutually by A and M, as quantified in Subsection 4.3.4. Detecting this force contribution constitutes a measurement of the state of the qubit formed by A and M.

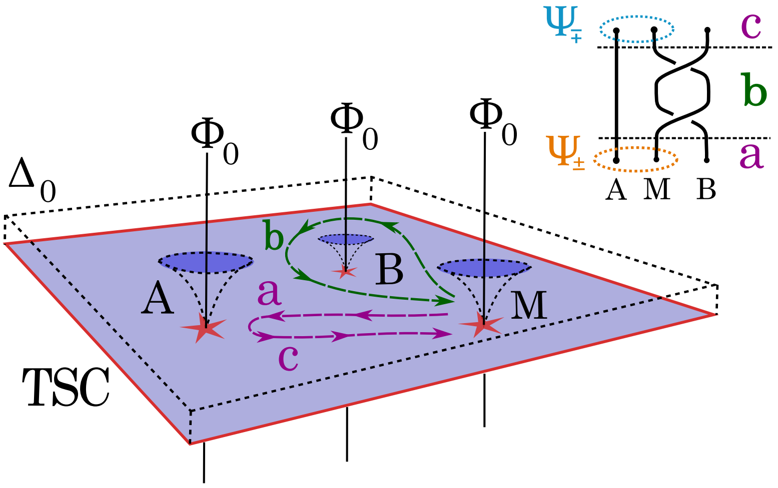

Figure 4.6: Envisioning braiding with Majorana vortex modes in a topological superconductor (TSC). Consider two stationary vortices, A and B, and a mobile vortex M, each hosting a Majorana zero mode (MZM), marked with red stars[9]. The gap profile is indicated with dashed lines. The qubit defined by MZMs A and M is initially in either of the states $\boldsymbol{\Psi}_{\pm}$. a: vortex M is moved close to A (on the order of ξ) to facilitate an indirect measurement of the hybridisation, b: M is braided with B resulting in a flip of the A-M qubit parity, and c: step a is repeated. The inset shows the braiding diagram with time running vertically.

---

[9] The total number of Majorana modes must be even to yield an integer number of fermionic degrees of freedom. In the context of Fig. 4.6 we imagine another MZM being localised on the edge of the sample, which is marked in red.

In step b, vortex M is directed around a third stationary vortex B, always separated from the other vortices by a distance much greater than ξ. This directed vortex motion is equivalent to the double braid shown in the inset of Fig. 4.6 and can readily be checked, with Eq. (4.34), to result in $\mathbf{\Psi}_{\pm} \mapsto \mathbf{\Psi}_{\mp}$ (up to an overall phase factor) for the qubit state defined by A and M. Finally, step a is repeated (called step c in Fig. 4.6) with the parity-dependent hybridisation having switched sign. If the inter-vortex force is successfully measured again and contrasted with the measurement in step a, this would be a clear demonstration of MZMs being non-Abelian anyons, and it would constitute a milestone towards topological quantum computation[10] [34]. In Section 4.4 some substantial obstacles to overcome in order to succeed in this experiment are discussed.

4.4.2 Vortex Manipulation

Naturally, the gap between the idealised picture of braiding envisioned in Fig. 4.6 and successfully performing such an experiment is huge. One of the major challenges to overcome is to actually have a controlled and precise way of moving vortices. However, intriguing progress has been made regarding vortex manipulation using magnetic force microscopy (MFM). This approach allows for measuring forces exerted from vortices on a sharp magnetic cantilever tip. In niobium thin films ($\xi \approx$ 10–20 nm) the lateral component of the tip force was estimated with about 1 pN precision, as inferred from the elastic properties of the tip and direct measurements of the vertical force component [189]. By adjustment of the tip distance from the sample surface, the technique was employed to controllably target and move individual vortices [189]. Braiding by use of MFM tips was recently proposed theoretically as a feasable route to topological quantum computation [194]. Vortex manipulation and force measurements have also been demonstrated with mechanical sharp tips [195], superconducting quantum interference devices (SQUID) [196], and local heating with a focused laser beam [197].

---

[10] To be precise, it would amount to a successful implementation of the Pauli-X gate.

We turn the attention to the superconductor $(\mathrm{Li}_{1-x}\mathrm{Fe}_x)\mathrm{OHFeSe}$ (for $x \approx 0.84$) with $T_c \approx 42$ K. This layered compound has recently emerged as a candidate surface topological superconductor. Density functional and dynamical mean-field theory [177], and angle-resolved photoemission spectroscopy (ARPES) [175, 198] identify a topologically non-trivial surface state with a Dirac-like dispersion, accompanied by a nodeless gap on the FeSe surface layer of size $\Delta_0 \approx 10$ meV. Similar to other iron-based superconductors, an attractive feature of this compound is its large minigap, on the order of $\delta_\varepsilon \approx 1$ meV ≈ 11 K, as a consequence of its Fermi energy $E_F \approx 50$–60 meV not being much larger than the superconducting gap [177]. The large minigap allows scanning tunnelling microscopy (STM) studies [177] to identify individual CdGM levels, clearly separated from the zero-bias peak which is attributed to a MZM. The band structure strongly suggests 2D behaviour [175]. However, we note that both how the surface states penetrate into the bulk and the bulk superconducting pairing symmetry are unclear at this point[11].

From the numerics of Section 4.3 we find $\varepsilon_0(R/\xi = 3) \approx 0.04\Delta_0$. This implies a force sensitivity of $\delta F \lesssim \varepsilon_0/\xi \approx 0.05$ pN, with $\xi \approx 1.4$ nm [177], to measure the difference between the pinning forces in the two parity sectors. This is, unfortunately, lower than what was reported in the seminal MFM study from 2008 [189], although optimistically close to encourage experimental effort in vortex manipulation in this or similar compounds. Despite the encouraging estimate, it is worth noting that the extremely short coherence length might make precise vortex manipulation challenging in some iron-based superconductors. In that regard, the compound $\mathrm{FeTe}_{0.55}\mathrm{Se}_{0.45}$ [175, 176, 199] has many features in common with $(\mathrm{Li}_{1-x}\mathrm{Fe}_x)\mathrm{OHFeSe}$ but, encouragingly, with a slightly longer coherence length of $\xi \approx 12$ nm [176].

4.4.3 Quasiparticle Poisoning and Timescales

A leading threat to topological quantum computation is uncontrolled flips of the qubit parity caused by free electrons or quasiparticles in the condensate [28, 34, 188]. Parity flips take place at random times but have an associated average time scale,

---

[11] Private communication with Tong Zhang.

denoted by the *poisoning time* [200]. For thermally activated quasiparticles the error rate is expected to be roughly [167]

$$\Gamma \approx k_B T e^{-\Delta_0/(k_B T)}, \tag{4.36}$$

which implies the poisoning time $t_p = \hbar/\Gamma$. Inserting $\Delta_0 = 10$ meV as relevant for $(\mathrm{Li}_{1-x}\mathrm{Fe}_x)\mathrm{OHFeSe}$ at $T = 5$ K results in the poisoning time $t_p \approx 20$ ms. Dragging a vortex around a loop of radius, say, 10ξ would thus require a vortex speed of at least $v \gtrsim 5\ \mu\mathrm{ms}^{-1}$. Considering naively the aforementioned approach of vortex dragging via laser heating[12], these speeds appear to be within experimental reach [197]. However, it is commonly believed that the estimate of Eq. (4.36) is too optimistic for $k_B T \ll \Delta_0$. In a disordered system, for instance, multiple gaps scales may be involved, and a more careful analysis is required. At any rate, experiments suggest far lower poisoning times than what is currently expected from theory [201, 202].

For the purpose of indirectly measuring the parity-dependent energy splitting of vortex-bound modes, it is of relevance to consider thermal fluctuations. The vortex-vortex distance is dynamical at finite temperature, which leads to smearing of an oscillating function (Eq. (4.31)). In a statistical average sense this can reduce the energy contrast between the two parity sectors significantly [192]. To minimise this problem we require the vortex pinning potential to be steep over the scale of the oscillation length $2\pi k_F^{-1} \approx 21$ nm, at least for temperatures greater than the minigap. This does not appear to be an unrealistic requirement when taking into account experimental developments [196].

Adiabatic vortex motion during braiding should be required to avoid exciting quasiparticles. Using Δ_0 as an estimate of the quasiparticle gap, the timescale below which we expect violation of adiabaticity is very short: $t_a \approx \hbar/\Delta_0 \approx 70$ fs[13]. Thus, at least in principle, the braiding time t should lie within the window

$$t_a \ll t \ll t_p, \tag{4.37}$$

---

[12] Disclaimer: bombarding the sample with high-energy photons and reducing the gap locally will surely excite quasiparticles that for the current purpose could be destructive.

[13] Requiring braiding times $t \gg t_a$ amounts to limiting the vortex speed by $v \ll \xi/(\hbar/\Delta_0) = v_F \approx 5.5 \cdot 10^4\ \mathrm{ms}^{-1}$ [177], in relation with the above discussion.

which at $T = 5$ K naively appears to span more than 10 orders of magnitude. One should interpret this as an overly optimistic estimate. Finally, another upper limit on the braiding time, $t \ll t_\varepsilon \approx \hbar/\varepsilon_0$, would arise from any residual energy splitting ε_0 due to a finite distance between the vortices during the braiding (step b in Fig. 4.6). However, due to the exponential decay in ε_0 with inter-vortex distance, t_ε can presumably be made much longer than t_p in iron-based superconductors.

4.5 Summary and Outlook

In this chapter we have studied vortex-bound MZMs in topological superconductors. With two vortices separated by a distance comparable to the coherence length, we have focused on the hybridisation of MZMs. The two MZMs, forming a doubly degenerate ground state in the large-separation limit, make up a two-level system – a topological qubit. In particular, we described how the free energy difference between the qubit states, dubbed the parity contrast, is influenced by thermal occupation of the excited CdGM core states. The parity contrast was considered as an indirect probe in read-out of the qubit, as exemplified via the associated vortex-vortex force contribution. The parity contrast was found to lie exponentially close to the zero-temperature result for temperatures less than roughly the minigap $\approx \Delta_0^2/E_F$ (the energy of the first excited core state). For temperatures below the full gap, exciting the CdGM states thermally was found to yield one factor of T^{-1} in the parity contrast for each occupied state on average. If the vortex core instead has a density of states associated with the in-gap states, the decay in temperature is exponential.

With the reciprocal dependence on temperature above the minigap, our results suggest that the temperature does *not* have to be $k_B T \ll \delta_\varepsilon$ to achieve read-out of the Majorana qubit – as mentioned in the introduction, MZMs can in theory coexist with the CdGM states as long as they do not interact with or via these states [188]. Local heating may even potentially prove to be a resource. If, for instance, the (external) magnetic field is limited by uncontrolled factors, increasing the temperature can decrease the lower critical field H_{c1} and hence prove useful.

Alternatively, one can imagine exciting the CdGM states on purpose to separate the vortex dynamics from the Majorana qubit parity.

The two compounds $(\mathrm{Li}_{1-x}\mathrm{Fe}_x)\mathrm{OHFeSe}$ [177] and $\mathrm{FeTe}_{0.55}\mathrm{Se}_{0.45}$ [176] were mentioned as two promising candidate topological superconductors in the context of the read-out considerations of this chapter. These iron-based compounds have appreciably large minigaps and thus accessible temperature windows in which one can aim at successfully reading out the Majorana qubit state via sensitive vortex-vortex force measurements. An alternative possible route to probing the parity sector could involve sensitive magnetic field measurements (with e.g. a nitrogen-diamond vacancy) near a pinned vortex as it repels off a second when the parity sector flips (uncontrollably) by quasiparticle poisoning.

We have, in a slightly ignorant fashion, focused on a simple spinless 2D model with $p + ip$ pairing to capture the essential features of topological superconductors. This is of course a gross simplification which leaves out the complications of spin and the question of what the pairing symmetry actually is (which is undecided) in the compound the results were applied to. However, the $p + ip$ model arguably captures the relevant physics needed to make sensible predictions in topological superconductors [192]. The model retains a simplicity which leaves analytical methods, at least partially, available and thereby offers transparency.

Finally, it should be mentioned that various interferometry protocols have been proposed [203–206] to verify the existence of (and to braid) chiral Majorana modes in topological superconductors. These proposals often rely on proximity-inducing superconductivity on the surface of topological insulators [172], and they are typically subject to tight restrictions caused by the low insulating quality of bulk topological insulators [37, 207].

Chapter 5

Conclusions

In this thesis we have been concerned with problems in unconventional superconductivity, in both lattice and continuum models. Our approach has spanned analytical and numerical methods of reoccurring relevance in condensed matter theory.

In Chapter 2 we methodically surveyed the weak-coupling theory of superconductivity. We subsequently narrowed the focus to a repulsive Hubbard model on the tetragonal lattice. To a great extent we focused on solving the linearised gap equation that results from weak-coupling theory when treating the two-particle vertex in the Cooper channel to leading order in the interaction strength. In the low-filling limit the (integral) gap equation was solved by means of analytical methods, and we recapitulated well-established results for a spherical Fermi surface. Away from low filling we established the superconducting phase diagram, as a function of the out-of-plane to in-plane hopping ratio $t_\perp/t_\parallel$ and chemical potential to in-plane hopping ratio $\mu/t_\parallel$, by solving the gap equation numerically. The phase diagram interpolates between what has been previously discussed in the literature ($t_\perp = 0$ and $t_\perp = t_\parallel$), and it is considered asymptotically exact in the weak-coupling limit.

Chapter 3 was concerned with the superconducting state of strontium ruthenate. This perovskite has maintained a special role in the history of unconventional superconductivity due to its long-hypothesised $p + ip$ pairing symmetry. In light of recent experiments strongly challenging this interpretation, we took on a microscopic and unbiased approach to calculate and compare relevant pairing channels. As such, we built an effective, yet accurate 3D three-band tight-binding model of the normal state via a band structure fit. To this model we added phenomenological multiband (Hubbard-like) interactions. In the weak-coupling limit we solved the generalised gap equation numerically. As a function of a single (undetermined) interaction parameter we found that helical p-wave triplet and d-wave singlet order was favoured. By comparing calculated results for these orders to specific heat and magnetic susceptibility data from experiments, we concluded that microscopic evidence now lean towards the superconducting state involving a d-wave order parameter component. As likely resolved by future calculations and experiments, the putative time-reversal symmetry breaking phase might involve two accidentally nearly-degenerate singlet order parameters.

Finally, in Chapter 4 we used an effective mean-field description of vortex modes in $p + ip$ superconductors. More generally, we reviewed properties of the anyonic quasiparticles, known as Majorana zero modes, that appear in the low-energy sector of topological superconductors. We described the hybridisation of Majorana modes in two vortices of finite separation, yielding a finite-energy two-level system for the topological qubit formed by the modes. In particular, we examined the impact of thermally occupying non-topological in-gap states in the vortex cores on the hybridisation. Since the hybridisation is sensitive to the state of the topological qubit, we discussed routes to measuring this hybridisation via its contribution to the vortex-vortex force in iron-based superconductors. The iron-based superconductors were proposed as promising candidates for future exploration and read-out of Majorana based qubits. These compounds have appreciably large minigaps, leaving an experimentally accessible temperature range in which one can avoid thermal activation of in-gap states.

To conclude, the results of this thesis shed light on the rich complexity of unconventional pairing states that arise from repulsive interactions in three dimensions, not only in complicated multiband systems. For instance, accidental and complicated nodal structures arise naturally and frequently with the weak-coupling approach on the lattice, and a minimal single-band model ranging four Fermi surface topologies was found to display five types of p- and d-wave orders. In the puzzling case of strontium ruthenate, we emphasise that the debate regarding its superconducting state has substantially heated up during the course of this work. Our contribution to this debate should be taken as suggestive and indicative. A body of conflicting results over the course of its 26-year-long history should be readdressed and re-evaluated as theory and experiment combine efforts in understanding its strongly correlated low-temperature phase. Independently of this perovskite, we have examined finite-temperature prospects for topological superconductivity that we hope will help non-Abelian anyons thrive in the coming decades.

Appendices

Appendix A

Solving Integral Equations with Orthogonal Polynomials

In Chapter 2 we encountered the integral equation of Eq. (2.22) that was to be solved in the prolate and oblate cases of Eqs. (2.40) and (2.41). Here, we show how the integral equation can be solved by expanding the kernel (the two-particle vertex) in orthogonal polynomials, and in such mapping it onto a standard matrix eigenvalue problem [68].

In the context of the problem encountered in Chapter 2 we apply the ansätze $\psi_{p_x \pm i p_y}(\theta, \phi) = \tilde{\psi}(\theta)\exp(\pm i\phi)$ and $\psi_{p_z}(\theta, \phi) = \tilde{\psi}(\theta)$. This is due to the lifted degeneracy of the spherical harmonics $Y_{l=1}^{m}$ into $Y_{l=1}^{m=\pm 1}$ and $Y_{l=1}^{m=0}$ when the Fermi surface is deformed into an oblate or prolate spheroid. Away from low filling (without rotational invariance), this splitting corresponds to the symmetry reduction $O_h \to D_{4h}$ and specifically to the respective irreps $T_{1u} \to \{A_{2u}, E_u\}$. The ansätze above allow us to integrate over ϕ' and reduce the problem to a one-variable integral equation:

$$\int_{-1}^{1} \mathrm{d}u'\, K(u, u')\tilde{\psi}(u') = \lambda \tilde{\psi}(u), \tag{A.1}$$

where we introduced $u = \cos\theta$, $u' = \cos\theta'$, and where $K(u, u')$ is the effective kernel (which is symmetric in u and u') after performing the integration over ϕ'. The solution is expanded in a set of orthogonal polynomials:

$$\tilde{\psi}(u) = \sum_n a_n p_n(u), \tag{A.2}$$

$$\int_{-1}^{1} \mathrm{d}u \; w(u) p_n(u) p_m(u) = c_n \delta_{nm}, \tag{A.3}$$

where $w(u)$ and c_n are weights and normalisation constants associated with the chosen set of polynomials $\{p_n(u)\}_n$ defined on $u \in [-1, 1]$, respectively. The expansion coefficients a_n are to be determined in the following. We expand the integration kernel in the same set of polynomials:

$$K(u, u') = \sum_n \frac{f_n(u')}{w(u')} p_n(u). \tag{A.4}$$

The kernel weight $f_n(u')$ introduced above is found by using Eq. (A.3) to invert the above equation:

$$f_n(u') = \frac{w(u')}{c_n} \int_{-1}^{1} \mathrm{d}u \; w(u) p_n(u) K(u, u'), \tag{A.5}$$

By inserting Eqs. (A.2), (A.4) and (A.5) into Eq. (A.1) it is revealed that the integral equation amounts to solving the eigenvalue problem

$$\sum_m A_{nm} a_m = \lambda a_n, \tag{A.6}$$

$$A_{nm} = \frac{1}{c_n} \int_{-1}^{1} \mathrm{d}u' \int_{-1}^{1} \mathrm{d}u \; w(u') p_n(u') K(u', u) p_m(u). \tag{A.7}$$

When the expansion series of Eq. (A.2) converges, one can in practice truncate the eigenvalue problem of Eq. (A.6) at finite dimension.

Due to the form of the expected solutions in the present context, we choose p_n to be Legendre polynomials (with $w(u) = 1$) and Chebyshev polynomials of the second kind (with $w(u) = \sqrt{1 - u^2}$) in the p_z and the $p_x \pm ip_y$ sectors, respectively.

Appendix B

Energy Hybridisation in an Annulus Geometry

In Chapter 4 we studied the energy hybridisation between Majorana vortex modes. We discussed how the hybridisation gives a contribution to the mutual vortex-vortex force that is sensitive to the ground state fermion parity. To illustrate the hybridisation between edge modes analytically, we consider the $p + ip$ model of Eq. (4.1) on an annulus with radii R_1 and $R_2 > R_1$, see Fig. B.1 and e.g. Refs. [32, 37, 208, 209].

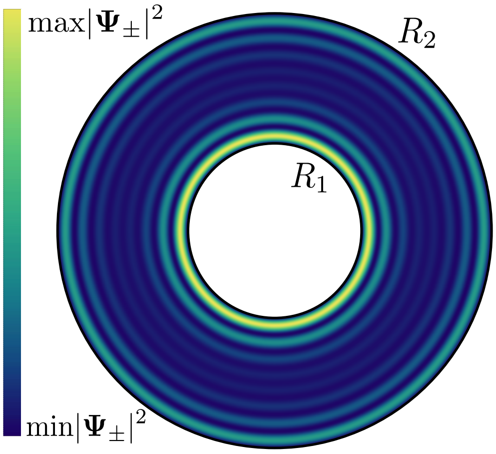

Figure B.1: An annulus geometry with edge modes on the inner (R_1) and outer (R_2) edge. The heat map reflects the electron density of the ground state candidates given in Eq. (B.1).

To model a flux quantum penetrating the central hole, we consider the order parameter $\Delta(\boldsymbol{r}) = \Delta_0 e^{i\theta}\Theta(r - R_1)\Theta(R_2 - r)$, where Θ is the Heaviside function, Δ_0

is a constant, and θ is the polar angle. We further assume that $2mE_F > \xi^{-2}$, where ξ is the coherence length, E_F is the Fermi energy, and m is the effective electron mass. This assumption causes the Majorana zero modes to exhibit radial oscillations with a frequency set by $k_F = \sqrt{2mE_F - 1/\xi^2}$, which is readily shown explicitly in Eq. (4.9). Outside the annulus, i.e. for $R < R_1$ and $R > R_2$, we let $E_F < 0$ (in the final step of the calculation we send $E_F \to -\infty$ outside the annulus). In the limit $R_2 \gg R_1 \gg 1/k_F$ the boundary states, which are localised exponentially close to the inner and outer edge, can both be expanded asymptotically.

In the same limit, we can construct the symmetric and asymmetric ground state candidates,

$$\boldsymbol{\Psi}_\pm = \frac{1}{\sqrt{2}}(\boldsymbol{\Psi}_1 \pm i\boldsymbol{\Psi}_2), \tag{B.1}$$

where $\boldsymbol{\Psi}_1$ ($\boldsymbol{\Psi}_2$) is the Majorana mode on edge R_1 (R_2), respectively [192]. The square modulus of these wavefunctions are visualised in Fig. B.1. By direct evaluation we obtain an estimate of the finite-R ground state energy as

$$\varepsilon_\pm = \langle \boldsymbol{\Psi}_\pm | \mathcal{H} | \boldsymbol{\Psi}_\pm \rangle \approx \mp \frac{8E_F}{k_F\xi} \sin(k_F R) \exp(-R/\xi), \tag{B.2}$$

where $R = R_2 - R_1$, and where we employed the limit $E_F \to -\infty$ outside the disk. The oscillations remind of an edge mode interference phenomenon, which yields exact zero modes for separations $Rk_F = n\pi$ with $n \in \mathbb{N}$. The same zero mode condition was obtained in Ref. [209] in the small-R limit (compared to k_F^{-1}) by imposing Dirichlet boundary conditions on the wavefunctions directly. The expression in Eq. (B.2) was confirmed by matrix diagonalisation and shows convincing agreement with numerics for $R \gtrsim 3\xi$ [208]. Moreover, the result is reminiscent of the splitting of two Majorana modes in point-like vortices, as given in Eq. (4.31).

References

[1] H. K. Onnes, "The Resistance of Pure Mercury at Helium Temperatures," Commun. Phys. Lab. Univ. Leiden **12** (1911).

[2] J. Bardeen, L. N. Cooper, and J. R. Schrieffer, "Microscopic Theory of Superconductivity," Phys. Rev. **106**, 162–164 (1957).

[3] B. T. Matthias, T. H. Geballe, and V. B. Compton, "Superconductivity," Rev. Mod. Phys. **35**, 1–22 (1963).

[4] D. D. Osheroff, R. C. Richardson, and D. M. Lee, "Evidence for a New Phase of Solid He^3," Phys. Rev. Lett. **28**, 885–888 (1972).

[5] P. W. Anderson and P. Morel, "Generalized Bardeen-Cooper-Schrieffer States and Aligned Orbital Angular Momentum in the Proposed Low-Temperature Phase of Liquid He^3," Phys. Rev. Lett. **5**, 136–138 (1960).

[6] P. W. Anderson and W. F. Brinkman, "Anisotropic Superfluidity in ^{3}He: A Possible Interpretation of Its Stability as a Spin-Fluctuation Effect," Phys. Rev. Lett. **30**, 1108–1111 (1973).

[7] R. Balian and N. R. Werthamer, "Superconductivity with Pairs in a Relative p Wave," Phys. Rev. **131**, 1553–1564 (1963).

[8] A. J. Leggett, "A theoretical description of the new phases of liquid ^{3}He," Rev. Mod. Phys. **47**, 331–414 (1975).

[9] F. Steglich, J. Aarts, C. D. Bredl, W. Lieke, D. Meschede, W. Franz, and H. Schäfer, "Superconductivity in the Presence of Strong Pauli Paramagnetism: $CeCu_2Si_2$," Phys. Rev. Lett. **43**, 1892–1896 (1979).

[10] J. G. Bednorz and K. A. Müller, "Possible high T_c superconductivity in the Ba–La–Cu–O system," Z. Phys. B **64**, 189–193 (1986).

[11] M. Sigrist and K. Ueda, "Phenomenological theory of unconventional superconductivity," Rev. Mod. Phys. **63**, 239–311 (1991).

[12] R. A. Fisher, S. Kim, B. F. Woodfield, N. E. Phillips, L. Taillefer, K. Hasselbach, J. Flouquet, A. L. Giorgi, and J. L. Smith, "Specific heat of UPt_3: Evidence for unconventional superconductivity," Phys. Rev. Lett. **62**, 1411–1414 (1989).

[13] R. Joynt and L. Taillefer, “The superconducting phases of UPt_3,” Rev. Mod. Phys. **74**, 235–294 (2002).

[14] W. Kohn and J. M. Luttinger, “New Mechanism for Superconductivity,” Phys. Rev. Lett. **15**, 524–526 (1965).

[15] S. Raghu, S. A. Kivelson, and D. J. Scalapino, “Superconductivity in the repulsive Hubbard model: An asymptotically exact weak-coupling solution,” Phys. Rev. B **81**, 224505 (2010).

[16] J. Hubbard, “Electron correlations in narrow energy bands,” Proc. R. Soc. Lond. A. **276**, 238 (1963).

[17] Y. Maeno, H. Hashimoto, K. Yoshida, S. Nishizaki, T. Fujita, J. G. Bednorz, and F. Lichtenberg, “Superconductivity in a layered perovskite without copper,” Nature **372**, 532–534 (1994).

[18] T. M. Rice and M. Sigrist, “Sr_2RuO_4: an electronic analogue of ^{3}He?” J. Phys. Condens. Matter **7**, L643–L648 (1995).

[19] A. Pustogow, Y. Luo, A. Chronister, Y.-S. Su, D. A. Sokolov, F. Jerzembeck, A. P. Mackenzie, C. W. Hicks, N. Kikugawa, S. Raghu, and S. E. Bauer, E. D. Brown, “Constraints on the superconducting order parameter in Sr_2RuO_4 from oxygen-17 nuclear magnetic resonance,” Nature **574**, 72–75 (2019).

[20] K. Ishida, M. Manago, K. Kinjo, and Y. Maeno, “Reduction of the ^{17}O Knight Shift in the Superconducting State and the Heat-up Effect by NMR Pulses on Sr_2RuO_4,” J. Phys. Soc. Jpn. **89**, 034712 (2020).

[21] N. Read and D. Green, “Paired states of fermions in two dimensions with breaking of parity and time-reversal symmetries and the fractional quantum Hall effect,” Phys. Rev. B **61**, 10267–10297 (2000).

[22] A. Y. Kitaev, “Unpaired Majorana fermions in quantum wires,” Phys. Usp. **44**, 131 (2001).

[23] D. A. Ivanov, “Non-Abelian Statistics of Half-Quantum Vortices in p-Wave Superconductors,” Phys. Rev. Lett. **86**, 268–271 (2001).

[24] G. Moore and N. Read, “Nonabelions in the fractional quantum hall effect,” Nucl. Phys. B **360**, 362 – 396 (1991).

[25] J. M. Leinaas and J. Myrheim, “On the theory of identical particles,” Il Nuovo Cimento B (1971-1996) **37**, 1–23 (1977).

[26] F. Wilczek, “Quantum Mechanics of Fractional-Spin Particles,” Phys. Rev. Lett. **49**, 957–959 (1982).

[27] Y.-S. Wu, “General Theory for Quantum Statistics in Two Dimensions,” Phys. Rev. Lett. **52**, 2103–2106 (1984).

[28] C. Nayak, S. H. Simon, A. Stern, M. Freedman, and S. Das Sarma, "Non-Abelian anyons and topological quantum computation," Rev. Mod. Phys. **80**, 1083–1159 (2008).

[29] P. W. Shor, "Proceedings of the 35th Annual Symposium on Foundations of Computer Science," (IEEE Computer Society Press, Los Alamitos, CA, 1994) pp. 124–134.

[30] R. P. Feynman, "Simulating physics with computers," Int. J. Theor. Phys. **21**, 467 (1982).

[31] F. Arute, K. Arya, R. Babbush, D. Bacon, J. C. Bardin, R. Barends, R. Biswas, S. Boixo, F. G. S. L. Brandao, D. A. Buell, B. Burkett, Y. Chen, Z. Chen, B. Chiaro, R. Collins, W. Courtney, A. Dunsworth, E. Farhi, B. Foxen, A. Fowler, C. Gidney, M. Giustina, R. Graff, K. Guerin, S. Habegger, M. P. Harrigan, M. J. Hartmann, A. Ho, M. Hoffmann, T. Huang, T. S. Humble, S. V. Isakov, E. Jeffrey, Z. Jiang, D. Kafri, K. Kechedzhi, J. Kelly, P. V. Klimov, S. Knysh, A. Korotkov, F. Kostritsa, D. Landhuis, M. Lindmark, E. Lucero, D. Lyakh, S. Mandrà, J. R. McClean, M. McEwen, A. Megrant, X. Mi, K. Michielsen, M. Mohseni, J. Mutus, O. Naaman, M. Neeley, C. Neill, M. Y. Niu, E. Ostby, A. Petukhov, J. C. Platt, C. Quintana, E. G. Rieffel, P. Roushan, N. C. Rubin, D. Sank, K. J. Satzinger, V. Smelyanskiy, K. J. Sung, M. D. Trevithick, A. Vainsencher, B. Villalonga, T. White, Z. J. Yao, P. Yeh, A. Zalcman, H. Neven, and J. M. Martinis, "Quantum supremacy using a programmable superconducting processor," Nature **574**, 505–510 (2019).

[32] J. Alicea, "New directions in the pursuit of Majorana fermions in solid state systems," Rep. Prog. Phys. **75**, 076501 (2012).

[33] C. Kallin and J. Berlinsky, "Chiral superconductors," Rep. Prog. Phys. **79**, 054502 (2016).

[34] D. Aasen, M. Hell, R. V. Mishmash, A. Higginbotham, J. Danon, M. Leijnse, T. S. Jespersen, J. A. Folk, C. M. Marcus, K. Flensberg, and J. Alicea, "Milestones Toward Majorana-Based Quantum Computing," Phys. Rev. X **6**, 031016 (2016).

[35] T. E. O'Brien, P. Rożek, and A. R. Akhmerov, "Majorana-Based Fermionic Quantum Computation," Phys. Rev. Lett. **120**, 220504 (2018).

[36] C. Caroli, P. D. Gennes, and J. Matricon, "Bound Fermion states on a vortex line in a type II superconductor," Phys. Lett. **9**, 307–309 (1964).

[37] H. S. Røising and S. H. Simon, "Size constraints on a Majorana beam-splitter interferometer: Majorana coupling and surface-bulk scattering," Phys. Rev. B **97**, 115424 (2018).

[38] H. S. Røising, F. Flicker, T. Scaffidi, and S. H. Simon, "Weak-coupling superconductivity in an anisotropic three-dimensional repulsive Hubbard model," Phys. Rev. B **98**, 224515 (2018).

[39] H. S. Røising, R. Ilan, T. Meng, S. H. Simon, and F. Flicker, "Finite temperature effects on Majorana bound states in chiral *p*-wave superconductors," SciPost Phys. **6**, 55 (2019).

[40] H. S. Røising, T. Scaffidi, F. Flicker, G. F. Lange, and S. H. Simon, "Superconducting order of Sr_2RuO_4 from a three-dimensional microscopic model," Phys. Rev. Research **1**, 033108 (2019).

[41] J. M. Luttinger, "New Mechanism for Superconductivity," Phys. Rev. **150**, 202–214 (1966).

[42] L. P. Gor'kov and T. K. Melik-Barkhudarov, "Contribution to the Theory of Superfluidity in an Imperfect Fermi Gas," J. Exptl. Theoret. Phys. (U.S.S.R) **13**, 1452–1458 (1961).

[43] N. W. Ashcroft and N. D. Mermin, *Solid State Physics* (Saunders College Publishing, 1976).

[44] S. Maiti and A. V. Chubukov, "Superconductivity from repulsive interaction," AIP Conf. Proc. **1550**, 3–73 (2013).

[45] F. H. L. Essler, H. Frahm, F. Göhmann, A. Klümper, and V. E. Korepin, *The One-Dimensional Hubbard Model* (Cambridge University Press, 2005).

[46] M. Jarrell, T. Maier, M. H. Hettler, and A. N. Tahvildarzadeh, "Phase diagram of the Hubbard model: Beyond the dynamical mean field," Europhys. Lett **56**, 563–569 (2001).

[47] J. P. F. LeBlanc, A. E. Antipov, F. Becca, I. W. Bulik, G. K.-L. Chan, C.-M. Chung, Y. Deng, M. Ferrero, T. M. Henderson, C. A. Jiménez-Hoyos, E. Kozik, X.-W. Liu, A. J. Millis, N. V. Prokof'ev, M. Qin, G. E. Scuseria, H. Shi, B. V. Svistunov, L. F. Tocchio, I. S. Tupitsyn, S. R. White, S. Zhang, B.-X. Zheng, Z. Zhu, and E. Gull (Simons Collaboration on the Many-Electron Problem), "Solutions of the Two-Dimensional Hubbard Model: Benchmarks and Results from a Wide Range of Numerical Algorithms," Phys. Rev. X **5**, 041041 (2015).

[48] D. J. Scalapino, E. Loh, and J. E. Hirsch, "*d*-wave pairing near a spin-density-wave instability," Phys. Rev. B **34**, 8190(R)–8192(R) (1986).

[49] A. V. Chubukov and J. P. Lu, "Pairing instabilities in the two-dimensional Hubbard model," Phys. Rev. B **46**, 11163–11166 (1992).

[50] M. A. Baranov and M. Y. Kagan, "D-wave pairing in the two-dimensional Hubbard model with low filling," Z. Phys. B **86**, 237–239 (1992).

[51] R. Hlubina, "Phase diagram of the weak-coupling two-dimensional $t - t'$ Hubbard model at low and intermediate electron density," Phys. Rev. B **59**, 9600–9605 (1999).

[52] H. Fukazawa and K. Yamada, "Third Order Perturbation Analysis of Pairing Symmetry in Two-Dimensional Hubbard Model," J. Phys. Soc. Jpn. **71**, 1541–1547 (2002).

[53] F. Šimkovic, X.-W. Liu, Y. Deng, and E. Kozik, "Ground-state phase diagram of the repulsive fermionic $t - t^{'}$ hubbard model on the square lattice from weak coupling," Phys. Rev. B **94**, 085106 (2016).

[54] A. T. Rømer, A. Kreisel, I. Eremin, M. A. Malakhov, T. A. Maier, P. J. Hirschfeld, and B. M. Andersen, "Pairing symmetry of the one-band Hubbard model in the paramagnetic weak-coupling limit: A numerical RPA study," Phys. Rev. B **92**, 104505 (2015).

[55] A. Kreisel, A. T. Rømer, P. J. Hirschfeld, and B. M. Andersen, "Superconducting Phase Diagram of the Paramagnetic One-Band Hubbard Model," J. Supercond. Nov. Magn. **30**, 85–89 (2017).

[56] H. Bruus and K. Flensberg, *Many-Body Quantum Theory in Condensed Matter Physics* (Oxford University Press, 2004).

[57] R. Shankar, "Renormalization-group approach to interacting fermions," Rev. Mod. Phys. **66**, 129–192 (1994).

[58] M. Tinkham, *Introduction to superconductivity* (McGraw-Hill New York, 1975).

[59] T. Scaffidi, *Weak-Coupling Theory of Topological Superconductivity: The Case of Strontium Ruthenate*, Springer Theses (Springer International Publishing, 2017).

[60] A. Altland and B. Simons, *Condensed Matter Field Theory* (Cambridge Universtiy Press, 2010).

[61] J. Linder and A. V. Balatsky, "Odd-frequency superconductivity," Rev. Mod. Phys. **91**, 045005 (2019).

[62] E. E. Salpeter and H. A. Bethe, "A Relativistic Equation for Bound-State Problems," Phys. Rev. **84**, 1232–1242 (1951).

[63] T. Takimoto and T. Moriya, "Superconductivity and antiferromagnetism in the three-dimensional Hubbard model," Phys. Rev. B **66**, 134516 (2002).

[64] N. Yoshioka, Y. Imai, and M. Sigrist, "Spontaneous Thermal Hall Effect in Three-dimensional Chiral Superconductors with Gap Nodes," J. Phys. Soc. Jpn. **87**, 124602 (2018).

[65] A. P. Schnyder, S. Ryu, A. Furusaki, and A. W. W. Ludwig, "Classification of topological insulators and superconductors in three spatial dimensions," Phys. Rev. B **78**, 195125 (2008).

[66] I. M. Lifshitz, "Anomalies of Electron Characteristics of a Metal in the High Pressure Region," J. Exptl. Theoret. Phys. (U.S.S.R) **11**, 1569–1576 (1960).

[67] D. Fay and A. Layzer, "Superfluidity of Low-Density Fermion Systems," Phys. Rev. Lett. **20**, 187–190 (1968).

[68] P. M. Morse and H. Feshbach, *Methods of Theoretical Physics* (McGraw-Hill Book Company, Inc., 1953).

[69] M. Sigrist, "Introduction to Unconventional Superconductivity," AIP Conf. Proc. **789**, 165–243 (2005).

[70] W. P. Halperin, J. M. Parpia, and J. A. Sauls, "Superfluid helium-3 in confined quarters," Physics Today **71**, 30 (2018).

[71] Y. Deng, E. Kozik, N. V. Prokof'ev, and B. V. Svistunov, "Emergent BCS regime of the two-dimensional fermionic Hubbard model: Ground-state phase diagram," EPL **110**, 57001 (2015).

[72] C. J. Halboth and W. Metzner, "Renormalization-group analysis of the two-dimensional Hubbard model," Phys. Rev. B **61**, 7364–7377 (2000).

[73] J. Reiss, D. Rohe, and W. Metzner, "Renormalized mean-field analysis of antiferromagnetism and d-wave superconductivity in the two-dimensional Hubbard model," Phys. Rev. B **75**, 075110 (2007).

[74] J. Ehrlich and C. Honerkamp, "Functional renormalization group for fermion lattice models in three dimensions: application to the Hubbard model on the cubic lattice," arXiv:2004.14711 [cond-mat.str-el] (2020).

[75] E. Fradkin, *Field Theories of Condensed Matter Physics (Second Edition)* (Cambridge University Press, 2013).

[76] M. H. Fischer and E. Berg, "Fluctuation and strain effects in a chiral p-wave superconductor," Phys. Rev. B **93**, 054501 (2016).

[77] L. Fu and E. Berg, "Odd-Parity Topological Superconductors: Theory and Application to $\mathrm{Cu}_x\mathrm{Bi}_2\mathrm{Se}_3$," Phys. Rev. Lett. **105**, 097001 (2010).

[78] L. Fu, "Odd-parity topological superconductor with nematic order: Application to $\mathrm{Cu}_x\mathrm{Bi}_2\mathrm{Se}_3$," Phys. Rev. B **90**, 100509 (2014).

[79] A. P. Mackenzie and Y. Maeno, "The superconductivity of $\mathrm{Sr}_2\mathrm{RuO}_4$ and the physics of spin-triplet pairing," Rev. Mod. Phys. **75**, 657–712 (2003).

[80] A. Altland and M. R. Zirnbauer, "Nonstandard symmetry classes in mesoscopic normal-superconducting hybrid structures," Phys. Rev. B **55**, 1142–1161 (1997).

[81] C.-K. Chiu, J. C. Y. Teo, A. P. Schnyder, and S. Ryu, "Classification of topological quantum matter with symmetries," Rev. Mod. Phys. **88**, 035005 (2016).

[82] M. Cheng, K. Sun, V. Galitski, and S. Das Sarma, "Stable topological superconductivity in a family of two-dimensional fermion models," Phys. Rev. B **81**, 024504 (2010).

[83] T. Meng and L. Balents, "Weyl superconductors," Phys. Rev. B **86**, 054504 (2012).

[84] T. Maier, M. Jarrell, T. Pruschke, and M. H. Hettler, "Quantum cluster theories," Rev. Mod. Phys. **77**, 1027–1080 (2005).

[85] A. T. Rømer, T. A. Maier, A. Kreisel, I. Eremin, P. J. Hirschfeld, and B. M. Andersen, "Pairing in the two-dimensional Hubbard model from weak to strong coupling," Phys. Rev. Research **2**, 013108 (2020).

[86] M. Qin, C.-M. Chung, H. Shi, C. H. Ettore Vitali, U. Schollwöck, S. R. White, and S. Zhang, "Absence of superconductivity in the pure two-dimensional Hubbard model," arXiv:1910.08931 [cond-mat.str-el] (2019).

[87] C. Bergemann, A. P. Mackenzie, S. R. Julian, D. Forsythe, and E. Ohmichi, "Quasi-two-dimensional Fermi liquid properties of the unconventional superconductor Sr_2RuO_4," Adv. Phys. **52**, 639–725 (2003).

[88] I. Eremin, D. Manske, S. Ovchinnikov, and J. Annett, "Unconventional superconductivity and magnetism in Sr_2RuO_4 and related materials," Ann. Phys. **13**, 149–174 (2004).

[89] C. Kallin, "Chiral p-wave order in Sr_2RuO_4," Rep. Prog. Phys. **75**, 042501 (2012).

[90] A. P. Mackenzie, T. Scaffidi, C. W. Hicks, and Y. Maeno, "Even odder after twenty-three years: the superconducting order parameter puzzle of Sr_2RuO_4," npj Quantum Materials **2**, 40 (2017).

[91] Y. Maeno, T. M. Rice, and M. Sigrist, "The Intriguing Superconductivity of Strontium Ruthenate," Physics Today **54**, 42–47 (2001).

[92] A. Damascelli, D. H. Lu, K. M. Shen, N. P. Armitage, F. Ronning, D. L. Feng, C. Kim, Z.-X. Shen, T. Kimura, Y. Tokura, Z. Q. Mao, and Y. Maeno, "Fermi Surface, Surface States, and Surface Reconstruction in Sr_2RuO_4," Phys. Rev. Lett. **85**, 5194–5197 (2000).

[93] A. Tamai, M. Zingl, E. Rozbicki, E. Cappelli, S. Riccò, A. de la Torre, S. McKeown Walker, F. Y. Bruno, P. D. C. King, W. Meevasana, M. Shi, M. Radović, N. C. Plumb, A. S. Gibbs, A. P. Mackenzie, C. Berthod, H. U. R. Strand, M. Kim, A. Georges, and F. Baumberger, "High-Resolution

Photoemission on Sr_2RuO_4 Reveals Correlation-Enhanced Effective Spin-Orbit Coupling and Dominantly Local Self-Energies," Phys. Rev. X **9**, 021048 (2019).

[94] C. Bergemann, S. R. Julian, A. P. Mackenzie, S. NishiZaki, and Y. Maeno, "Detailed Topography of the Fermi Surface of Sr_2RuO_4," Phys. Rev. Lett. **84**, 2662–2665 (2000).

[95] V. Grinenko, S. Ghosh, R. Sarkar, J.-C. Orain, A. Nikitin, M. Elender, D. Das, Z. Guguchia, F. Brückner, M. E. Barber, J. Park, N. Kikugawa, D. A. Sokolov, J. S. Bobowski, T. Miyoshi, Y. Maeno, A. P. Mackenzie, H. Luetkens, C. W. Hicks, and H.-H. Klauss, "Split superconducting and time-reversal symmetry-breaking transitions, and magnetic order in Sr_2RuO_4 under uniaxial stress," arXiv:2001.08152 [cond-mat.supr-con] (2019).

[96] G. M. Luke, Y. Fudamoto, K. M. Kojima, M. I. Larkin, J. Merrin, B. Nachumi, Y. J. Uemura, Y. Maeno, Z. Q. Mao, Y. Mori, H. Nakamura, and M. Sigrist, "Time-reversal symmetry-breaking superconductivity in Sr_2RuO_4," Nature **394**, 558–561 (1998).

[97] J. Xia, Y. Maeno, P. T. Beyersdorf, M. M. Fejer, and A. Kapitulnik, "High Resolution Polar Kerr Effect Measurements of Sr_2RuO_4: Evidence for Broken Time-Reversal Symmetry in the Superconducting State," Phys. Rev. Lett. **97**, 167002 (2006).

[98] K. Ishida, H. Mukuda, Y. Kitaoka, K. Asayama, Z. Q. Mao, Y. Mori, and Y. Maeno, "Spin-triplet superconductivity in Sr_2RuO_4 identified by ^{17}O Knight shift," Nature **396**, 658–660 (1998).

[99] K. Ishida, H. Mukuda, Y. Kitaoka, Z. Q. Mao, H. Fukazawa, and Y. Maeno, "Ru NMR probe of spin susceptibility in the superconducting state of Sr_2RuO_4," Phys. Rev. B **63**, 060507(R) (2001).

[100] S. NishiZaki, Y. Maeno, and Z. Mao, "Changes in the Superconducting State of Sr_2RuO_4 under Magnetic Fields Probed by Specific Heat," J. Phys. Soc. Jpn. **69**, 572–578 (2000).

[101] T. Nomura and K. Yamada, "Detailed Investigation of Gap Structure and Specific Heat in the p-wave Superconductor Sr_2RuO_4," J. Phys. Soc. Jpn. **71**, 404–407 (2002).

[102] K. Deguchi, Z. Q. Mao, H. Yaguchi, and Y. Maeno, "Gap Structure of the Spin-Triplet Superconductor Sr_2RuO_4 Determined from the Field-Orientation Dependence of the Specific Heat," Phys. Rev. Lett. **92**, 047002 (2004).

[103] E. Hassinger, P. Bourgeois-Hope, H. Taniguchi, S. René de Cotret, G. Grissonnanche, M. S. Anwar, Y. Maeno, N. Doiron-Leyraud, and L. Taillefer, "Vertical Line Nodes in the Superconducting Gap Structure of Sr_2RuO_4," Phys. Rev. X **7**, 011032 (2017).

[104] J. F. Dodaro, Z. Wang, and C. Kallin, “Effects of deep superconducting gap minima and disorder on residual thermal transport in Sr_2RuO_4,” Phys. Rev. B **98**, 214520 (2018).

[105] C. Lupien, W. A. MacFarlane, C. Proust, L. Taillefer, Z. Q. Mao, and Y. Maeno, “Ultrasound Attenuation in Sr_2RuO_4: An Angle-Resolved Study of the Superconducting Gap Function,” Phys. Rev. Lett. **86**, 5986–5989 (2001).

[106] M. B. Walker and P. Contreras, “Theory of elastic properties of Sr_2RuO_4 at the superconducting transition temperature,” Phys. Rev. B **66**, 214508 (2002).

[107] C. W. Hicks, D. O. Brodsky, E. A. Yelland, A. S. Gibbs, J. A. N. Bruin, M. E. Barber, S. D. Edkins, K. Nishimura, S. Yonezawa, Y. Maeno, and A. P. Mackenzie, “Strong Increase of T_c of Sr_2RuO_4 Under Both Tensile and Compressive Strain,” Science **344**, 283–285 (2014).

[108] A. Steppke, L. Zhao, M. E. Barber, T. Scaffidi, F. Jerzembeck, H. Rosner, A. S. Gibbs, Y. Maeno, S. H. Simon, A. P. Mackenzie, and C. W. Hicks, “Strong peak in T_c of Sr_2RuO_4 under uniaxial pressure,” Science **355**, eaaf9398 (2017).

[109] Y.-S. Li, N. Kikugawa, D. Sokolov, F. Jerzembeck, A. Gibbs, Y. Maeno, C. Hicks, M. Nicklas, and A. Mackenzie, “High precision heat capacity measurements on Sr_2RuO_4 under uniaxial pressure,” arXiv:1906.07597 [cond-mat.supr-con] (2019).

[110] M. W. Haverkort, I. S. Elfimov, L. H. Tjeng, G. A. Sawatzky, and A. Damascelli, “Strong Spin-Orbit Coupling Effects on the Fermi Surface of Sr_2RuO_4 and Sr_2RhO_4,” Phys. Rev. Lett. **101**, 026406 (2008).

[111] C. N. Veenstra, Z.-H. Zhu, M. Raichle, B. M. Ludbrook, A. Nicolaou, B. Slomski, G. Landolt, S. Kittaka, Y. Maeno, J. H. Dil, I. S. Elfimov, M. W. Haverkort, and A. Damascelli, “Spin-Orbital Entanglement and the Breakdown of Singlets and Triplets in Sr_2RuO_4 Revealed by Spin- and Angle-Resolved Photoemission Spectroscopy,” Phys. Rev. Lett. **112**, 127002 (2014).

[112] F. B. Kugler, M. Zingl, H. U. R. Strand, S.-S. B. Lee, J. von Delft, and A. Georges, “Strongly Correlated Materials from a Numerical Renormalization Group Perspective: How the Fermi-Liquid State of Sr_2RuO_4 Emerges,” Phys. Rev. Lett. **124**, 016401 (2020).

[113] J. S. Bobowski, N. Kikugawa, T. Miyoshi, H. Suwa, H.-s. Xu, S. Yonezawa, D. A. Sokolov, A. P. Mackenzie, and Y. Maeno, “Improved Single-Crystal Growth of Sr_2RuO_4,” Condens. Matter **4**, 6 (2019).

[114] H. G. Suh, H. Menke, P. Brydon, C. Timm, A. Ramires, and D. F. Agterberg, “Stabilizing Even-Parity Chiral Superconductivity in Sr_2RuO_4,” arXiv:1912.09525 [cond-mat.supr-con] (2019).

[115] O. Gingras, R. Nourafkan, A.-M. S. Tremblay, and M. Côté, "Superconducting Symmetries of Sr_2RuO_4 from First-Principles Electronic Structure," Phys. Rev. Lett. **123**, 217005 (2019).

[116] T. Scaffidi, J. C. Romers, and S. H. Simon, "Pairing symmetry and dominant band in Sr_2RuO_4," Phys. Rev. B **89**, 220510(R) (2014).

[117] L.-D. Zhang, W. Huang, F. Yang, and H. Yao, "Superconducting pairing in Sr_2RuO_4 from weak to intermediate coupling," Phys. Rev. B **97**, 060510(R) (2018).

[118] A. T. Rømer, D. D. Scherer, I. M. Eremin, P. J. Hirschfeld, and B. M. Andersen, "Knight Shift and Leading Superconducting Instability from Spin Fluctuations in Sr_2RuO_4," Phys. Rev. Lett. **123**, 247001 (2019).

[119] K. I. Wysokiński, G. Litak, J. F. Annett, and B. L. Györffy, "Spin triplet superconductivity in Sr_2RuO_4," Phys. Status Solidi B **236**, 325–331 (2003).

[120] G. Litak, J. F. Annett, B. L. Györffy, and K. I. Wysokiński, "Horizontal line nodes in superconducting Sr_2RuO_4," Phys. Status Solidi B **241**, 983–989 (2004).

[121] I. Žutić and I. Mazin, "Phase-Sensitive Tests of the Pairing State Symmetry in Sr_2RuO_4," Phys. Rev. Lett. **95**, 217004 (2005).

[122] S. Kittaka, S. Nakamura, T. Sakakibara, N. Kikugawa, T. Terashima, S. Uji, D. A. Sokolov, A. P. Mackenzie, K. Irie, Y. Tsutsumi, K. Suzuki, and K. Machida, "Searching for Gap Zeros in Sr_2RuO_4 via Field-Angle-Dependent Specific-Heat Measurement," J. Phys. Soc. Jpn. **87**, 093703 (2018).

[123] E. Dagotto, T. Hotta, and A. Moreo, "Colossal magnetoresistant materials: the key role of phase separation," Phys. Rep. **344**, 1–153 (2001).

[124] K. K. Ng and M. Sigrist, "The role of spin-orbit coupling for the superconducting state in Sr_2RuO_4," EPL **49**, 473–479 (2000).

[125] H. Kontani, T. Tanaka, D. S. Hirashima, K. Yamada, and J. Inoue, "Giant Intrinsic Spin and Orbital Hall Effects in Sr_2MO_4 ($M =$ Ru, Rh, Mo)," Phys. Rev. Lett. **100**, 096601 (2008).

[126] A. Ramires and M. Sigrist, "Superconducting order parameter of Sr_2RuO_4: A microscopic perspective," Phys. Rev. B **100**, 104501 (2019).

[127] F. Flicker, *The Geometry and Topology of Charge-Ordered Quantum Fields in Low-Dimensional Systems*, Ph.D. thesis, University of Bristol (2015).

[128] W. Cho, R. Thomale, S. Raghu, and S. A. Kivelson, "Band structure effects on the superconductivity in Hubbard models," Phys. Rev. B **88**, 064505 (2013).

[129] M. Tsuchiizu, Y. Yamakawa, S. Onari, Y. Ohno, and H. Kontani, "Spin-triplet superconductivity in Sr_2RuO_4 due to orbital and spin fluctuations: Analyses by two-dimensional renormalization group theory and self-consistent vertex-correction method," Phys. Rev. B **91**, 155103 (2015).

[130] W. Cho, C. Platt, R. H. McKenzie, and S. Raghu, "Spin-triplet superconductivity in a weak-coupling Hubbard model for the quasi-one-dimensional compound $Li_{0.9}Mo_6O_{17}$," Phys. Rev. B **92**, 134514 (2015).

[131] S. Wolf, T. L. Schmidt, and S. Rachel, "Unconventional superconductivity in the extended Hubbard model: Weak-coupling renormalization group," Phys. Rev. B **98**, 174515 (2018).

[132] J. Kopp, "Efficient numerical diagonalization of Hermitian 3 × 3 matrices," Int. J. Mod. Phys. C **19**, 523–548 (2008).

[133] L. Vaugier, H. Jiang, and S. Biermann, "Hubbard U and Hund exchange J in transition metal oxides: Screening versus localization trends from constrained random phase approximation," Phys. Rev. B **86**, 165105 (2012).

[134] J. Mravlje, M. Aichhorn, T. Miyake, K. Haule, G. Kotliar, and A. Georges, "Coherence-Incoherence Crossover and the Mass-Renormalization Puzzles in Sr_2RuO_4," Phys. Rev. Lett. **106**, 096401 (2011).

[135] J.-W. Huo, T. M. Rice, and F.-C. Zhang, "Spin Density Wave Fluctuations and p-Wave Pairing in Sr_2RuO_4," Phys. Rev. Lett. **110**, 167003 (2013).

[136] M. Behrmann, C. Piefke, and F. Lechermann, "Multiorbital physics in Fermi liquids prone to magnetic order," Phys. Rev. B **86**, 045130 (2012).

[137] J. F. Annett, G. Litak, B. L. Györffy, and K. I. Wysokiński, "Spin-orbit coupling and symmetry of the order parameter in strontium ruthenate," Phys. Rev. B **73**, 134501 (2006).

[138] Z. Wang, X. Wang, and C. Kallin, "Spin-orbit coupling and spin-triplet pairing symmetry in Sr_2RuO_4," Phys. Rev. B **101**, 064507 (2020).

[139] I. A. Firmo, S. Lederer, C. Lupien, A. P. Mackenzie, J. C. Davis, and S. A. Kivelson, "Evidence from tunneling spectroscopy for a quasi-one-dimensional origin of superconductivity in Sr_2RuO_4," Phys. Rev. B **88**, 134521 (2013).

[140] W.-S. Wang, C.-C. Zhang, F.-C. Zhang, and Q.-H. Wang, "Theory of Chiral p-Wave Superconductivity with Near Nodes for Sr_2RuO_4," Phys. Rev. Lett. **122**, 027002 (2019).

[141] W. Metzner and D. Vollhardt, "Ground-state energy of the d=1,2,3 dimensional Hubbard model in the weak-coupling limit," Phys. Rev. B **39**, 4462–4466 (1989).

[142] D. Baeriswyl, "Superconductivity from repulsion: Variational results for the two-dimensional Hubbard model in the limit of weak interaction," Phys. Rev. B **99**, 235152 (2019).

[143] S. Nishizaki, Y. Maeno, S. Farner, S.-i. Ikeda, and T. Fujita, "Evidence for Unconventional Superconductivity of Sr_2RuO_4 from Specific-Heat Measurements," J. Phys. Soc. Jpn. **67**, 560–563 (1998).

[144] R. Sharma, S. D. Edkins, Z. Wang, A. Kostin, C. Sow, Y. Maeno, A. P. Mackenzie, J. C. S. Davis, and V. Madhavan, "Momentum-resolved superconducting energy gaps of Sr_2RuO_4 from quasiparticle interference imaging," PNAS **117**, 5222–5227 (2020).

[145] A. Ramires and M. Sigrist, "A note on the upper critical field of Sr_2RuO_4 under strain," J. Phys. Conf. Ser. **807**, 052011 (2017).

[146] J. F. Annett, "Symmetry of the order parameter for high-temperature superconductivity," Adv. Phys. **39**, 83–126 (1990).

[147] T. M. Riseman, P. G. Kealey, E. M. Forgan, A. P. Mackenzie, L. M. Galvin, A. W. Tyler, S. L. Lee, C. Ager, D. M. Paul, C. M. Aegerter, R. Cubitt, Z. Q. Mao, T. Akima, and Y. Maeno, "Observation of a square flux-line lattice in the unconventional superconductor Sr_2RuO_4," Nature **574**, 242–245 (1998).

[148] S. Ghosh, A. Shekhter, F. Jerzembeck, N. Kikugawa, D. A. Sokolov, M. Brando, A. P. Mackenzie, C. W. Hicks, and B. J. Ramshaw, "Thermodynamic Evidence for a Two-Component Superconducting Order Parameter in Sr_2RuO_4," arXiv:2002.06130 [cond-mat.supr-con] (2020).

[149] S. Benhabib, C. Lupien, I. Paul, L. Berges, M. Dion, M. Nardone, A. Zitouni, Z. Mao, Y. Maeno, A. Georges, L. Taillefer, and C. Proust, "Jump in the c_{66} shear modulus at the superconducting transition of Sr_2RuO_4: Evidence for a two-component order parameter," arXiv:2002.05916 [cond-mat.supr-con] (2020).

[150] W. Huang and H. Yao, "Possible Three-Dimensional Nematic Odd-Parity Superconductivity in Sr_2RuO_4," Phys. Rev. Lett. **121**, 157002 (2018).

[151] W. Huang, Y. Zhou, and H. Yao, "Possible 3D nematic odd-parity pairing in Sr_2RuO_4: experimental evidences and predictions," arXiv:1901.07041 [cond-mat.supr-con] (2019).

[152] W.-C. Lee, S.-C. Zhang, and C. Wu, "Pairing State with a Time-Reversal Symmetry Breaking in FeAs-Based Superconductors," Phys. Rev. Lett. **102**, 217002 (2009).

[153] S. A. Kivelson, A. C. Yuan, B. J. Ramshaw, and R. Thomale, "A proposal for reconciling diverse experiments on the superconducting state in Sr_2RuO_4," arXiv:2002.00016 [cond-mat.supr-con] (2020).

[154] S. Raghu, E. Berg, A. V. Chubukov, and S. A. Kivelson, “Effects of longer-range interactions on unconventional superconductivity,” Phys. Rev. B **85**, 024516 (2012).

[155] S. Kashiwaya, K. Saitoh, H. Kashiwaya, M. Koyanagi, M. Sato, K. Yada, Y. Tanaka, and Y. Maeno, “Time-reversal invariant superconductivity of Sr_2RuO_4 revealed by Josephson effects,” Phys. Rev. B **100**, 094530 (2019).

[156] S. Mazumdar, “Sr_2RuO_4, like doped cuprates and barium bismuthate, is a negative charge-transfer gap even parity superconductor with 3/4-filled oxygen band,” arXiv:2002.08451 [cond-mat.supr-con] (2020).

[157] S. K. Yip and J. A. Sauls, “Circular dichroism and birefringence in unconventional superconductors,” J. Low Temp. Phys. **86**, 257–290 (1992).

[158] K. I. Wysokiński, J. F. Annett, and B. L. Györffy, “Intrinsic Optical Dichroism in the Chiral Superconducting State of Sr_2RuO_4,” Phys. Rev. Lett. **108**, 077004 (2012).

[159] A. P. Mackenzie, “A Personal Perspective on the Unconventional Superconductivity of Sr_2RuO_4,” J. Supercond. Nov. Magn. **33**, 177–182 (2020).

[160] A. N. Petsch, M. Zhu, M. Enderle, Z. Q. Mao, Y. Maeno, and S. M. Hayden, “Reduction of the spin susceptibility in the superconducting state of Sr_2RuO_4 observed by polarized neutron scattering,” arXiv:2002.02856 [cond-mat.supr-con] (2020).

[161] K. v. Klitzing, G. Dorda, and M. Pepper, “New Method for High-Accuracy Determination of the Fine-Structure Constant Based on Quantized Hall Resistance,” Phys. Rev. Lett. **45**, 494–497 (1980).

[162] D. C. Tsui, H. L. Stormer, and A. C. Gossard, “Two-Dimensional Magnetotransport in the Extreme Quantum Limit,” Phys. Rev. Lett. **48**, 1559–1562 (1982).

[163] X.-L. Qi and S.-C. Zhang, “Topological insulators and superconductors,” Rev. Mod. Phys. **83**, 1057–1110 (2011).

[164] X. G. Wen, “Non-Abelian statistics in the fractional quantum Hall states,” Phys. Rev. Lett. **66**, 802–805 (1991).

[165] E. Majorana, “Teoria simmetrica dell’elettrone e del positrone,” Il Nuovo Cimento **14**, 171–184 (1937).

[166] V. Gurarie and L. Radzihovsky, “Zero modes of two-dimensional chiral p-wave superconductors,” Phys. Rev. B **75**, 212509 (2007).

[167] S. Das Sarma, M. Freedman, and C. Nayak, “Topologically Protected Qubits from a Possible Non-Abelian Fractional Quantum Hall State,” Phys. Rev. Lett. **94**, 166802 (2005).

[168] V. Mourik, K. Zuo, S. M. Frolov, S. R. Plissard, E. P. A. M. Bakkers, and L. P. Kouwenhoven, "Signatures of Majorana Fermions in Hybrid Superconductor-Semiconductor Nanowire Devices," Science **336**, 1003–1007 (2012).

[169] S. Nadj-Perge, I. K. Drozdov, J. Li, H. Chen, S. Jeon, J. Seo, A. H. MacDonald, B. A. Bernevig, and A. Yazdani, "Observation of Majorana fermions in ferromagnetic atomic chains on a superconductor," Science **346**, 602–607 (2014).

[170] A. P. Higginbotham, S. M. Albrecht, G. Kiršanskas, W. Chang, F. Kuemmeth, P. Krogstrup, T. S. Jespersen, J. Nygård, K. Flensberg, and C. M. Marcus, "Parity lifetime of bound states in a proximitized semiconductor nanowire," Nat. Phys. **11**, 1017–1021 (2015).

[171] Q. L. He, L. Pan, A. L. Stern, E. C. Burks, X. Che, G. Yin, J. Wang, B. Lian, Q. Zhou, E. S. Choi, K. Murata, X. Kou, Z. Chen, T. Nie, Q. Shao, Y. Fan, S.-C. Zhang, K. Liu, J. Xia, and K. L. Wang, "Chiral Majorana fermion modes in a quantum anomalous Hall insulator–superconductor structure," Science **357**, 294–299 (2017).

[172] L. Fu and C. L. Kane, "Superconducting Proximity Effect and Majorana Fermions at the Surface of a Topological Insulator," Phys. Rev. Lett. **100**, 096407 (2008).

[173] G. Koren, T. Kirzhner, E. Lahoud, K. B. Chashka, and A. Kanigel, "Proximity-induced superconductivity in topological Bi_2Te_2Se and Bi_2Se_3 films: Robust zero-energy bound state possibly due to Majorana fermions," Phys. Rev. B **84**, 224521 (2011).

[174] J.-P. Xu, M.-X. Wang, Z. L. Liu, J.-F. Ge, X. Yang, C. Liu, Z. A. Xu, D. Guan, C. L. Gao, D. Qian, Y. Liu, Q.-H. Wang, F.-C. Zhang, Q.-K. Xue, and J.-F. Jia, "Experimental Detection of a Majorana Mode in the core of a Magnetic Vortex inside a Topological Insulator-Superconductor $Bi_2Te_3/NbSe_2$ Heterostructure," Phys. Rev. Lett. **114**, 017001 (2015).

[175] L. Zhao, A. Liang, D. Yuan, Y. Hu, D. Liu, J. Huang, S. He, B. Shen, Y. Xu, X. Liu, L. Yu, G. Liu, H. Zhou, Y. Huang, X. Dong, F. Zhou, K. Liu, Z. Lu, Z. Zhao, C. Chen, Z. Xu, and X. J. Zhou, "Common electronic origin of superconductivity in (Li,Fe)OHFeSe bulk superconductor and single-layer $FeSe/SrTiO_3$ films," Nat. Commun. **7**, 10608 (2016).

[176] D. Wang, L. Kong, P. Fan, H. Chen, S. Zhu, W. Liu, L. Cao, Y. Sun, S. Du, J. Schneeloch, R. Zhong, G. Gu, L. Fu, H. Ding, and H.-J. Gao, "Evidence for Majorana bound states in an iron-based superconductor," Science **362**, 333–335 (2018).

[177] Q. Liu, C. Chen, T. Zhang, R. Peng, Y.-J. Yan, C.-H.-P. Wen, X. Lou, Y.-L. Huang, J.-P. Tian, X.-L. Dong, G.-W. Wang, W.-C. Bao, Q.-H. Wang, Z.-P.

Yin, Z.-X. Zhao, and D.-L. Feng, "Robust and Clean Majorana Zero Mode in the Vortex Core of High-Temperature Superconductor $(\mathrm{Li}_{0.84}\mathrm{Fe}_{0.16})\mathrm{OHFeSe}$," Phys. Rev. X **8**, 041056 (2018).

[178] Y. Oreg, G. Refael, and F. von Oppen, "Helical Liquids and Majorana Bound States in Quantum Wires," Phys. Rev. Lett. **105**, 177002 (2010).

[179] J. Alicea, Y. Oreg, G. Refael, F. von Oppen, and M. P. A. Fisher, "Non-Abelian statistics and topological quantum information processing in 1D wire networks," Nat. Phys. **7**, 412–417 (2011).

[180] G. E. Volovik, "Fermion zero modes on vortices in chiral superconductors," JETP Lett. **70**, 609–614 (1999).

[181] M. Cheng, K. Sun, V. Galitski, and S. Das Sarma, "Stable topological superconductivity in a family of two-dimensional fermion models," Phys. Rev. B **81**, 024504 (2010).

[182] Y. E. Kraus, A. Auerbach, H. A. Fertig, and S. H. Simon, "Majorana fermions of a two-dimensional p_x+ip_y superconductor," Phys. Rev. B **79**, 134515 (2009).

[183] T. Mizushima and K. Machida, "Vortex structures and zero-energy states in the BCS-to-BEC evolution of p-wave resonant Fermi gases," Phys. Rev. A **81**, 053605 (2010).

[184] G. Möller, N. R. Cooper, and V. Gurarie, "Structure and consequences of vortex-core states in p-wave superfluids," Phys. Rev. B **83**, 014513 (2011).

[185] M. T. Tuominen, J. M. Hergenrother, T. S. Tighe, and M. Tinkham, "Experimental evidence for parity-based 2e periodicity in a superconducting single-electron tunneling transistor," Phys. Rev. Lett. **69**, 1997–2000 (1992).

[186] B. Jankó, A. Smith, and V. Ambegaokar, "BCS superconductivity with fixed number parity," Phys. Rev. B **50**, 1152–1161 (1994).

[187] K. T. Law and P. A. Lee, "Robustness of Majorana fermion induced fractional Josephson effect in multichannel superconducting wires," Phys. Rev. B **84**, 081304(R) (2011).

[188] A. R. Akhmerov, "Topological quantum computation away from the ground state using Majorana fermions," Phys. Rev. B **82**, 020509(R) (2010).

[189] E. W. J. Straver, J. E. Hoffman, O. M. Auslaender, D. Rugar, and K. A. Moler, "Controlled manipulation of individual vortices in a superconductor," Appl. Phys. Lett. **93**, 172514 (2008).

[190] G. Ménard, A. Mesaros, C. Brun, F. Debontridder, D. Roditchev, P. Simon, and T. Cren, "Isolated pairs of Majorana zero modes in a disordered superconducting lead monolayer," Nat. Commun. **10**, 2587 (2019).

[191] M. Chen, X. Chen, H. Yang, Z. Du, X. Zhu, E. Wang, , and H.-H. Wen, "Discrete energy levels of Caroli-de Gennes-Matricon states in quantum limit in $FeTe_{0.55}Se_{0.45}$," Nat. Commun. **9**, 970 (2018).

[192] M. Cheng, R. M. Lutchyn, V. Galitski, and S. Das Sarma, "Splitting of Majorana-Fermion Modes due to Intervortex Tunneling in a $p_x + ip_y$ Superconductor," Phys. Rev. Lett. **103**, 107001 (2009).

[193] S. Bravyi and A. Kitaev, "Universal quantum computation with ideal Clifford gates and noisy ancillas," Phys. Rev. A **71**, 022316 (2005).

[194] B. H. November, J. D. Sau, J. R. Williams, and J. E. Hoffman, "Scheme for Majorana Manipulation Using Magnetic Force Microscopy ," arXiv:1905.09792 [cond-mat.supr-con] (2019).

[195] A. Kremen, S. Wissberg, N. Haham, E. Persky, Y. Frenkel, and B. Kalisky, "Mechanical Control of Individual Superconducting Vortices," Nano. Lett. **16**, 1626–1630 (2016).

[196] L. Embon, Y. Anahory, A. Suhov, D. Halbertal, J. Cuppens, A. Yakovenko, A. Uri, Y. Myasoedov, M. L. Rappaport, M. E. Huber, A. Gurevich, and E. Zeldov, "Probing dynamics and pinning of single vortices in superconductors at nanometer scales," Sci. Rep. **5**, 7598 (2015).

[197] I. S. Veshchunov, W. Magrini, S. V. Mironov, A. G. Godin, J.-B. Trebbia, A. I. Buzdin, P. Tamarat, and B. Lounis, "Optical manipulation of single flux quanta," Nat. Commun. **7**, 12801 (2016).

[198] X. H. Niu, R. Peng, H. C. Xu, Y. J. Yan, J. Jiang, D. F. Xu, T. L. Yu, Q. Song, Z. C. Huang, Y. X. Wang, B. P. Xie, X. F. Lu, N. Z. Wang, X. H. Chen, Z. Sun, and D. L. Feng, "Surface electronic structure and isotropic superconducting gap in $(Li_{0.8}Fe_{0.2})OHFeSe$," Phys. Rev. B **92**, 060504(R) (2015).

[199] Z. Wang, P. Zhang, G. Xu, L. K. Zeng, H. Miao, X. Xu, T. Qian, H. Weng, P. Richard, A. V. Fedorov, H. Ding, X. Dai, and Z. Fang, "Topological nature of the $FeSe_{0.5}Te_{0.5}$ superconductor," Phys. Rev. B **92**, 115119 (2015).

[200] D. Rainis and D. Loss, "Majorana qubit decoherence by quasiparticle poisoning," Phys. Rev. B **85**, 174533 (2012).

[201] J. M. Martinis, M. Ansmann, and J. Aumentado, "Energy Decay in Superconducting Josephson-Junction Qubits from Nonequilibrium Quasiparticle Excitations," Phys. Rev. Lett. **103**, 097002 (2009).

[202] A. Bespalov, M. Houzet, J. S. Meyer, and Y. V. Nazarov, "Theoretical Model to Explain Excess of Quasiparticles in Superconductors," Phys. Rev. Lett. **117**, 117002 (2016).

[203] A. R. Akhmerov, J. Nilsson, and C. W. J. Beenakker, "Electrically Detected Interferometry of Majorana Fermions in a Topological Insulator," Phys. Rev. Lett. **102**, 216404 (2009).

[204] L. Fu and C. L. Kane, "Probing Neutral Majorana Fermion Edge Modes with Charge Transport," Phys. Rev. Lett. **102**, 216403 (2009).

[205] B. Lian, X.-Q. Sun, A. Vaezi, X.-L. Qi, and S.-C. Zhang, "Topological quantum computation based on chiral Majorana fermions," PNAS **115**, 10938–10942 (2018).

[206] C. W. J. Beenakker, P. Baireuther, Y. Herasymenko, I. Adagideli, L. Wang, and A. R. Akhmerov, "Deterministic Creation and Braiding of Chiral Edge Vortices," Phys. Rev. Lett. **122**, 146803 (2019).

[207] H. Beidenkopf, P. Roushan, J. Seo, L. Gorman, I. Drozdov, Y. S. Hor, R. J. Cava, and A. Yazdani, "Spatial fluctuations of helical Dirac fermions on the surface of topological insulators," Nat. Phys. **7**, 939–943 (2011).

[208] H. S. Røising, "Topological Superconductivity and Majorana Fermions," (2016), DUO Research Archive.

[209] B. Rosenstein, I. Shapiro, and B. Y. Shapiro, "Majorana states in a p-wave superconducting ring," EPL **102**, 57002 (2013).